2020

Understanding Droplet Mobility and Penetration in Nonwovens via Numerical Simulation and Complementary Experiment

Mohammad Jamali 1991

Understanding Droplet Mobility and Penetration in Nonwovens via Numerical Simulation and Complementary Experiment

A dissertation submitted in partial fulfillment of the requirements for the degree of Doctor of Philosophy at Virginia Commonwealth University

By

Mohammad Jamali

M.Sc. Mechanical Engineering, Iran University of Science and Technology, Tehran, Iran, 2015

Director: Hooman V. Tafreshi

Professor, Department of Mechanical and Nuclear Engineering

Virginia Commonwealth University

Richmond, Virginia

July, 2020

Dedication

I would like to dedicate this work to my family, especially to my parents. I could not have come this far without their unconditional support.

Acknowledgment

I wish to express my sincere thanks to Prof. Hooman V. Tafreshi, my advisor, for his continuous support, valuable guidance and encouragement throughout the course of my research. I would not have been able to finish this work without his support and unfailing faith in me.

I would like to extend my feeling of gratitude to the other members of my Ph.D. committee, Prof. Gary C. Tepper, Prof. Jayasimha Atulasimha, Prof. Chris Lemmon and Prof. Umit Ozgur for their insightful questions, valuable suggestions and comments which have helped strengthen my work.

I am thankful to my friends and my labmates for making my life in VCU and Richmond memorable. I would like to express my gratitude to my family for their endless support.

I would also like to thank the Nonwovens Institute at NC State University and VCU School of Engineering for financial support.

Table of Contents

List of Figures

Abstract

Understanding Droplet Mobility and Penetration in Nonwovens via Numerical Simulation and Complementary Experiment

By Mohammad Jamali, Ph.D.

A dissertation submitted in partial fulfillment of the requirements for the degree of Doctor of Philosophy at Virginia Commonwealth University.

Virginia Commonwealth University, 2020

Director: Hooman V. Tafreshi

Professor, Department of Mechanical and Nuclear Engineering

Water droplet mobility on a hydrophobic surface cannot be guaranteed even when the droplet exhibits a high contact angle with the surface. Droplet mobility is defined as the required force to move a droplet on the surface. In fact, droplet mobility on a surface, especially a fibrous surface, has remained an unsolved empirical problem. As the earth gravity may not be strong enough to initiate water droplet mobility or penetration into some hydrophobic fibrous coatings (electrospun polystyrene), a novel test method was designed. In the experiment, an aqueous ferrofluid droplets rather than water are used so that the body force on the droplets could be enhanced using a magnet, and droplet detachment or penetration could be induced. Our combined experimental-computational revealed the role of microstructure on droplet mobility and penetration into a fibrous coating. It was found that a coating made of aligned fibers could have a droplet mobility less than a random coating. A fiber level force calculation showed that fibers in the middle of the surface

do not play a significant role in keeping the droplet on the surface (negligible relative contribution in resisting droplet detachment). Using the balance of forces acting on the detaching or penetrating droplet, novel easy-to-use expressions are developed to estimate droplet detachment (or penetration) force from (or into) a fibrous surface. This circumvents the need for running CPU-intensive simulations for each and every droplet–coating combinations of interest, and provides a means for designing nonwoven materials with low droplet mobility, e.g., self-cleaning fabrics. In addition, a new technique to study a nonmagnetic droplet (e.g., water) adhesion on hydrophobic surfaces is developed. The nonmagnetic droplet is partially cloaked with a high-surface tension oil-based ferrofluid and a permanent magnet is used to detach the resulting droplet (i.e. compound droplet). At the end, an insightful analysis into the complex nature of this multiphase problem is also provided, and thereby a general-purpose plot that extends the application of our work to other oil–water–solid combinations is presented.

Chapter 1. Introduction

1.1 Background Information

Self-cleaning is a desirable property that allows a surface to remain clean for a longer period of time, and it is often brought about by water (or oil) repellency. Both the self-cleaning and water/oil repellency owe their effectiveness to droplet mobility on the surface (droplet ability to move on the surface). Over the past decade, there has been tremendous progress in creating water repellent (superhydrophobic) or oil repellent (superoleophobic) surfaces. In fact, the technology has advanced to a point where almost any surface can now be made hydrophobic (or even superhydrophobic) by simply applying a commercially-available spray-on coating or by many other ways. However, despite the advances in the chemistry of water-repellent surface/coatings, droplet mobility on a rough surface (e.g., a nonwoven) is neither understood nor formulated. In other words, while one can easily produce a nonwoven material that exhibits high water contact angles (through surface treatment or the choice of polymer), droplet mobility on such a nonwoven may be quite bad (see Figure 1.1) [1]. While hydrophobic nonwovens are more likely to repel water than their hydrophilic counterparts, the extent of this effect has not yet been quantified. No relationship has yet been established between the contact angle of a water (or oil) droplet on a nonwoven surface and the mobility of the same droplet on that surface. For instance, it is quite possible that a droplet forming a contact angle of 100 deg. with a particular nonwoven rolls off the surface a lot faster than the same droplet does on another nonwoven with which it forms a contact angle of 140 deg. Similarly, the penetration of a water droplet into a hydrophobic nonwoven (or an oil droplet into an oleophobic nonwoven) is not understood well. For instance, a water droplet may initially bead up on the surface of a hydrophobic nonwoven, but the very same droplet may penetrate into the structure over time (due to evaporation, as evaporation increases the pressure

inside a droplet) or upon impact with the surface. The question to answer here is how a surface can be designed to repel water (or oil) to remain clean not just initially but over time.

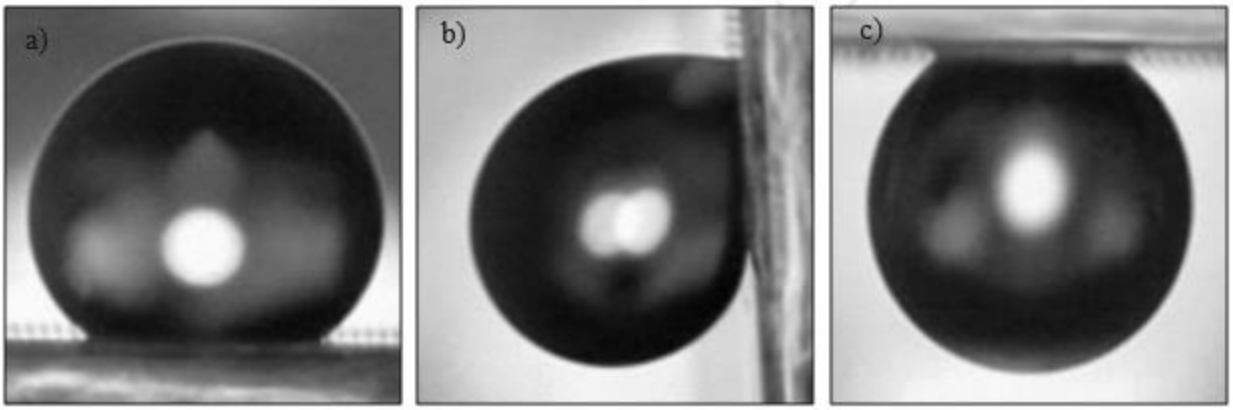

Figure 1.1: Droplet with high apparent contact angle when the surface is tilted a) zero-degree b) 90 degrees c) 180 degrees [1]

1.2. Droplet Mobility

Mobility of a droplet on a nonwoven surface depends on the local wetting state of the surface underneath the droplet. These wetting states include the Cassie state, the Wenzel, the Rose Petal state, and the Gecko state. Briefly speaking, it is the droplet area of contact with the solid surface and the nature of the contact that determines the mobility of a droplet on a nonwoven fabric; the droplet contact angle is not the independent variable in this problem.

This project can be of great interest to industry as it develops a series of experimental and computational tools that can be used for characterizing the behavior of a nonwoven interacting with a fluid. Industries that directly benefit from this research include, but are not limited to, protective clothing (“phobic” nonwovens resisting fluid penetration), absorbent media such as diapers (“philic” nonwovens promoting fluid absorption), fluid–fluid and fluid–air separation media (“philic” to one phase, “phobic” to the other), fuel cells (gas diffusion layer), and fluid coating processes (e.g., kiss-roll coating).

Understanding the interactions between a droplet and a fiber has been of great interest for many years. Droplet–fiber interactions have been studied in many pioneering studies, and it has been shown that the apparent contact angle of a droplet with a fiber can be quite different from the Young–Laplace Contact Angle (YLCA) obtained for a small droplet of the same liquid deposited on a flat surface made from the same material [2–10]. Roughness has been shown to affect the wettability of a surface. Wenzel proposed a relationship between YLCA and a droplet's apparent contact angle on a rough flat surface in terms of the ratio of the actual to the projected area of the rough surface [11]. However, due to a variety of factors, the measured contact angles can be significantly different from the predictions of Wenzel simple relationship [12]. In fact, predicting a droplet apparent contact angle on a rough surface has remained an active area of research for the past decades (see e.g., [13]). Past research has shown that multiple states can be observed for a liquid droplet deposited on a rough surface (e.g., an electrospun Polystyrene nonwoven). These states include the Wenzel (wetted) state, the Cassie (dry) state, and a series of transition states between these extreme states [14–17]. The Wenzel state corresponds to the state where the liquid droplet fills the asperities of a rough surface. The Cassie state, on the other hand, refers to the state where the air bubbles are entrapped in the asperities of the surface under the droplet as the droplet resides only on the peaks of the protrusions. When a droplet transitions from the Cassie state to the Wenzel state, it tends to become "sticky", and the surface loses its water repellent or self-cleaning properties. High apparent contact angles and low contact angle hysteresis are often observed for a droplet at the Cassie state [17]. The volume of a droplet and how it is formed on the surface (or came into contact with the surface) generally dictates the wetting state of the droplet. High apparent contact angles combined with high stickiness was also observed with surfaces having hierarchical roughness. The two main examples of non-wetting but sticky surfaces

are those exhibiting the so-called Rose Petal and Gecko states [1,17]. The Rose Petal state is referred to the case of a non-wetting droplet that penetrates through the micro-scale asperities of the surface but cannot wet the nano-scale asperities [1,17]. The Gecko state is the case where sealed pockets of trapped air cause negative pressure (suction) against droplet movement of the surface.

The angle between the tangent to the liquid-gas interface and the apparent solid surface is different from Young Laplace contact angle (YLCA) and it is known as the apparent contact angle. The shape of a droplet is almost spherical if the surface roughness is isotropic (the apparent contact angle formed by the droplet with the surface is uniform). When the surface roughness is anisotropic (e.g., nonwovens with high machine directionality), the droplet deviates from the spherical shape and the contact angles observed from the machine and cross directions should be different (see Figure 1.2).

The Cassie–Baxter (CB) equation can be used for a rough surface in a heterogeneous wetting regime in order to predict apparent contact angle [18-20]. The CB apparent contact angle θ_{App} is given by

$$cos\theta_{App} = \frac{\alpha d}{s} cos\theta^{YL} + \frac{d\,sin\,\alpha}{s} - 1 \tag{1.1}$$

where α, d, s and θ^{YL} are the immersion angle, fiber diameter, fiber spacing, and YLCA, respectively. The immersion angle is dependent on the pressure drop p and can be calculated using the following equation.

$$p = -\frac{2\sigma\, sin(\theta^{YL}+\alpha)}{(s-d\,sin\,\alpha)} \tag{1.2}$$

Here σ is the surface tension of fluid. Chhatre et al. [21] simplified the CB equation for cylindrically textured surfaces and used a dimensionless spacing ratio in order to consider the

effects of both diameter and spacing between cylinders (see [22–24] for more information about CB equation and its validity).

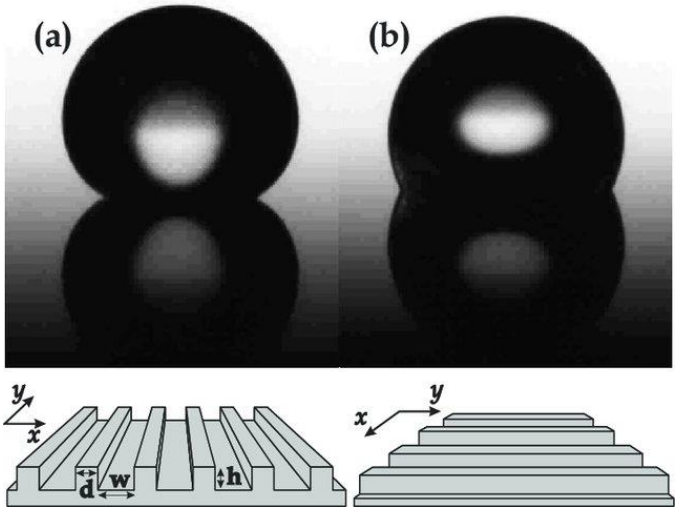

Figure 1.2: A droplet on a striped SH surface: a) transverse side view; b) longitudinal side view [9]

Predicting droplet mobility on a rough surface, i.e., the tendency of the droplet to move on the surface in response to an external force, is a challenge. This is because droplet mobility on a surface depends on many factors including, but not limited to, 1) area of contact between the droplet and the solid surface (wetted area, WA), 2) length of the three-phase air–water–solid contact line (CL), 3) 3-D shape and orientation of WA and CL with respect to droplet's direction of motion, and 4) slope of the air–water interface (AWI) along the CL. In addition, droplet pinning to surface non-homogeneities is another unresolved issue that further complicates this problem [25–27]. For these reasons, it is almost impossible to accurately predict the force required to move a droplet on a surface via a first-principle theoretical approach. For the lack of a better option, designing a self-cleaning surface has remained an empirical problem, often approached via try-and-error and characterized in terms of the intellectually-insignificant but easy-to-image largest and smallest ACAs along the perimeter of a droplet (loosely referred to as the advancing and receding ACAs,

respectively) [28–32]. Because of these limitations, the force required to detach a droplet from a surface is often presented in terms of the difference between the advancing and receding CAs (i.e., CA hysteresis) but scaled by yet another empirical factor $1 < k < 3.14$ that is there to compensate for all what is not known about the actual forces acting on the droplet [33–40], i.e.,

$$F = kw\sigma(cos\theta_{max} - cos\theta_{min}) \tag{1.3}$$

In this equation, w is an arbitrary "width" perpendicular to the direction of the motion assigned to the droplet. Being so empirical in nature, this equation can only be used when one takes the effort to experimentally measure the advancing and receding CAs for the desired droplet–surface system at hand (where one may rather measure the force directly!). Fortunately, however, a theoretical approach can still be devised to predict the force needed to move a droplet on a rough hydrophobic surface, but only if droplet pinning is not an issue (e.g., when the surface asperities are not sharp) [41–45].

1.3. Droplet Penetration

Droplet penetration into the pores of a porous surface may take place spontaneously or in response to an external force, depending on the geometrical and wetting properties of the surface–droplet system [46, 47]. Understanding the interactions between a droplet and a fibrous material is of great significance to water-resistant membranes and barriers [48-52], wound dressing and functional textiles [53-56], self-cleaning coatings and surfaces [17, 57, 58], fuel cells [16, 19, 59], and fog harvesting [60-62] among many others. Another example of an industrially-important problem involving droplet–fiber interactions is the removal of dispersed droplets from a gas (e.g., engine exhaust) or a liquid (e.g., diesel fuel) stream, often referred to as coalescence filtration, which has remained an empirical problem since its infancy. Examples of such studies are the experiments

reported in [22, 63-67] where droplet penetration through a coalescing filter (averaged over the entire exposed surface of the filter) were measured at different air flowrates or for filters made of different polymers. Understanding and formulating droplet–fiber(s) interactions allows one to quantify the tendency of a fibrous media to reject or absorb an incoming liquid droplet, and can be used to custom-design the media for their intended specific applications. For instance, in a study on droplet impact on electrospun fibrous membranes, it was shown that inertial droplet penetration into a membrane can be categorized into different regimes depending on the interplay between droplet inertia (promoting droplet penetration) and capillary forces (resisting penetration in the case of hydrophobic membranes, but helping in the case of hydrophilic membranes) [68-71]. Such an enabling knowledge can also be used in designing water-repelling membranes for desalination or a variety of other applications as mentioned earlier [48-62].

1.4. Compound Droplet

To characterize the degree of hydrophobicity of a surface, one needs to measure the force needed to detach (or move) a droplet from (or on) the surface (i.e. normal and lateral adhesions). The traditional approach to measure the force of lateral adhesion between a water droplet and a surface has been to measure the role-off angle (the inclination angle at which the droplet rolls off the surface). Obviously, this method becomes inefficient if the force needed to move the droplet is greater than the weight of the droplet. Alternative methods therefore, have been proposed over the years to overcome this problem. These methods include, but are not limited to, centrifugal force (e.g., [28, 72] for lateral adhesion and [73, 74] for normal adhesion), the use of an external device like the tip of an atomic force microscope [75–77], or an air flow (e.g., [78–80]) for both lateral and normal adhesions. The first study to report measuring droplet detachment force using a magnet

was the work Amrei et al. [81], who studied normal adhesion force between a hydrophilic fishing line and a water-based ferrofluid droplet in 2016 (see also the work of Timonen et al. [82] for the use of magnetic field in studying droplet lateral adhesion). While the method of [81] was easy to implement and accurate for its simplicity, it could only be used for detaching ferrofluid droplets. To expand the application of this method to the case of non-magnetic fluids (e.g., water), Farhan and Tafreshi [83] recently developed a new droplet detachment approach in which the non-magnetic droplet was cloaked with an immiscible ferrofluid (in the form of a compound droplet) to allow the use of a magnetic force for droplet vertical detachment (see also [84] for transport a sessile water droplet floating over spikes of an oil-based ferrofluid on a ferrofluid layer). The water droplet detachment via producing a compound droplet is a novel method.

1.5. Overall Objectives of This Thesis

Droplet mobility on a nonwoven surface is neither well-understood nor formulated. No relationship has yet been established for the mobility of a droplet on a nonwoven surface in terms of nonwovens' microstructural parameters. The goal of this project is to fill the above knowledge gap, and to also provide a means for designing nonwoven materials allowing good mobility for water/oil droplets (e.g., self-cleaning fabrics). We consider a combination of numerical simulations and experiments to better our understating of the physics of droplet motion on a nonwoven surface. For the case of droplet mobility, we start the project by considering the simplest nonwoven microstructures, unidirectional and orthogonal nonwoven structures. The droplet detachment from these nonwoven structures in the vertical and horizontal directions is studied both computationally and experimentally. More specifically, we study the effects of Young-Laplace contact angle (YLCA) and fiber spacing on droplet detachment force (the force required to detach the droplet).

For the experimental component of this research, we design and build a test setup to measure droplet detachment forces in the vertical and horizontal directions. The experiments are imaged using a high-speed video camera, and the images are used to analyze the shape (contact line and contact angle) of the droplet during detachment or penetration. Easy-to-use expressions are developed to estimate droplet detachment force from a fibrous surface in the vertical and horizontal directions. In addition, a compound droplet made of two immiscible droplets has been studied and formulated. More specifically, a water droplet is partially cloaked with a high surface tension ferrofluid and a permanent magnet is used to detach the water droplet. Numerical simulations have provided an insight to a complex four phase compound droplet detachment.

Droplet penetration into the pores of a porous surface may take place spontaneously or in response to an external force, depending on the geometrical and wetting properties of the surface–droplet system. Droplet penetration into a nonwoven surface is neither well-understood nor formulated similar to droplet mobility. For the case of droplet penetration, the same experimental setup as droplet mobility is also used to measure droplet's penetration force. Effects of these parameters on the force needed to pull a droplet into a hydrophobic nonwoven are investigated as well. Easy-to-use expressions are developed to estimate droplet penetration force into a fibrous surface.

This study has three major goals each having a series of objectives. Goal 1 is to discover and formulate the important factors affecting droplet mobility (or droplet stickiness) on a nonwoven fabric (structure–droplet-mobility relationships). Goal 2 is to discover and formulate the important factors affecting droplet penetration into a nonwoven fabric (structure–droplet-penetration relationships). Goal 3 is developing structure–property relationships for droplet mobility and penetration.

Chapter 2. Droplet Adhesion to Hydrophobic Fibrous Surfaces

2.1. Introduction

Previous studies have shown that a droplet deposited on a coating with unidirectional fibers may exhibit different ACAs in different directions [18, 19, 85, 86]. Therefore, one can potentially improve or control the adhesion force between a droplet and a fibrous coating by controlling the orientation of the fibers. The easiest way to produce a fibrous mat with directional fibers is to deposit parallel fibers in orthogonal layers. As will be seen later, the strength of droplet adhesion to such a surface depends strongly on the extent of interactions between the orthogonal fibers and the droplet. In this work, we characterize these interactions both computationally, via finite element simulations, and experimentally, using coatings comprised of orthogonal electrospun Polystyrene fibers. We obtain the force needed to detach a droplet from such orthogonal fibrous coatings in a direction normal to the surface (referred to here as droplet detachment force).

2.2. Methods: Droplet Detachment Experiment and Simulation

In this section, we first discuss the steps considered in producing electrospun Polystyrene (PS) coatings, and then present our method of measuring the force of adhesion between droplets of different volumes and these orthogonal fibrous structures.

Electrospinning is a means of producing nanofibers from a solution driven by a strong electrostatic field. To produce electrospun PS mats, we dissolved PS pellets in a 70–30 wt% Toluene–Tetrahydrofuran (THF) mixture to obtain a solution with 25 wt% PS concentration (a PS concentration of 25% was chosen based on previous experience with electrospinning PS with the same setup [87, 88]). The solution was allowed to rest for a day to ensure homogeneity. A positive voltage of 5.5 kV with respect to a grounded target was applied to a hypodermic syringe tip

mounted on a syringe pump with an infusion rate of 2.5 μL/min. The distance between the syringe tip and the target was set to 85 mm. The substrate was a microscope cover glass from McMaster Carr. To produce coatings with aligned fibers the substrate was placed on an axially moving rotating drum with rotational and translational speeds of 1200 rpm and 1.5 cm/s, respectively. The orthogonally-layered structures were made by rotating the substrate by a 90-degree angle after depositing each layer (see [87, 88] for more information), and the average fiber-to-fiber spacing was varied by varying the total spinning time for each layer. Figure 2.1a shows a SEM image of such an orthogonally-layered fibrous material. Note that, due to the inherent instability of the electrospinning process, it is not easy to obtain perfect fiber alignment or fiber–fiber spacing, and this obviously contributes to the errors associated with our experimental data, as will be discussed later.

To measure the force required to detach a droplet from a surface, we use ferrofluid droplets in a magnetic field [81]. This method is quite easy to implement, and it is also flexible with regards to changing the direction at which droplet detachment force is measured (see Figure 2.1b). This is in contrast to the more established methods through centrifugal forces [73], an atomic force microscope [75], or air flow [78, 79]. The force of detachment was measured using a sensitive scale (Mettler Toledo XSE105DU with an accuracy of 0.01 mg). The ferrofluid used in the experiment (purchased from EMG508, Ferrotech, USA) was an aqueous suspension of Fe3O4 nanoparticles (contained 1% volumetric) with a mixture density of ρ =1.05 g/cm3 at 25 °C. Note that, the detachment force obtained from our experiments using a ferrofluid droplet can be generalized to droplets of other fluids after scaling with their surface tension ratios. Droplets of various volumes (2–7 μL) where produced using a New Era NE-300 syringe pump, and gently deposited on the electrospun mats. The mats were mounted on a 3-D printed holder and the holder

was placed on the scale. Next, the scale was zeroed and a magnetic force was vertically applied to the droplet by a nickel-plated axially magnetized cylindrical permanent magnet with a diameter of 22 mm and a length of 22 mm (K&J Magnetics).

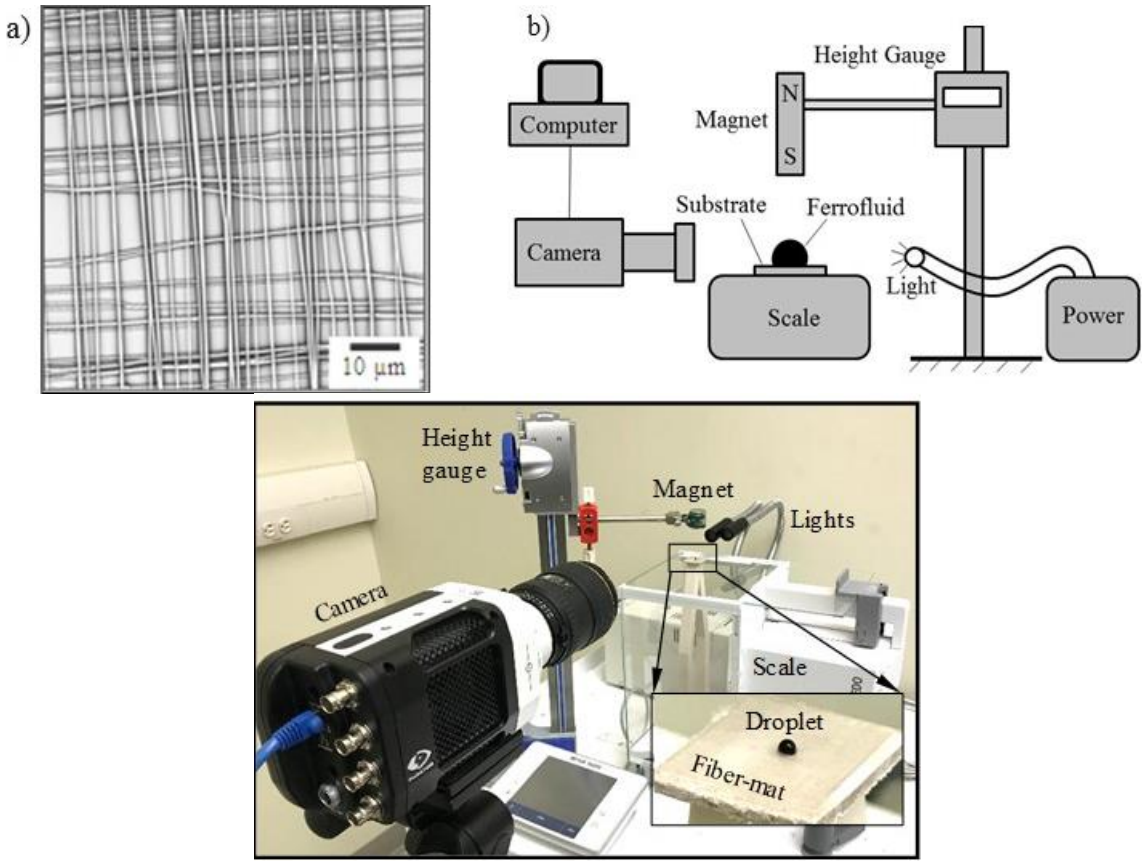

Figure 2.1: An example of our electrospun mats comprised of two orthogonal layers (3 minutes spinning per layer) of aligned PS fibers with a diameter is about 0.5 µm in shown in (a). Schematic and actual image of our experimental setup is given in (b).

The magnetic force was increased incrementally by lowering the magnet (attached to a Mitutoyo electronic height gauge) toward the droplet, and the corresponding readings on the scale digital display was videoed (to ensure that the scale reading at the moment of droplet detachment is recorded). Note that the detachment process consists of a series of quasi-static equilibrium states,

where droplet shape changes in response to the external force, and a fast and spontaneous process, where it actually detaches from the surface. Our detachment force measurements correspond to the final state of droplet equilibrium before the spontaneous detachment process starts (see [81]). The entire droplet detachment experiment was recorded with a digital high-speed camera (Phantom Miro Lab 340 with) with a Tokina 100 mm F 2.8 D lens. An additional camera (Nikon D3100 camera with an AF-S micro Nikkor 105 mm lens) was used to take pictures from the residue left on the mat or from the droplet at an angle perpendicular to the high-speed camera.

We use the Surface Evolver (SE) finite element code in this work for our simulations. SE uses an iterative method to obtain the equilibrium shape of a droplet by minimizing the total energy of the air–water–solid system (Eq. 2.1) [89].

$$E = \sigma A_{aw} - \sigma \cos\theta^{YL} \iint_{A_{sw}} dA + \iiint \rho g z dV_a \tag{2.1}$$

In this equation, A_{aw}, A_{sw} and V_a denote the air–water and solid–water interfacial area, and droplet volume respectively. For our calculations, the solid–water interfacial area A_{sw} and volume of wetted fibers V_s are defined and programed in SE so that the code can correctly calculate the droplet volume V_a in presence of interacting fibers.

$$dA_{sw} = -\frac{xz}{\sqrt{y^2+z^2}}dy + \frac{xy}{\sqrt{y^2+z^2}}dz \tag{2.2}$$

$$dV_s = (-xzdy + xydz)/2 \tag{2.3}$$

Simulations start by placing a droplet with an arbitrary shape on the fibers. SE then continuously evolves the droplet shape to shapes that results in a lower total energy for the total system. In each iteration, the three-phase contact line (CL) moves over the surface, while the AWI maintains a slope corresponding to the YLCA with the solid surface. A constraint is also placed on the solid walls to prevent droplet from penetrating into the fibers (non-physical). After droplet's equilibrium shape and position are obtained, an external force (in the in-plane or out-of-plane directions) is

exerted on the droplet and its magnitude is increased gradually until the droplet is about to move over the surface (in-plane) or detach from the fibers (out-of-plane directions). To ensure that our simulation results are not dependent on the choice of mesh density, the wetted area under a droplet with a volume of 0.5 μL and an YLCA of 85 is calculated for a coating having a fiber diameter of 10 μm, and a spacing of 80 μm. The mesh density was then increased incrementally and its effects on the wetted area as well as droplet's ACA were recorded. It was found that simulations performed with a mesh density of $d/20$ along the CL produce numerical results with less than about 5% mesh dependence (not shown for the sake of brevity). Figure 2.2a is an example of our SE simulations conducted for a droplet with a volume of $0.5\mu L$ deposited under the influence of gravity on two layers of parallel fibers placed orthogonally on top of one another (red on top and green on the bottom). The diameter of the fibers and their center-to-center spacing are 10 μm and 110 μm, respectively. The YLCA of the material of the fibers is assumed to be 85 degrees. Figure 2.2b shows a magnified image of droplet–fiber contact viewed from inside of the droplet. It can be seen that the droplet has come into contact with the bottom layer (green fiber) in addition to the fiber on top (the red fibers), but has not reached the substrate on which the fibers are deposited (see Figure 2.2c and 2.2d).

The computational component of this research is devised to provide insight into the process of droplet detachment from a fibrous coating (e.g., electrospun mats). However, one should note that a series of simplifications has to be considered to make such simulations feasible. This is due mainly to two factors: 1) the inherent imperfection of electrospun mats in terms of fiber spacing, fiber diameter, and fiber alignment, which is hard to duplicate in a model, and 2) the computational challenges involved in modeling interactions between a millimeter-sized droplet and a large number of sub-micron fibers (three orders of magnitude size difference). To validate the accuracy

of our numerical simulations (through a one-on-one quantitative comparison), we produced orthogonal fibers with a diameter of 291 μm and a fiber spacing of 920 μm using a 5th Gen Makerbot Replicator 3-D printer. We spray-coated the printed structures with Ultra-Ever Dry solution from Ultratech Company. Prior to coating the fibers with Ultra-Ever Dry, a layer of adhesive was applied to the fibers and the fibers were left to dry for 30 min. The fibers were left to dry for a day before being used in the experiment. The coating was also applied on a glass slide and an YLCA of about 119 degrees was obtained for the coating with ferrofluid (not shown for brevity). Figures 2.2e–2.2g show a ferrofluid droplet with a volume of 15 μL on the above 3-D-printed structures with orthogonal fibers from top, longitudinal, and transverse views, respectively. Figure 2.2h compares the results of numerical simulation with experiment conducted for the ferrofluid droplet on the same printed mesh but under the influence of a magnetic body force applied in the positive z-direction. In this experiment, the magnetic force was incrementally increased by lowering the magnet stepwise, and the droplet was imaged at each step (only a few steps are shown in Figure 2.2h for the sake of brevity). Good agreement can be seen between simulation results and experiment at each force increment. A final detachment force of 0.2g (i.e., 2.0 N/kg) was obtained from the simulations, which is within 15% margin of error from the detachment force obtained experimentally (averaged over 5 repetitions using different parts of the same coated mesh). The parameters contributing to the mismatch between experimental and numerical results include, but are not limited to, non-uniformity in the coating applied to the fiber surface (possibly causing some variations in the YLCA of the fibers), and imperfection in the geometry of the printed fibers in terms of fiber spacing, fiber cross-sectional shape, and fiber surface roughness (leading to droplet pinning). These factors were obviously not included in the

simulations. More specifically, the fibers are assumed to be perfectly smooth cylinders in the simulations causing no resistance against droplet motion in the direction of the fibers.

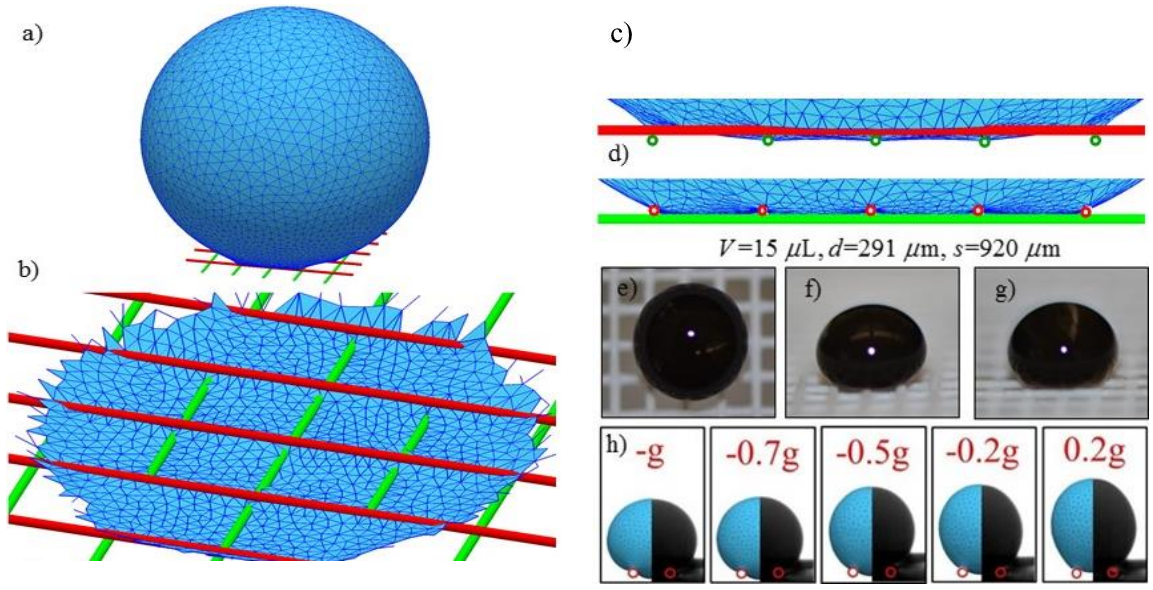

Figure 2.2: An example of droplet shape simulation on two orthogonal layers of aligned fibers is given in (a) for a droplet volume of 0.5µl, a fiber diameter of 10µm, and a fiber-fiber spacing of 110 µm. The air–water interface in contact with the fibers is shown in (b), (c), and (d) as they are viewed from inside, from the transverse direction, and from the longitudinal direction, respectively. Images of a ferrofluid droplet with a volume of 15 µl on a 3-D printed structure are shown in (e), (f), and (g) from top, longitudinal, and transverse views, respectively. Diameter and spacing between the filaments in the printed structure are 291 µm and 920 µm, respectively. Side-by-side simulation–experiment comparison is given in (h) for the shape of the above droplet as it changes in response to a body force increasing from left (downward gravity only) to right (net 0.2 g upward).

2.3. Experimental Results

In this section, we present our experimental detachment force data obtained for PS electrospun mats with orthogonal fibers. Polystyrene mats were produced in the form of 2, 3, or 4 layers of parallel fibers with 3 minutes of spinning time for each layer. Fiber diameter was measured from SEM images, and it was found to be about 0.5 µm on average. Figure 2.3a shows the force required to detach a ferrofluid droplet with volume of $4\mu L$ from these mats. It can be seen that detachment force is about 35 N/kg (3.5 times greater than the gravity) for both the three-layer and four-layer

mats, but it is about 60 N/kg for the two-layer mat (about 70% higher). Examples of droplet residues on the mats after detachment are also added to Figure 2.3a as insets, and it can be seen that the residue left on the two-layer mat is much larger than those left on the three-layer and four-layer mats. To further explain the reason for this behavior, examples of detachment process are shown in Figures 2.3b and 2.3c for two-layer and three-layer coatings, respectively.

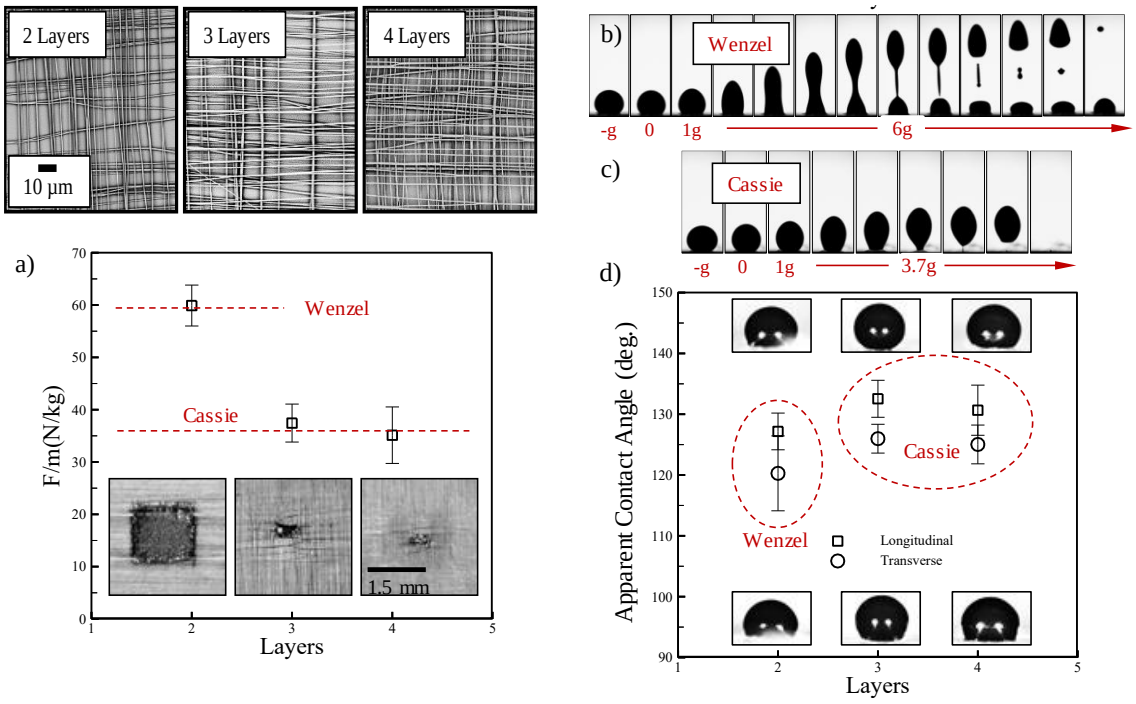

Figure 2.3: Droplet detachment force versus number of layers of fibers is shown in (a). The inset images show droplet residue on the mat for each case (the large residue is from the Wenzel droplet). Examples of high-speed images of droplet detachment are shown in (b) and (c) for Wenzel and Cassie droplets, respectively. Transverse and longitudinal ACAs are given in (d) for ferrofluid droplets with a volume of 4 µl.

In these figures, magnetic force on the droplet is increased from left to right. Once the magnetic force reaches a critical value (referred to here as droplet detachment force), a spontaneous detachment process starts and continues until the droplet breaks up into two volumes (Figure 2.3b) or detaches with no measurable residue on the surface (Figure 2.3c). The reason for this behavior is that the droplet in Figure 2.3b had come into contact with the hydrophilic substrate underneath

the fibers (i.e., Wenzel state) but the one in Figure 2.3c had remained in the Cassie state. Figure 2.3d shows the average ACAs of the droplets on the above mats in longitudinal and transverse directions in the absence of a magnetic force (gravity only). It is interesting to note that droplets' average ACAs on all mats are within about 10% of one another despite their strikingly different detachment behavior. This is because the hydrophobic PS fibers resist against Wenzel droplets spreading over the surface.

Figures 2.4a and 2.4b show detachment force, ACA, and critical ACA (the apparat contact angle of the droplet at its final equilibrium state before spontaneous detachment) for a droplet with a volume of $4\mu L$ on mats comprised of one layer of parallel PS fibers, respectively. The *x*-axis in these figures is fiber deposition time, which is inversely proportional to fiber spacing as can be seen in the SEM images shown in Figure 2.4a. It can be seen that detachment force increases by a factor of about two when deposition time increases from 3 min to 8 min (when the mats become denser), but ACA and critical ACA vary only a few degrees, confirming the fact that contact angle information alone is not enough to quantify the degree of droplet adhesion to a surface. Note that the reported critical ACAs are imaged from the longitudinal direction only as additional synchronized high-speed cameras are needed to capture the critical ACA from more than one view. Also note in Figure 2.4b that critical ACAs are about 20 degree smaller than the ACAs for most cases. Figure 2.4c shows examples of droplet detachment sequences for three different fiber-mats having different fiber spacing (corresponding to 3, 5, and 8 minutes of electrospinning). The ACAs and critical ACAs are marked in these figures with blue and red frames, respectively. Figure 2.4c, also shows examples of droplet residues on the fiber-mats, and it can be seen that the residue is bigger when the fibers are packed more closely (e.g., the case of 8 min spinning time).

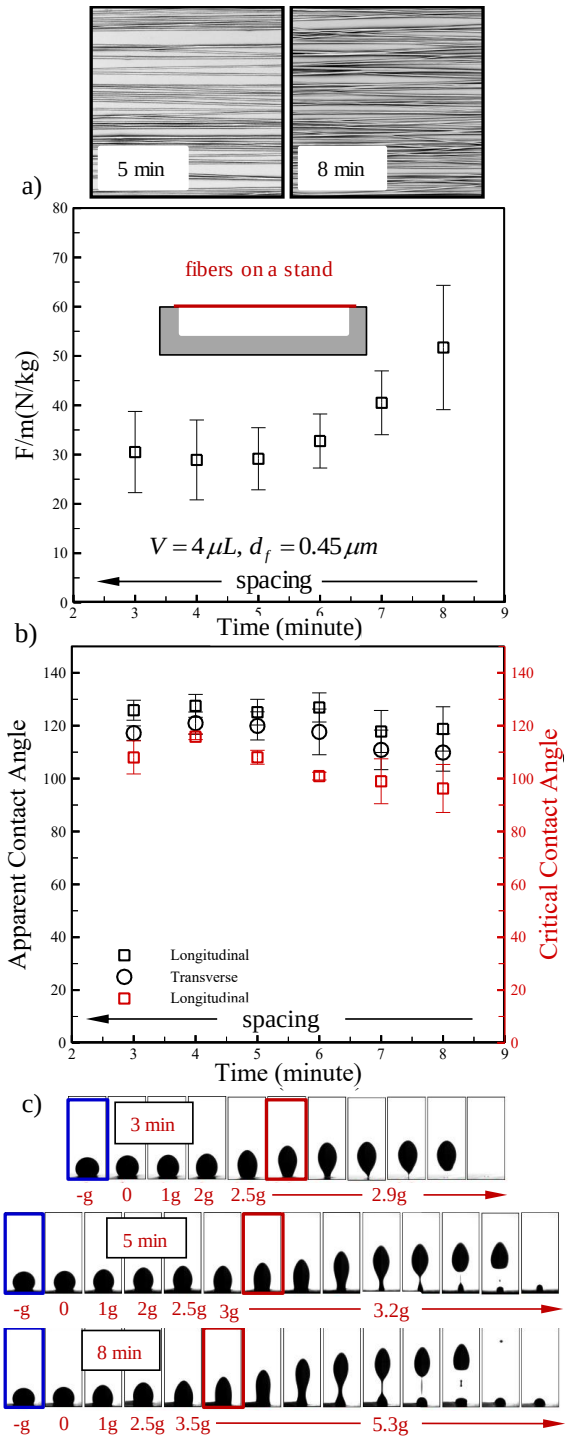

Figure 2.4: Droplet detachment force versus fiber spinning time per layer (inversely proportional to fiber-to-fiber spacing in the layer) is given in (a) for a droplet with a volume of 4 µL. The mats used for the experiments were composed of aligned fibers. Transvers and longitudinal ACAs as well as critical ACAs (final state of equilibrium before detachment) are given in (b). The latter was only imaged from the longitudinal view. Examples of droplet detachment process from these mats are shown in (c) for mats with different fiber-to-fiber spacing (characterized by spinning time). Droplet volume is 4 µL.

Detachment force and ACA results are shown in Figures 2.5a for mats comprised of three layers of orthogonal fibers. It can again be seen that detachment force increases (although not so drastically) when deposition time increases from 3 min to 8 min (when the mats become denser), while ACA vary only negligibly (critical ACAs are not reported for the sake of brevity but a few examples can be seen in Figure 2.5b).

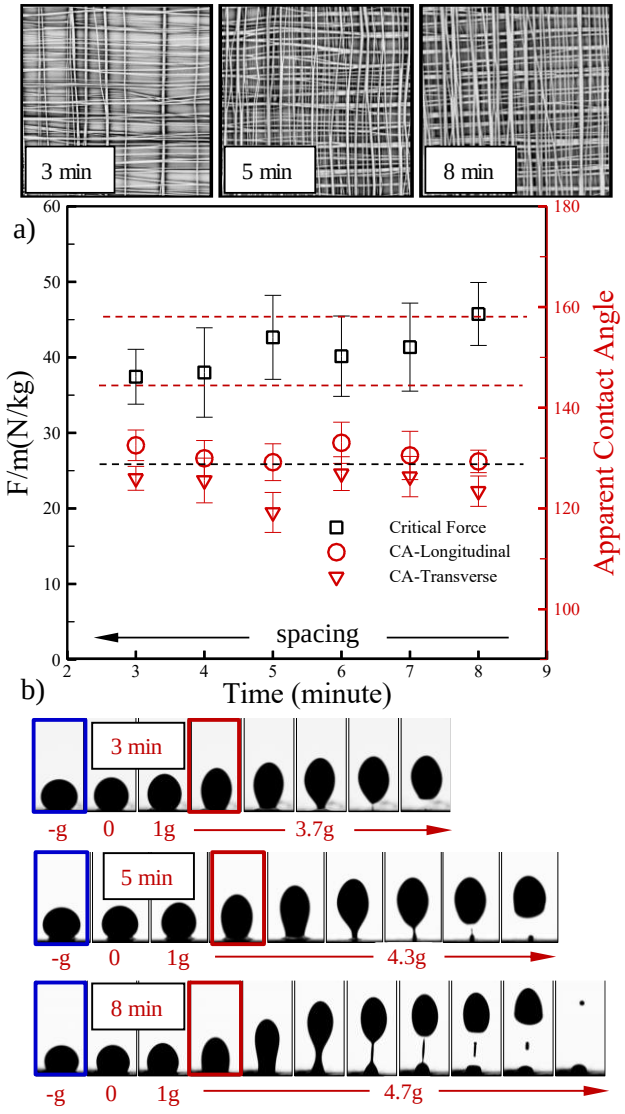

Figure 2.5: Droplet detachment force versus fiber spinning time per layer (inversely proportional to fiber-to-fiber spacing in the layer) is given in (a) for a droplet with a volume of 4 µL. The mats used for the experiments were composed of orthogonally layered aligned fibers. Examples of droplet detachment process from these mats are shown in (b) for mats with different fiber-to-fiber spacing (characterized by spinning time). Droplet volume is 4 µL.

Comparing the results obtained for three-layer mats with those obtained for one-layer mats (Figure 2.4), one can see that ACAs are generally larger (but only about 10%) for the three-layer mats. The detachment forces are also generally higher for the three-layer mats with the exception of the one-layer mats at 8 min deposition. We conjecture that the increase in detachment force and the decrease in ACA with increasing deposition time is due to droplets coming into contact with more fibers. Figure 2.6a shows detachment force and ACA for a range of droplet volumes deposited on three-layer mats with a deposition time of 5 min. It can be seen that ACA decreases only slightly with increasing droplet volume, but the detachment force per unit mass decreases rapidly (as expected). Figure 2.6b shows the sequence of droplet detachment for different droplet volumes.

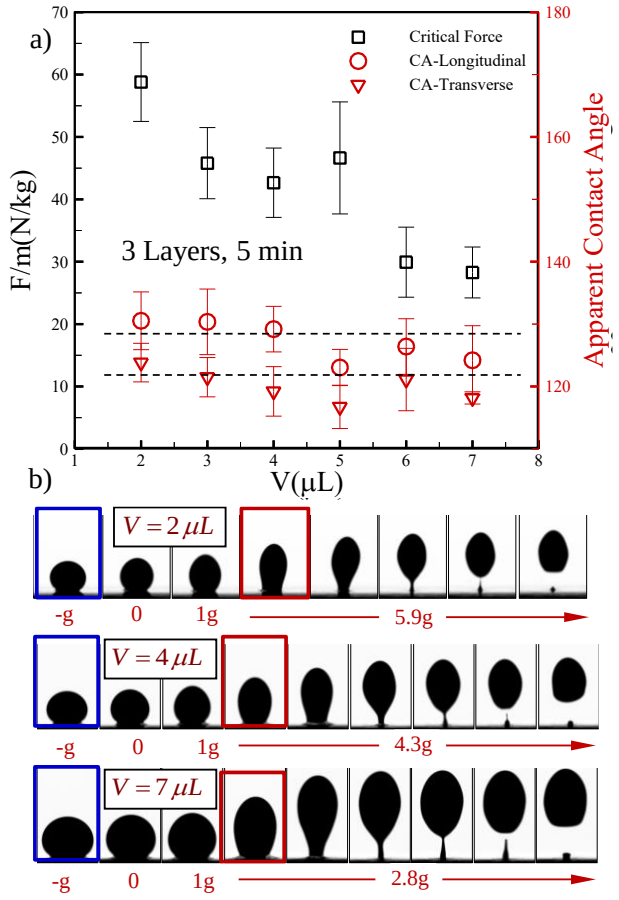

Figure 2.6: Detachment force and ACAs for droplets with different volumes in given in (a). The mats used for the experiments were composed of 3 orthogonal layers with 5 min fiber spinning per layer. Examples of droplet detachment process from these mats are shown in (b) for different droplet volumes.

Overall, one can notice from Figures 2.3–2.6 that the force required to detach a droplet from a fibrous surface is not directly correlated to its ACA on the surface (hence the rose petal effect). We further discuss this in the next section using our simulation results.

2.4. Simulation Results

As mentioned earlier, simulating detachment of a millimeter-sized droplet from a coating comprised of submicron fibers is computationally prohibitive. Therefore, for our simulations in this section, we considered fibers with a fixed diameter of 10 μm (about 10 to 20 times larger than those produced experimentally), and used a droplet volume of 0.5 μL only. We consider water to be the fluid in the simulations. We start by studying the effects of fibers' spacing and YLCA on droplet detachment from coatings with orthogonal fibers. To do so, we first discuss droplet ACAs in the absence of an external body force but then move on to simulate droplet detachment due to a vertical body force.

Figure 2.7a shows the variation of the ACA, defined along the perimeter of the droplet area of contact with the surface. Here, we define local ACA as the angle between a plane tangent to the droplet at a certain distance above the surface of the fibers, and a horizontal plane at that location, i.e.,

$$\theta_{App} = \cos^{-1}(\hat{n}_p.\hat{n}_d) \tag{2.4}$$

where $\hat{n}_p$ and $\hat{n}_d$ are normal vectors to these planes as shown in the inset figure. We obtain an average ACA by integrating the local ACA along the CL, i.e.,

$$\bar{\theta}_{App} = \frac{\int \theta_{App} dl}{\int dl} \tag{2.5}$$

Figure 2.7b shows the effects of fiber spacing and YLCA on average ACA for a droplet on a coating with two layers of orthogonal fibers. It can be seen that ACA generally increase with increasing fiber spacing for small fiber spacing values, but it reaches a plateau (with some fluctuations) with further increase in fiber spacing. In other words, ACA seems to increase with fiber spacing when the droplet is in contact with only the fibers in the first layer (shown in the figure with vertical dotted lines for each YLCA). Note that these computational ACAs cannot directly be compared with the experimental ACAs shown previously in Figures 2.3–2.6 because of the differences between the dimensions of fibers and droplets. More specifically, the droplets used in the experiment (being bigger than those used for the simulations) come into contact with more number of fibers (being smaller than those used in the simulations), and this tends to smooth out some of the ACA fluctuations shown in Figure 2.7b. Predictions of the CB equation are also added to Figure 2.7b for the range of fiber spacing values in which the droplet is in contact with the first layer only (CB cannot be applied to droplets in contact with more than one layer of fibers). Good agreement can be seen between the computational results and the CB equation. Figure 2.7b also shows that ACA is higher for surfaces with higher YLCAs, as expected.

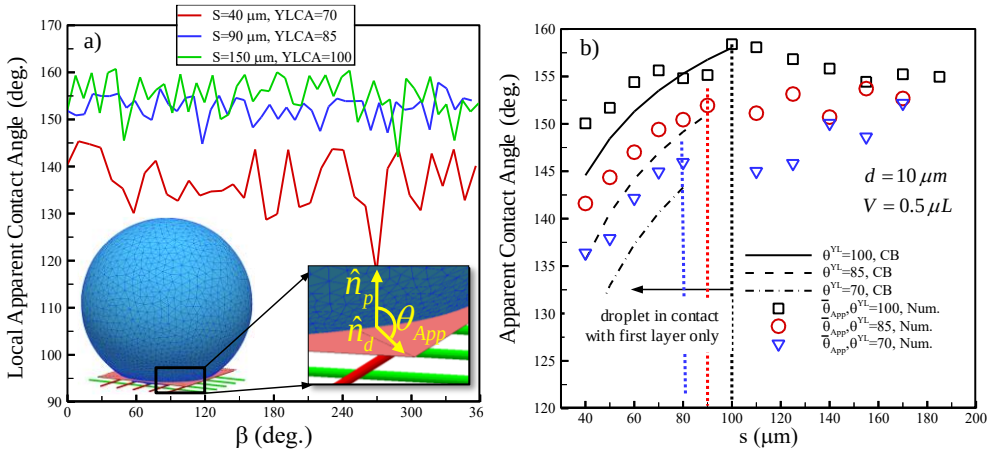

Figure 2.7: Local ACA along the perimeter of droplet contact area with the mats having different YLCAs or fiber spacing is given in (a). Effects of fiber spacing and YLCA on average ACA (averaged along CL) are shown in (b). Predictions of the Cassie–Baxter equation are also added for comparison (applicable only to droplets in contact with the top layer of fibers).

After an equilibrium shape was obtained for a droplet, we applied a small body force to the droplet and increase it with an arbitrary increment of $\Delta g_z = 0.5$ N/kg until no stable shape was obtained for the droplet on the fibers. The largest body force under which a stable droplet shape could be obtained (plus an increment of Δg_z) was then taken as the force required to detach the droplet from the surface. Note that the simulation method considered in this work cannot be used to model the dynamics of droplet detachment from the surface or the volume of the droplet residue after detachment. Figures 2.8a and 2.8b show examples of droplet shape under the influence of a vertical body force from the longitudinal and bottom viewpoints. The droplets shown on top are in contact with only one layer of fibers (s =80 μm), whereas those shown on the bottom are in contact with both layers of fibers (s =140 μm). The average ACAs of these droplets are recorded as a function of the external force and are shown in Figure 2.8c. It can be seen that ACA does not vary much with varying external force, which is somewhat different from what we reported in Figure 2.4 (where the critical ACA for each fiber spacing was about 20 degrees less than the ACA for that spacing). We believe this is due to two main reasons. Firstly, for a droplet as small as 0.5 μL (simulated droplets), the Laplace pressure is too high to allow the droplet shape to deviate from an almost spherical shape before the droplet detaches from the surface. This is not the case for the droplets used in the experiments as they were much bigger. Secondly, the simulated droplets in Figure 2.7 were all in the Cassie state, whereas those in the experiment might have partially (or locally) transitioned to the Wenzel state (and hence the small droplet residues on the surface as shown in Figure 2.4c). Our simulations also show that fibers' wetted area and droplet CL decrease significantly with increasing the external force (Figure 8d), which also support the above argument, i.e., the unpinned CL shrinks in response to increasing the external force allowing the ACA to remain unchanged. While we did not attempt to measure the wetted area or CL

experimentally in all cases, one can observe from droplet snapshots given in Figure 2.3–2.6 that they also decreased with increasing external force.

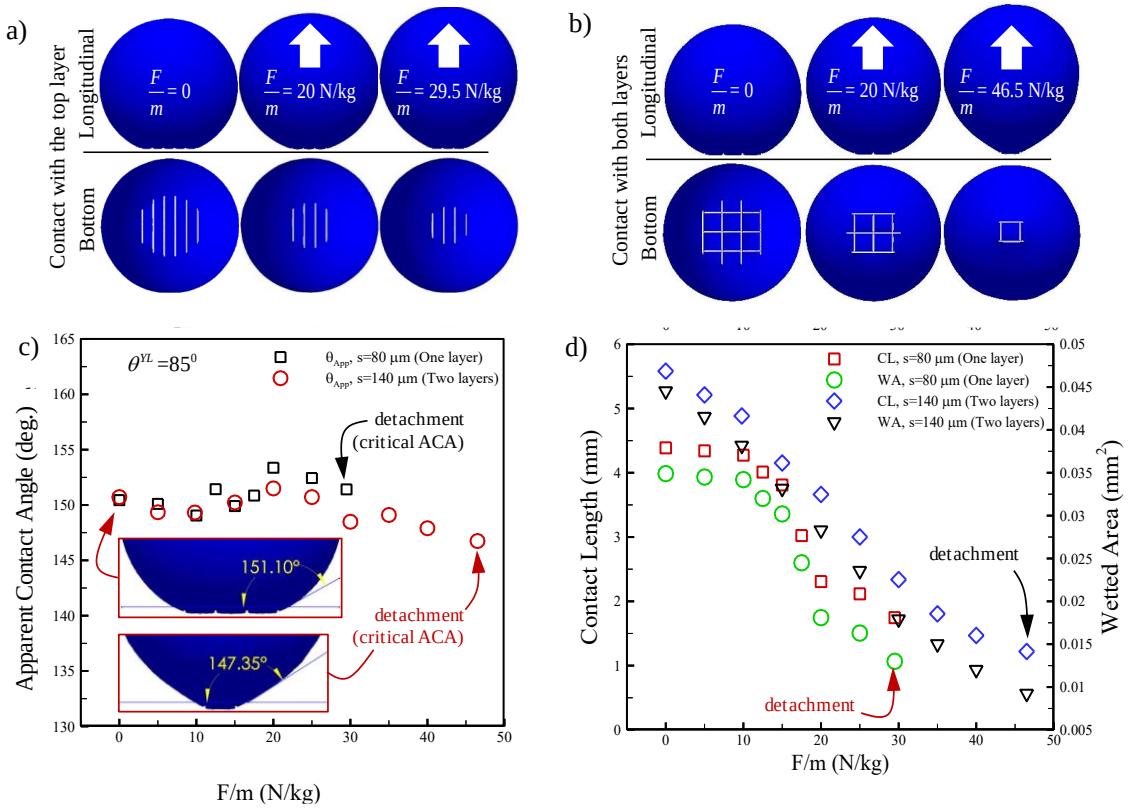

Figure 2.8: Droplet profile as a function of net external force from longitudinal and bottom views are given in (a) for s =80 μm and in (b) for s =140. Effects of increasing vertical body force (leading to droplet detachment) on ACA (c) and on CL and wetted area (d) are shown for mats with two different fiber spacing but an identical YLCA of 85 degree.

Figure 2.9a shows droplet detachment force for coatings with different fiber spacing and YLCAs. Detachment force seems to decrease with increasing fiber spacing when the spacing is relatively small and the droplet is in contact with only the fibers in the first layer which is in agreement with the experimental data in Figure 2.4. However, the detachment force tends to increase with fiber spacing when the droplet is in contact with both layers. This also corresponds to how wetted area and CL vary with spacing (see Figure 2.9b). The results presented in Figure 2.9a suggest that there

exists a fiber spacing for which the vertical detachment force is minimal (i.e., maximum fiber spacing as long as the droplet is in contact with the fibers in the top layer only), which is an important conclusion from a practical point of view. Note that detachment force in all the cases reported in Figure 2.9a is more than 9.8 N/kg, meaning that gravity is not enough to detach the droplet from the surface even when it is turned upside down (sticky superhydrophobic surface).

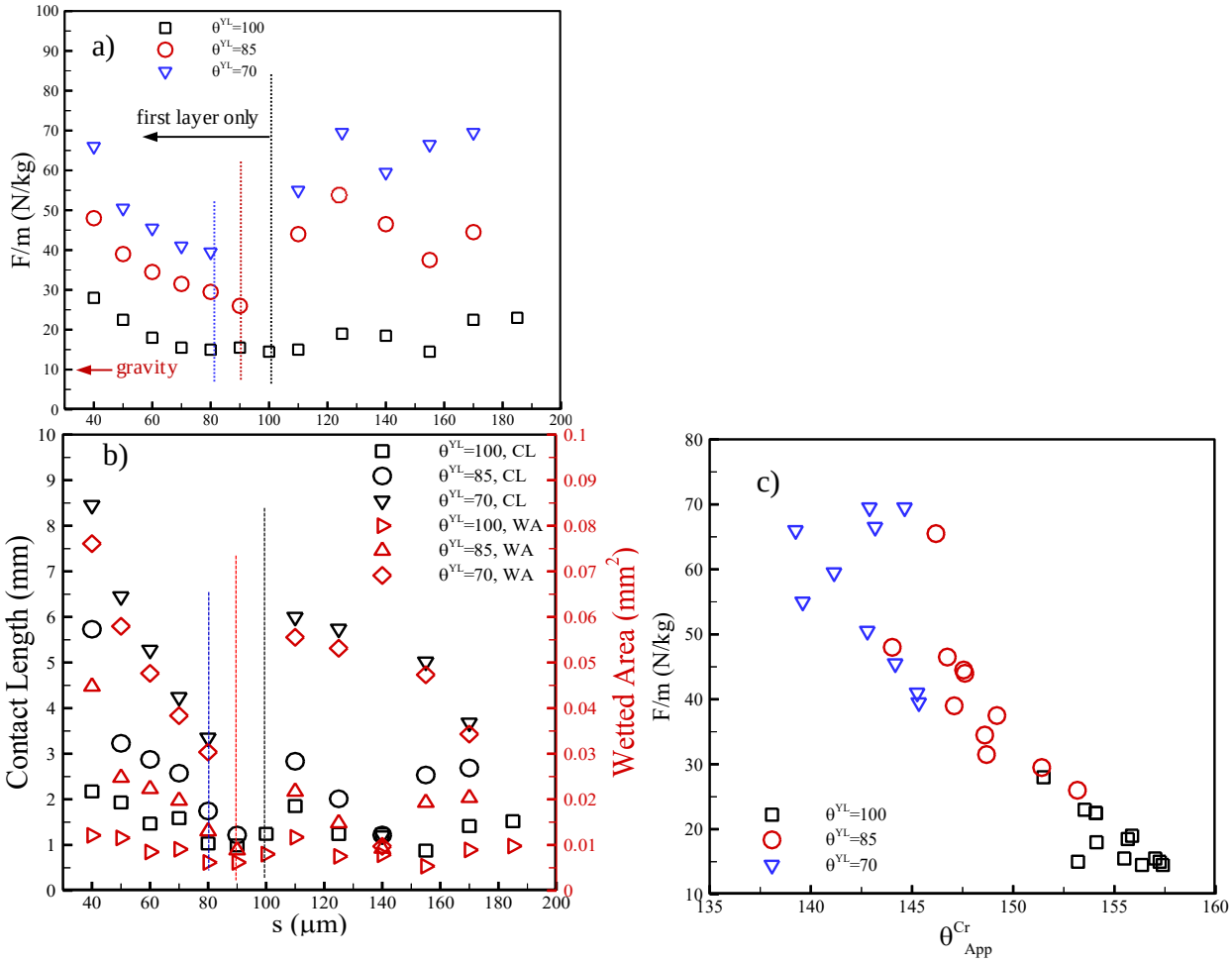

Figure 2.9: Effects of fiber-to-fiber spacing on droplet detachment force (a) and CL and wetted area (b) are shown for different YLCAs. Droplet detachment force is given in (c) in terms of critical ACA (i.e., receding contact angle). Droplet volume and fiber diameter are 0.5 µl, 10 µm, respectively.

2.5. Force Balance Analysis for a Detaching Droplet

To better understand the balance of forces acting on a droplet during detachment, consider a fiber in contact with the droplet as shown in Figure 2.10a (e.g., the red fiber shown on the left side of Figure 2.2d). There are two capillary forces acting on the opposite sides of the fiber along the contact line, and each have a slope equal to the local slope of the AWI. There is also a compression force resulting from the positive pressure inside the droplet (Laplace pressure) distributed over the wetted area of the fiber. The capillary force resisting droplet detachment is the component of the capillary force in a direction opposite to the direction of the external force (see Figure 2.10a), and it varies along the length of the fiber (along the x-direction) depending on the local AWI slope. The total force on each fiber can be obtained by integrating the local capillary forces in the x-direction, i.e.,

$$F_z = \int_{CL} \sigma \sin\beta dx + \int_{WA} p dA \tag{2.6}$$

where β is the angle between the tangent to the AWI and a horizontal plane along the contact line on the fiber, and dA is the elemental wetted area of the fiber projected onto the same horizontal plane (see Figure 2.10a). More specifically, the forces acting on the left and right sides of the fiber can be written as,

$$\begin{aligned} F_z &= F_z^{left} + F_z^{right} = \int_{CL} \sigma \sin\beta_1 dx + \int_{WA} p dA_1 - \int_{CL} \sigma \sin\beta_2 dx + \int_{WA} p dA_2 \\ &= \sigma \int (\sin\beta_1 - \sin\beta_2) \mathrm{dx} + pr \int (\sin\alpha_2 + \sin\alpha_1) \mathrm{dx} \end{aligned} \tag{2.7}$$

where r is fiber radius. Equation 2.7 provides the force acting on each fiber in contact with the droplet, and so the summation of these individual forces should add up to the external body force applied to the droplet. The angles β_1 and β_2 can be calculated using the following equations:

$$\cos\beta_1 = \sin\left(\frac{\pi}{2} + \alpha_1 + \theta^{YL}\right) \tag{2.8}$$

$$\cos\beta_2 = \sin(\frac{3\pi}{2} - \alpha_2 - \theta^{YL}) \tag{2.9}$$

where α_1 and α_2 are the immersion angles on each side of the fiber as discussed earlier. Figure 2.10b shows a few examples of how each fiber in an orthogonal coating contributes to the total capillary force resisting a vertical body force at the moment of droplet detachment. The total detachment force is shown with black symbols versus fiber spacing ranging from 50 to 185 μm. The fibers in contact with the droplet are numbered in the blue bottom-view images (white for fibers in the first layer and green for fibers in the second layer), and their individual contribution to the total force is given with different colors in the bar chart. It is interesting to note in Figure 10b that fibers in the middle of contact area have negligible contribution to the total force resisting droplet detachment when the droplet is in contact with the first layer only. Moreover, the fibers in the second layer contribute more than the fibers in the first layer to the total resistance force against detachment when the droplet is in contact with both layers. It is also interesting to note that a fiber contribution to capillary force may become negative (helping detachment) depending on the local shape and position of the AWI.

As discussed in before, one can obtained the force needed to detach a droplet from a fibrous coating by calculating the individual forces applied by each fiber (using Eq. 2.7) and adding them up together. Equation 2.7 however, is an integral equation that is not easy to solve in the absence of available computational data for each fiber in contact with the droplet. Moving forward with making the calculations more practical, we have developed approximate methods for force calculation as is discussed here in this section.

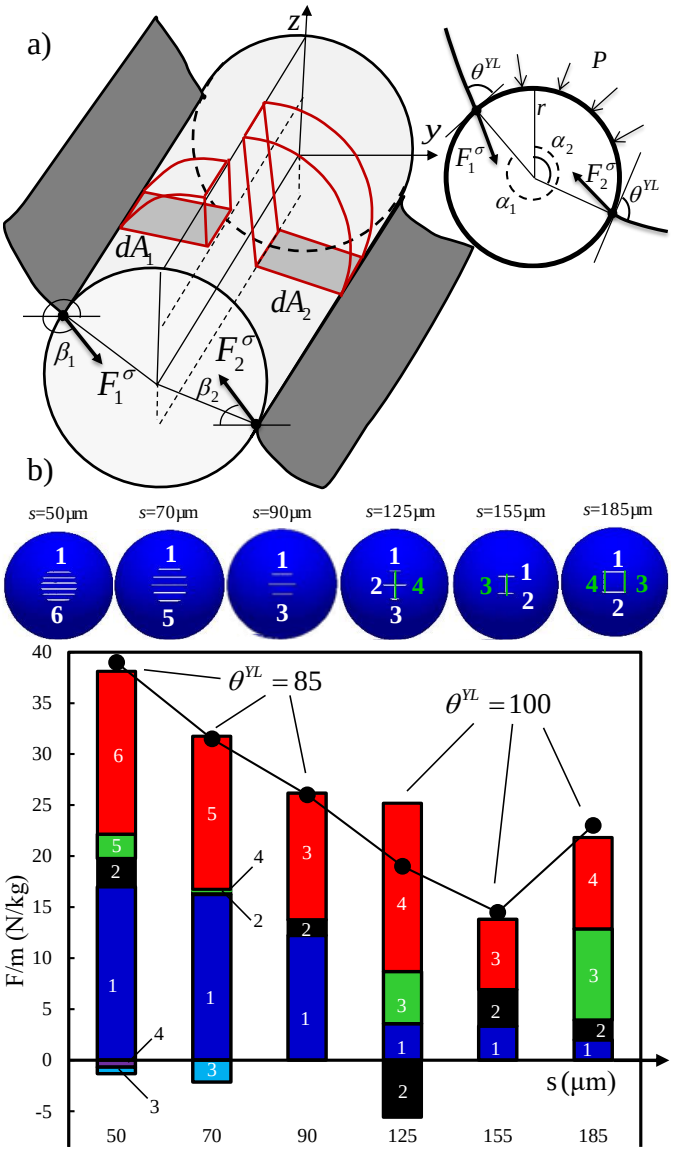

Figure 10: A free body diagram is given in (a) for the forces acting on a fiber in contact with a droplet. Forces acting on each individual fiber in contact with a detaching droplet is shown with different colors in the bar chart given in (b). Each bar represents a different mat with different fiber spacing, and the colors in each bar represent the force acting on the individual fibers in each mat. These fibers are numbered in the bottom view droplet images in each case.

Consider slicing a droplet deposited on a fibrous surface with a horizontal plane as was shown previously in Figure 2.7a. Using a free body diagram as shown in Figure 2.11a, one can rewrite Eq. 2.6 as,

$$F_z = \sigma L \sin \bar{\theta}_{App}^{Cr} - pA \tag{2.10}$$

where L and A are the perimeter and cross-sectional area of the droplet in the slicing plane; $\bar{\theta}_{App}^{Cr}$ is the average critical ACA (obtained using Eqs. 2.4-2.5), and p is the droplet pressure obtained from SE. Figure 2.11b compares predictions of Eq. 2.10 with those directly obtained from SE calculations and good agreement can be observed between the predictions. To be able to predict the force of detachment without needing to conduct a numerical simulation, we have further simplified Eq. 2.10. Keeping in mind that there are only a few geometric parameters can be obtained from a droplet image, we have approximated $\bar{\theta}_{App}^{Cr}$ with the average of the transvers and tangential ACAs (or one of them if both not available from experiment), and also assumed a circular shape for droplet cross-section in the slicing plane. Likewise, d_{cir} is taken as the average of the contact diameters measured from the transvers and tangential views (or one of them if both not available from experiment).

$$F = \sigma\pi d_{cir}\, sin\theta_{App}^{Cr} - p\pi d_{cir}^2/4 \tag{2.11}$$

We have also approximated droplet pressure with $p = \sigma(1/R_1 + 1/R_2) \cong 2\sigma/d_{cir}$ assuming that droplet's in-plane radius of curvature R_2 (not to be confused with droplet diameter) is much larger than that in the out-of-plane direction $R_1 = d_{cir}/2$ (most accurate when ACA is 90 degrees). Predictions of Eq. 2.11 are also added to Figure 2.11b for comparison. It can be seen that this equation estimates the detachment force an accuracy of about 50–60%. Figure 2.11c shows predictions of Eq. 2.11 when used to estimate our experimental detachment force data from Figure 2.4. It can be seen in this figure that predictions of Eq. 2.11 are reasonably good given the level of approximations considered in developing the equation. While not shown in Figure 2.11b for the sake of brevity, it should be mentioned that Eq. 2.11 is more accurate in estimating the simulation data obtained for $\theta^{YL} = 70^o$, but less accurate when used for $\theta^{YL} = 100^o$. This is because $\bar{\theta}_{App}^{Cr}$ is closer to 90 degrees for the former and much larger than 90 for the latter. The same reason explains why

Eq. 2.11 predicts experimental data better than the simulation data obtained for $\theta^{YL} = 85^{o}$ (see the inset in Figure 2.11c). See our published paper for more details on this task [90].

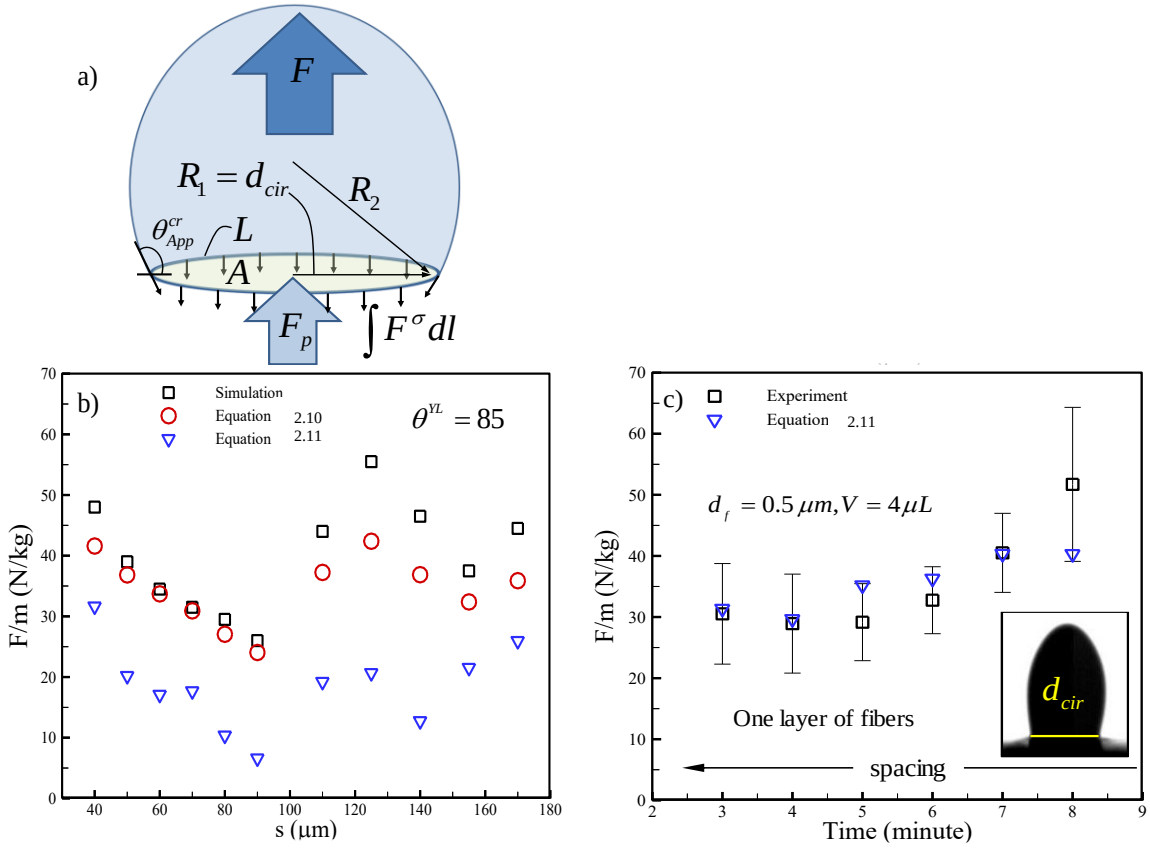

Figure 2.11: A free body diagram is given in (a) for the forces acting on a droplet at equilibrium on a surface. Comparison between droplet detachment forces versus fiber-to-fiber spacing obtained from numerical simulations, Eq. 2.10, and Eq. 2.11 is given in (b). Comparison is also given between predictions of Eq. 2.11 and our experimental data (c). The inset in (c) shows how d_{cir} was obtained from droplet images right before detachment.

2.6 Conclusions

The force needed to detach a droplet from a sticky hydrophobic fibrous surface is investigated in this chapter experimentally and computationally. The experiments were performed using ferrofluid droplets deposited on electrospun PS coatings comprised of orthogonally-layered aligned fibers, and the simulations were conducted for conceptually similar systems but after some

simplifications. The following conclusions were drawn from our combined experimental-computational study. It was observed from the simulations and experiments that droplet detachment force decreases with increasing fibers' YLCA. It was also observed that droplet detachment force decreases or remains relatively constant with increasing fiber-to-fiber spacing depending on the number of layers of fibers in contact with the droplet. The variations are more predictable for when Cassie droplets are in contact with only one layer of fibers, but interactions become more complicated when fibers in the lower layers come into contact with the droplets or when the droplets are not in the Cassie state. Analyzing the individual capillary forces provided by the fibers in contact with a droplet, it was found that fibers in the middle of the surface wetted area do not play a significant role in keeping the droplet on the surface (negligible relative contribution in resisting droplet detachment). Contribution of the individual fibers in resisting droplet detachment becomes more complicated and unpredictable when the droplet is in contact with more than one layer. No simple quantitative relationship was observed between droplet detachment force and droplet equilibrium ACA, or droplet CL (or surface wetted area). However, the trends of variation of these parameters with fiber-to-fiber spacing or YLCA seemed to agree with those of detachment force. A more clear relationship was observed between droplet detachment force and droplet critical ACA (also referred to as receding contact angle). Using the balance of forces acting on the detaching droplet, an easy-to-use expression is developed to estimate droplet detachment force from a fibrous surface. The predictions of this simple equation are compared with our experimental and computation results and reasonable agreement was observed.

Chapter 3. Measurement of the Force Required to Move a Droplet on a Hydrophobic Fibrous

3.1. Introduction

The focus of the work presented here, is to study droplet mobility on hydrophobic fibrous surfaces with low droplet mobility. Fibrous coatings are usually made by depositing fibers on top of one another. While a droplet can exhibit high apparent contact angles (ACAs) on such surfaces, its adhesion to the surface may be very unpredictable. The root cause of this problem is the empirical nature of the current surface manufacturing procedures in which a fibrous surface is first manufactured and then it is tested for droplet mobility. An ambitious but yet logical alternative to the traditional manufacturing approach would be to first design and test the surface virtually, and go on to then manufacture it if the performance was acceptable. This futuristic approach obviously requires detailed information about the impact of surface micro-scale morphology on the forces acting on a droplet. The study presented in this paper is therefore aimed at providing additional insight into the physics of droplet–fiber interactions specific to fibrous hydrophobic coatings. Similar approach for experiment and simulation to previous task is considered here.

3.2. Experimental Results

As mentioned earlier, the force required to move a droplet on the surface of our PS coatings was measured using a sensitive scale on which the coatings were placed in the vertical position. To start, a ferrofluid droplet was gently deposited on the coating in the horizontal position, and the coating was then rotated 90 degrees and mounted on the scale. A continuously increasing magnetic force was then applied to the droplet by lowering the magnet while recoding droplet deformation using a high-speed camera.

In studying droplet mobility on fibrous coatings, we limit our work to droplets that have not penetrated deep into the coatings to reach the underlying substrate. While we realize that there exists a series of partially-wetted transition states between the fully-dry Cassie and fully-wetted Wenzel states, we refer to such droplets as the Cassie droplets to distinguish them from the droplets that have come into contact with the substrate (referred to here as the Wenzel droplets) for the sake of simplicity. Since it is difficult to visually determine whether a droplet has come into contact with the substrate during an experiment, we use the ACAs, sliding force, and droplet residue on the coating in judging the state of the droplet as shown in Figure 3.1. This figure reports droplet sliding force and ACAs on electrospun PS coatings comprised of two, three, and four orthogonal layers of parallel fibers (3 min electrospinning per layer). We have also included the contact angle hysteresis (CAH) for comparison.

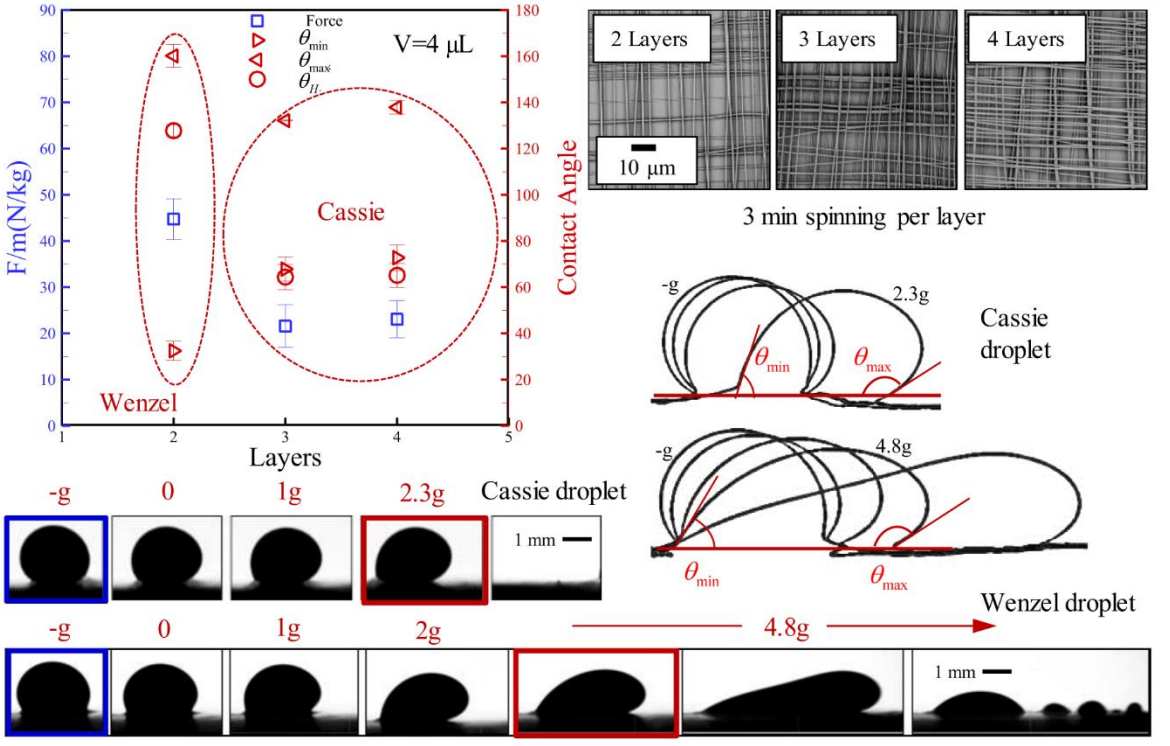

Figure 3.1 Droplet sliding force and critical CAs are given versus number of electrospun layers. Example snapshots of droplet deformation and sliding are also shown for Wenzel and Cassie droplets with a volume of 4µL. Droplet profile are extracted and overlaid for comparison.

It can be seen that the force needed to move the droplet over the two-layer coatings is almost two times higher than that needed to slide the droplet over the three- or four-layer coatings. Likewise, the CAH is greater on the two-layer coatings. This information indicate that ferrofluid droplets with a volume of 4 µL stay in the Cassie state on the three- or four-layer coatings but they transition to the Wenzel state when deposited on the two-layer coatings. This argument is also supported by the images obtained from droplet motion and the presence or the lack of a measureable droplet residue on the surface. As can be seen in the bottom-right image in Figure 3.1, a Wenzel droplet breaks up into smaller droplets as it moves over the surface, the so-called pearling effect.

Figure 3.2 shows sliding force and CA for droplets with a volume in the range of 2 µL to 7 µL on coatings comprised of three orthogonal layers of parallel PS fibers each spun for 5 minutes (the CAs will be later used for Figure 3.7). It can be seen that sliding force per droplet mass is smaller for larger droplets. From a design perspective, it is important to explore the importance of fiber–fiber spacing (inversely proportional to spinning time per layer) and layer configuration on droplet mobility. Figure 5 shows the sliding force and CAs for a droplet with a volume of 4 µL placed on PS coatings with different fiber–fiber spacing. The results given in Figure 5a are for coatings made only of one layer of fibers (mounted on a stand to avoid contact with the underlying substrate), while those shown in Figure 3.3b are obtained with three-layer coatings. It can be seen that sliding force and CAH increase with decreasing fiber spacing.

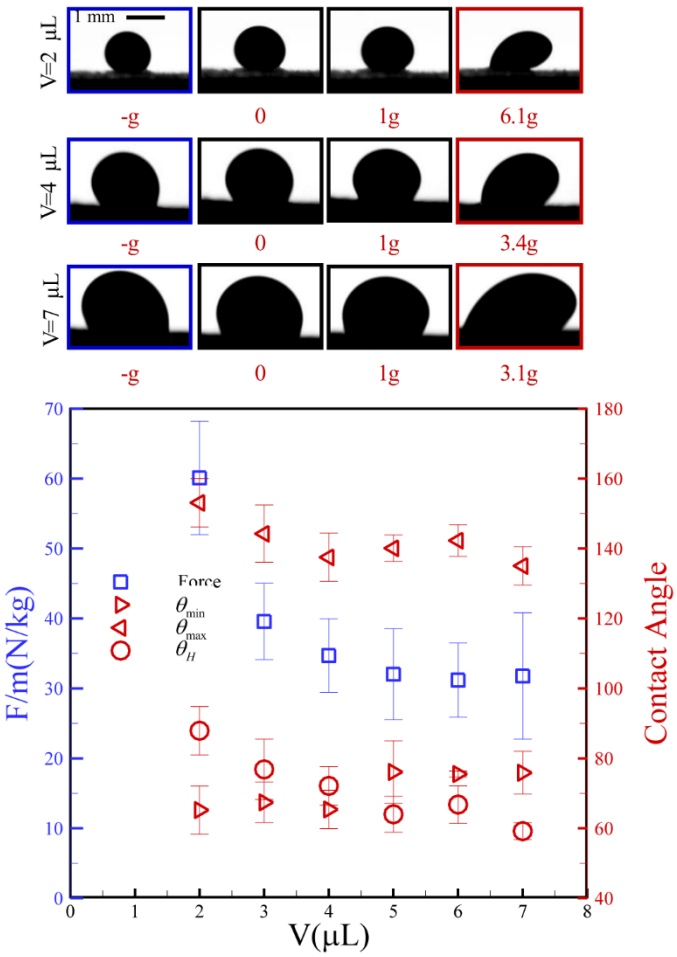

Figure 3.2. Droplet sliding force and CAs are given versus for droplet volume. The coatings used for the experiments were composed of 3 orthogonal layers of electrospun parallel fibers with 5 min fiber spinning per layer. Example snapshots of droplet deformation are also shown for three different droplet volumes.

It is interesting to note that sliding force and CAH values reported in Figure 3.3b are greater than their counterparts in Figure 3.3a. This indicates that for the droplet–fiber combinations considered in these experiments, the droplets penetrate deep into the coatings enough to come into contact with the fibers below the first layer. Additional discussion about the role of individual fibers and the effects fiber–fiber spacing is given in the last section (see Figure 3.6 and 3.7).

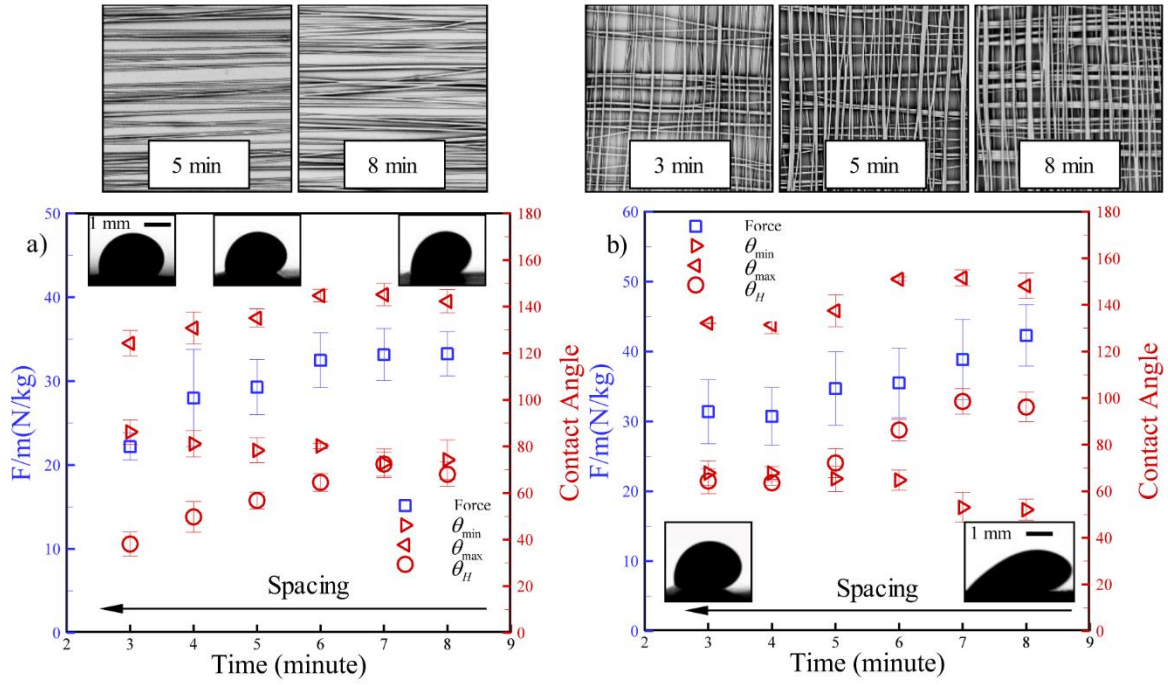

Figure 3.3. Droplet sliding force and CAs are given versus spinning time (inversely proportional to fiber-to-fiber spacing) for a droplet with a volume of 4 µL on one-layer coatings made of aligned electrospun fibers in (a) and orthogonally layered aligned fibers in (b). The insets show droplet shape at the moment of detachment.

3.3. Simulation Results

Unless otherwise stated, the fiber diameter and droplet volume considered for the computational component of this research are 10 µm and 0.5 µL, respectively. Simulations start by first obtaining droplet's equilibrium shape on horizontal coatings (with gravity normal to the plane of fibers). Mimicking droplet on a vertical coating as in the experiment, we then set the gravity to zero but apply an external force to the droplet in a direction parallel to the plain of coating. In simulating sliding force, we incrementally increase the force on the droplet (with an arbitrary increment of $\Delta g_z = 0.5$ N/kg) until no equilibrium shape and position can be obtained for the droplet. The largest body force at which an equilibrium shape is obtained (plus an increment of Δg_z) is then taken as the force required to slide the droplet on the surface. Note that the simulation method used

in this work cannot be used to model the dynamics of droplet sliding or the volume of the droplet residue left on the fibers after detachment.

Figure 3.4a-3.4c shows examples of overlaid droplet shapes on fiber coatings with different properties. The blue-colored droplets are under the influence of gravity only (i.e., horizontal equilibrium position) while the red-colored droplets represent droplets on a vertical coating (exposed to an external body force parallel to the plain of fibers). The red-colored droplets are at their final state of equilibrium, i.e., they are about to slide on the surface. Footprint of each droplet on the coatings (portion of the droplet in contact with the coating) is also included for each case in Figure 3.4 with matching colors. Fibers in the first (top) and second layers are shown with green and dark-red colors, respectively. The droplets shown in Figure 3.4a are in contact with only one layer of fibers (s=70 μm), whereas those shown in Figure 3.4b and 3.4c are in contact with both layers of fibers (s=140 μm and s=125 μm). The external force is normal to the green fibers in Figures 3.4a and 3.4b, but it is parallel to the green fibers in Figure 3.4c. Effects of external body force on CL, fibers' wetted area (Figure 3.4d), and CAH (Figure 3.4e) are also presented for quantitative comparison. It can be seen that increasing the body force increases the CAH but decreases CL and fibers wetted area which were expected conceptually but never quantified for fibrous surfaces.

Figures 3.5a–3.5d show the effects of fiber spacing and YLCA on droplet 3-D shape and footprint on the coatings in presence (red-colored) and absence (blue-colored) of a parallel external force. Coating's wetted area, droplet CL, CAH, and droplet sliding force (parallel to the surface but perpendicular to the fibers in the top layer) calculated and given in Figures 3.5e–3.5g as a function of fiber–fiber spacing. Our results indicate that sliding force is lower on coatings with high fiber–fiber spacing (regardless of number of layers or YLCA of the fibers). This is because a droplet on

a coating with a greater fiber spacing is in contact with less number of fibers (smaller capillary force).

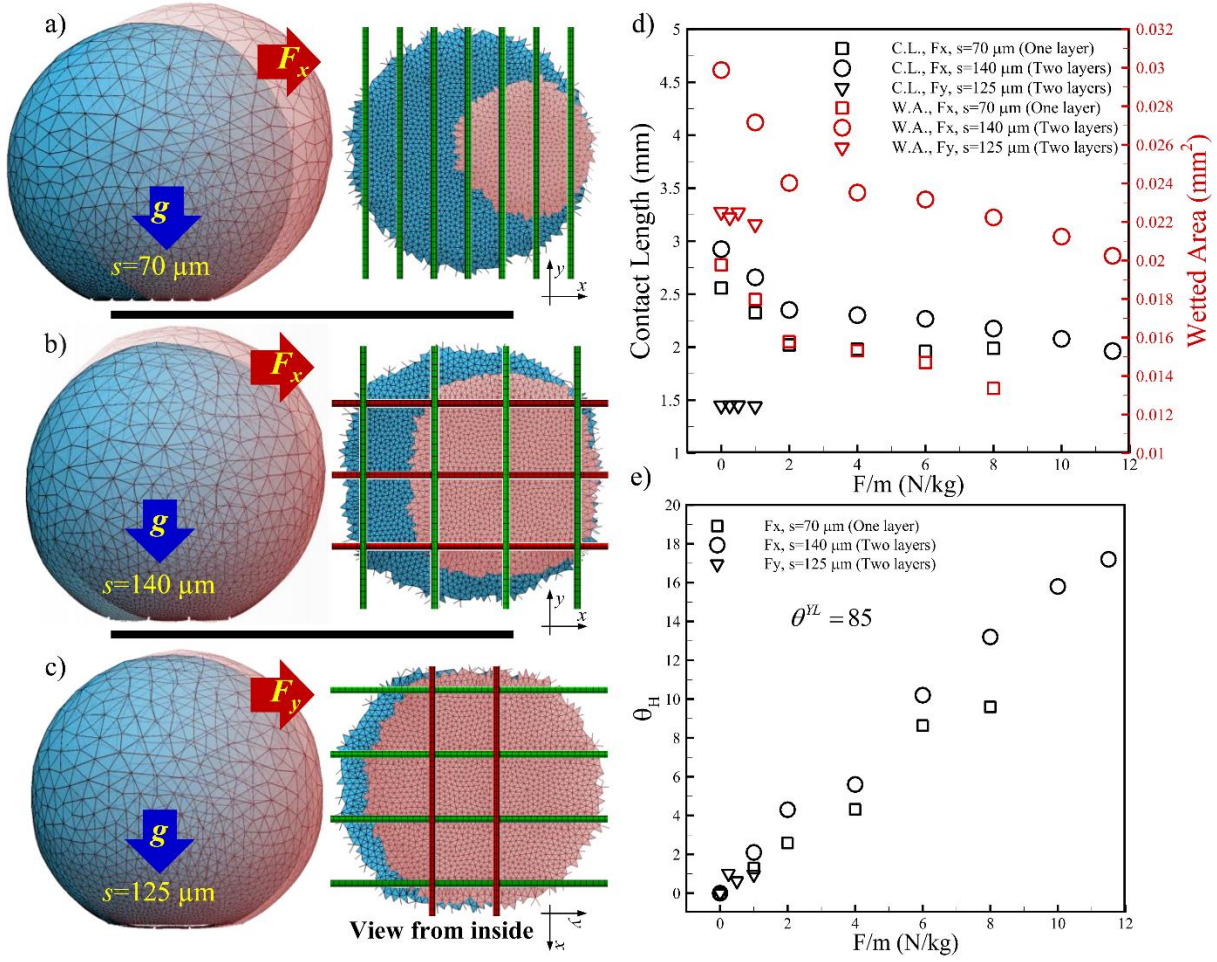

Figure 3.4. Droplet profile and bottom views are given in (a), (b) and (c) for droplets on coatings with different fiber–fiber spacing. Effects of increasing horizontal body force (leading to droplet sliding) on CL and fiber wetted area (d), and CAH (e) are also given for coatings with three different fiber spacing but an identical YLCA of 85 degree.

It can also be seen that sliding force is less on coatings comprised of fibers with a higher YLCA. The simulations also revealed that sliding force increases rapidly if the droplet comes into contact with the fibers in the second layer (i.e., mobility is less on coatings that allow the droplet to penetrate into the structure). Qualitative agreement can also be seen between our experimental data

(Figure 3.3) and the computational results (Figures 3.4 and 3.5) despite the differences in dimensions of the fibers and the droplets. It is worth noting that the sliding forces obtained experimentally for our electrospun coatings are larger than those obtained from the simulations. This is because the number of fibers in contact with a droplet deposited on an actual electrospun coating is more than that in the virtual coatings used in the simulations.

When the external force is applied in a direction parallel to the fibers in the first layer (i.e., in the *y*-direction), the sliding forces are about an order of magnitude smaller than their counterparts in the *x*-direction. In fact, the sliding force is zero for droplets that do not reach the fibers in the second layer in this case (in the absence of viscous forces and CL pinning).

It is also interesting to mention that sliding forces in the *y*-direction are less than *g*, which means that the droplets can roll off by simply tilting the surface (which was not the case when the external force was in the *x*-direction). This confirms that droplet mobility over a fibrous surface strongly depends on the relative angle between the fibers in contact with the droplet (fibers near the top of the surface) and the direction of the external force.

3.4. Force Balance Analysis for Droplet Sliding Force

An unanswered (or perhaps partially answered) question in the literature has been the relative contributions of the advancing and receding sides of a droplet in resisting against droplet motion. In this section, we use our numerical simulations to shed some more light on this issue and help better understand the role of individual fibers in resisting droplet mobility.

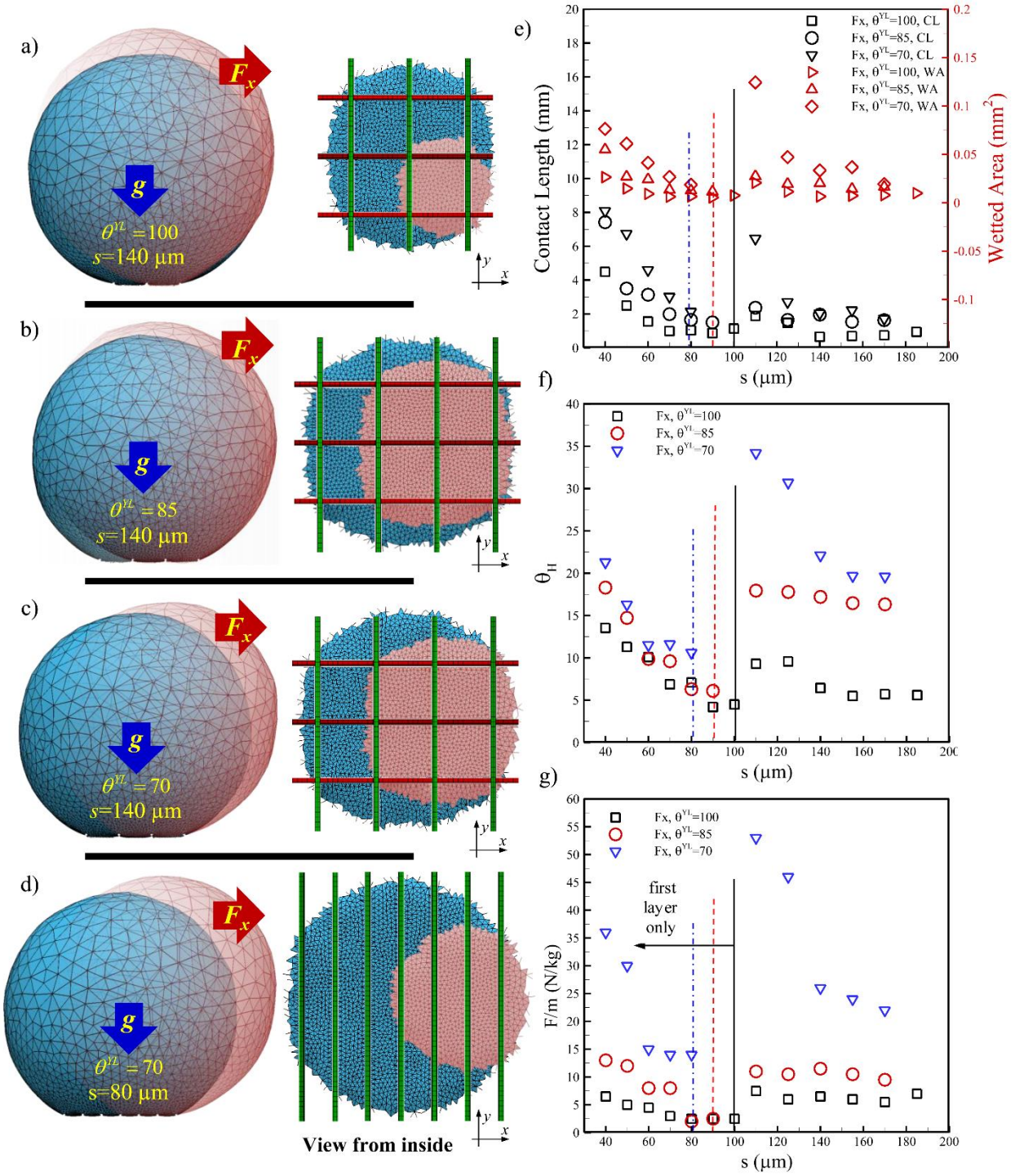

Figure 3.5. Droplet profile and bottom views are given in (a) through (d) for a droplet on coatings with different fiber spacing. Effects fiber spacing on CL and wetted area (e) and CAH (f), and sliding force (g) are of also given for comparison. Droplet volume and fiber diameter are 0.5 µl, 10 µm, respectively.

With the numerical simulation data available, one can study how each individual fiber in contact with a droplet contributes to the force resisting against the droplet motion. Figure 3.6a shows a schematic drawing of the contact between a fiber and a droplet. The capillary forces act on the opposite sides of the fiber in a direction tangent to the AWI along the fiber axis (the *y*-direction here) with a slope that is equal to the local slope of the AWI. Pressure forces, caused by the elevated pressure inside the droplet, act normal to the local curvature of the solid surface on the fiber's wetted area (shown in red in Figure 3.6a). The fiber resistance to droplet motion is the summation of the components of the capillary and pressure forces in the direction opposite to that of the droplet motion, i.e.,

$$F_x = \int_{CL} \sigma \cos\beta dx + \int_{WA} pdA \tag{3.1}$$

where β is the angle between the tangent to the AWI and the horizontal plane along the CL on the fiber, and dA is the elemental wetted area of the fiber projected onto a vertical plane as shown in Figure 3.6a. Expanding Eq. 3.1 using geometrical information given in Figure 3.6a, we obtain,

$$\begin{aligned} F_x = F_x^L + F_x^R &= \int_{CL} \sigma \cos\beta_1 dy + \int_{WA} pdA_1 - \int_{CL} \sigma \cos\beta_2 dy - \int_{WA} pdA_2 \\ &= \sigma \int (\cos\beta_1 - \cos\beta_2)\, \mathrm{dy} + pr \int (\cos\vartheta_2 - \cos\vartheta_1)\, \mathrm{dy} \end{aligned} \tag{3.2}$$

where r is the fiber radius. The superscripts L and R refer to left and right sides of the fiber as can be seen in Figure 3.6a. Applying Equation 3.2 to all fibers in contact with the droplet results in the total resistance of the coating to droplet motion. Using Figure 3.6a, the angles β_1 and β_2 can be written in terms of immersion angles on each side of the fiber (ϑ_1 and ϑ_2), i.e.,

$$\cos\beta_1 = \sin\left(\frac{\pi}{2} + \vartheta_1 + \theta^{YL}\right) \tag{3.3}$$

$$\cos\beta_2 = \sin\left(\frac{3\pi}{2} - \vartheta_2 - \theta^{YL}\right) \tag{3.4}$$

The simulations reported earlier are considered here again in Figure 3.6b for its simplicity (there are only three fibers in contact with the droplet) to further analyze the forces between a droplet and its underlying fibers. As mentioned earlier, the net force exerted on each fiber is the resultants of the capillary (along the CL) and pressure (over the wetted area) forces on the left and right sides of the fiber. Table 3.1 compares these forces with one another for the case shown in Figure 3.6b. It is interesting to note that the fiber in the middle (Fiber 2) does not contribute to the total force acting on the droplet (forces cancel each other due to geometrical symmetry). The fiber on the advancing side (Fiber 3) makes the strongest resistance against droplet motion, while the fiber on the receding side (Fiber 1) tends to help the droplet to move. Note that the length of the CL is quite different on the receding and advancing sides of the droplet (CL is longer on the fiber on the advancing side as can be seen in the magnified images in Figure 3.6b).

Table 3.1. Force components for a droplet with a volume of 30 µL on 3-D printed parallel fibers with a diameter of 362 µm and fiber spacing of 898 µm.

$f = F_x / m$	f_σ^L	f_σ^R	f_p^L	f_p^L	f_{net}^L	f_{net}^R	f_{net}
Fiber 1 (receding)	20	-25	-5	17	15	8	**7**
Fiber 2 (middle)	26	-26	-15	15	11	11	**0**
Fiber 3 (advancing)	26	-30	-14	6	12	24	**-12**
Resultant force	Summation of all three fibers						**-5**
Experiment	$g\sin\alpha, \alpha = 30$						**4.9**

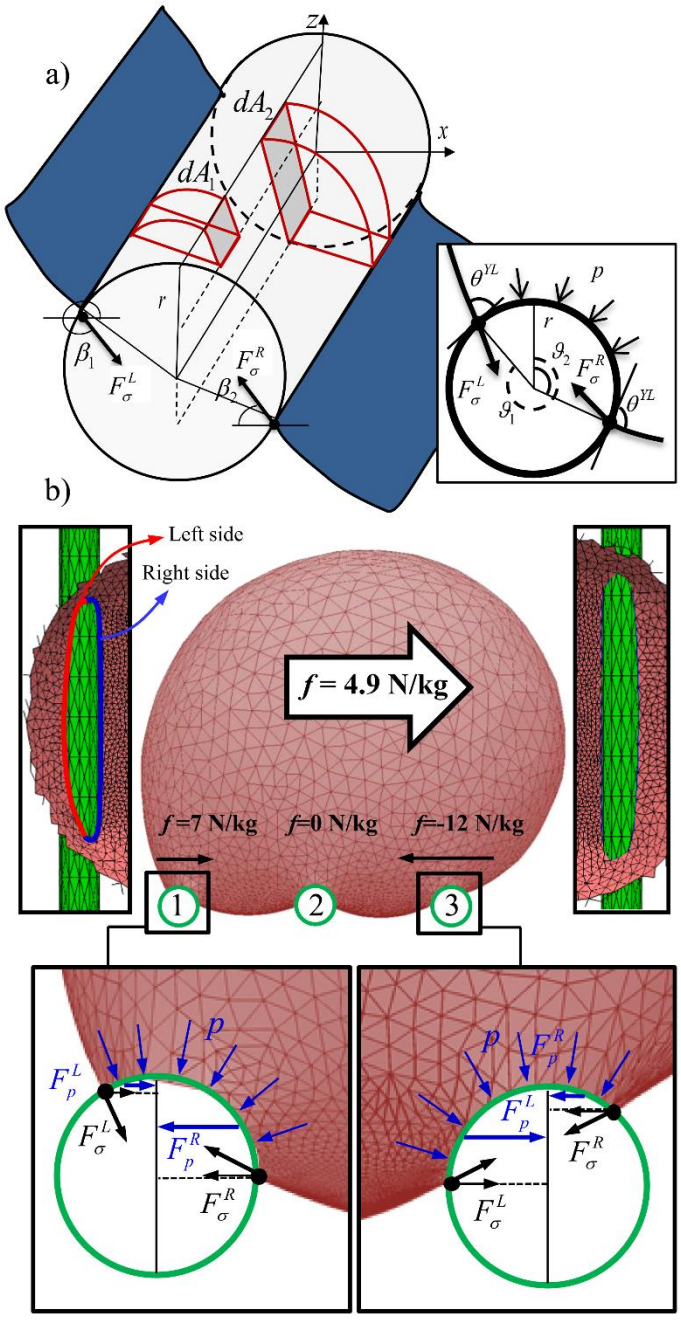

Figure 3.6. A free body diagram is given in (a) for the forces acting on a fiber in contact with a droplet. (b) Simulated force components are given for a droplet with a volume of 30 µL on the 3-D printed fibers (with diameter of 362 µm and fiber spacing of 898 µm).

This observation may seem to contradict the commonly accepted conclusion that the receding end of a droplet plays the most important role in controlling droplet mobility. However, the conclusion

was probably reached for droplets on surfaces that allow CL pinning (e.g., surfaces made of microfabricated sharp-edged posts).

Coming back to the more complicated case of droplet on virtual coatings with orthogonal fibers, we present force per fiber for four different coatings in Figure 3.7. The bar chart of Figure 3.7a shows the contribution of each individual fiber in the total force against droplet motion (the total force shown with black circles) for a few virtual fibrous coatings with different fiber–fiber spacing (from Figure 3.5). The bar segments in Figure 3.7a are colored differently for different fibers. Figure 3.7b shows the droplet footprints on coatings with different fiber–fiber spacing values of 50 µm, 70 µm, 125 µm, and 170 µm. Note that, fibers shown in red provide no resistance against droplet motion in the *x*-direction (they are parallel to the *x*-direction). It is interesting to note in Figure 3.7a that fibers on the droplet's receding and advancing sides play the main role in resisting against droplet motion. In this figure, the positive forces help droplet motion while the negative force resist against it.

An alternative approach to using Eq. 3.2 for sliding force prediction is to slice the droplet at a location slightly above the surface and to consider the balance of forces acting on the droplet as shown in Figure 3.8a (the distance between the fibers and the slicing plane is exaggerated for illustration). The new approach does not provide any fiber-level information (see Figure 3.7 and its discussion), but it is more practical as will be seen later in this section. Figure 3.8a also shows the capillary forces (black arrows) acting on the sliced droplet. The capillary forces are projected onto the slicing plane and are shown from below. The red arrows in this figure are the *x*-components of these planar forces. Note that, the pressure forces acting on droplet cross-section have no components in the *x*-direction.

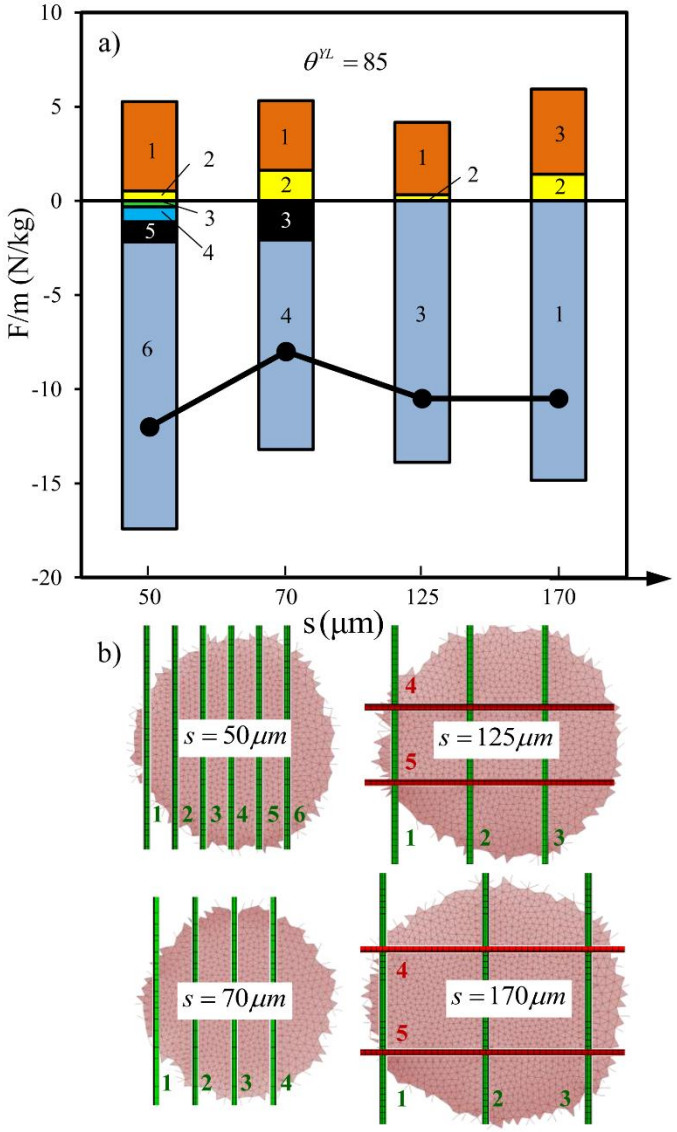

Figure 3.7: Forces acting on each individual fiber in contact with a droplet at the final state of equilibrium under an external horizontal force (a). Each bar represents a coating with a different fiber spacing, and the colors in each bar represent the force acting on the individual fibers in each coating (b).

The sliding force can therefore be calculated as the *x*-component of the force obtain using Eq. 3.5,

i.e.,

$$F_x = \int_{CL} \sigma \cos\theta_{app}^{cr} dl \tag{3.5}$$

where θ_{app}^{cr} is local apparent contact angle of the droplet (around the 3-D contact line) at its final equilibrium state before moving. Figure 3.8b compares the sliding force from simulations (Figure 3.5) with the predictions of Eq. 3.5. To do so, we sliced the simulated droplets at a distance of 6*d* above the top surface of the fibers to extract θ_{app}^{cr} and CL data for Eq. 3.5. Good agreement can be seen between the actual simulation data (black squares) and those obtained from the above slicing method (green circles), as expected.

As mentioned earlier in the Introduction, one can estimate the droplet sliding force on a surface using Eq. 1.3. This equation however requires droplet's advancing and receding CAs as well as the width of the droplet's footprint on the surface w as input (assuming the empirical correction factor to be $k = 1$). While in principle droplet's width right before sliding w^{cr} should be used in Eq. 1, better agreement with simulation results was observed when we used footprint's width in the absence of the magnetic force w^0 in the equation (see Figure 3.8b). The inset in Figure 3.8b shows the droplet footprint on the surface as a function of in-plane body force. It can be seen that w decreases (though not monotonically) with increasing the in-plane body force on the droplet.

The experimental counterparts to the computational results shown in Figure 3.8b are given in Figure 3.8c for a droplet with a volume of 4 μL on a single layer of aligned electrospun fibers (the experiments reported in Figure 3.3a). Since droplet footprint on the surface can be approximated as being circular in the absence of an in-plane body force, we used droplet length in place of droplet width when measuring w^0. To measure w^{cr}, the droplet was imaged from behind as it was pull up by the magnet. The inset in Figure 3.8c shows an example of such images obtained under different in-plane body forces (overlaid on top of each other for comparison). It can again be seen that Eq. 1.3 tends to underestimate the sliding force when $w = w^{cr}$ is used in the equation for footprint width. Equation 1.3 however, provides reasonable predictions with $w = w^0$.

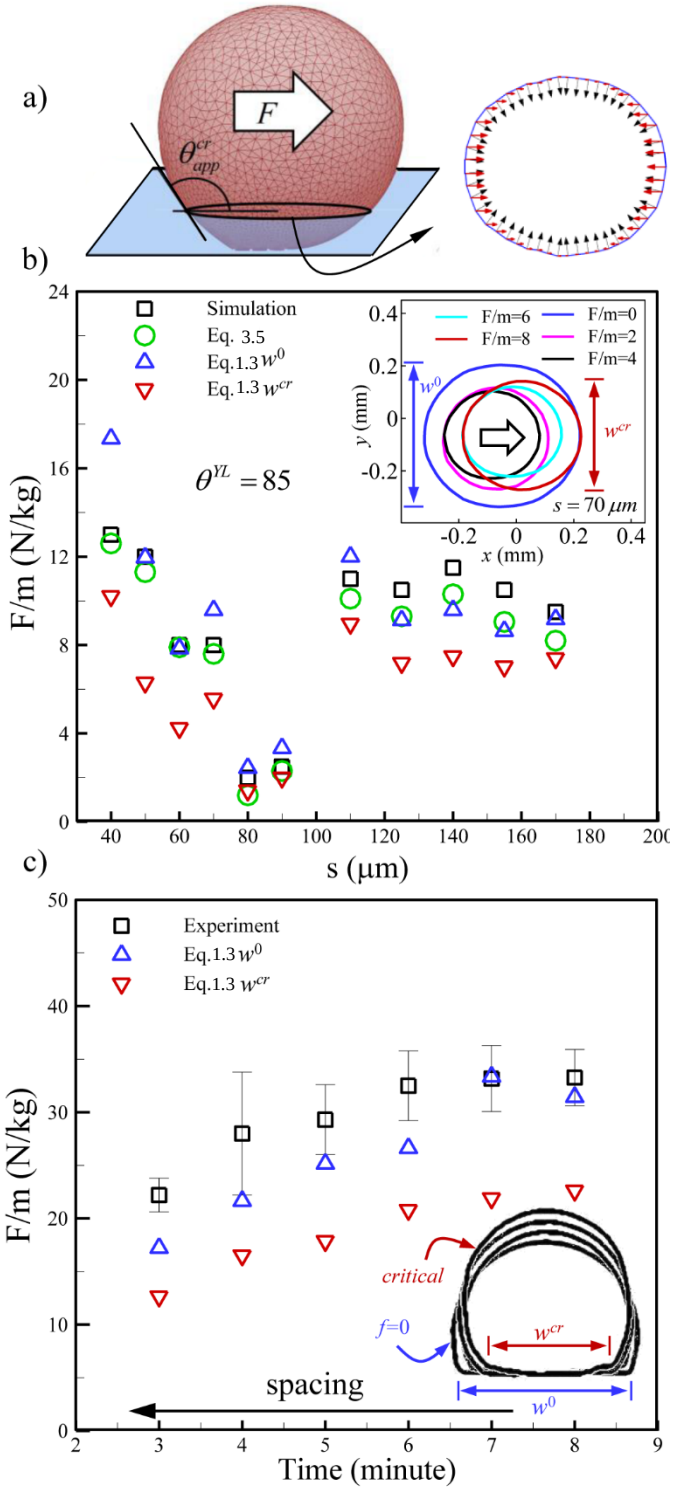

Figure 3.8. Droplet slicing method on the capillary forces at the cross section are shown in (a). Comparison between droplet sliding forces obtained from numerical simulations, Eq. 3.5, and Eq. 1.3 is given in (b). Comparison between predictions of Eq. 1.3 and our experimental data is given in (c).

Regardless, we believe droplet footprint dimensions on the surface right before detachment (be it the width or other dimensions) are more logical parameters to use in predicting the sliding force. The reported inaccuracies in predictions obtained from Eq. 1.3 seem to be inherent to this oversimplified empirical equation (hence the empirical correction factor of $1 < k < 3.14$ as recommended in the literature). See our published paper for more details on this chapter [91].

3.5. Droplet Detachment from Mats with Random Fibers

The force needed to detach a droplet from a fibrous surface made of parallel or orthogonal fibers with different number of layers was investigated before. In this section, the out-of-plane force (vertical force) and in-plane (horizontal force) are measured for a mat with randomly oriented fibers (see Figure 3.4). The detachment force in this case is almost constant independent of the electrospinning time. For PS coatings made of aligned fibers, depending on the spacing between the fibers (electrospinning time) or the number of fiber layers, we obtained out-of-plane and in-plane detachment forces ranging from 22 to 60 N/kg, respectively. These forces however were found to be about 50 and 38 N/kg for mats with random fibers.

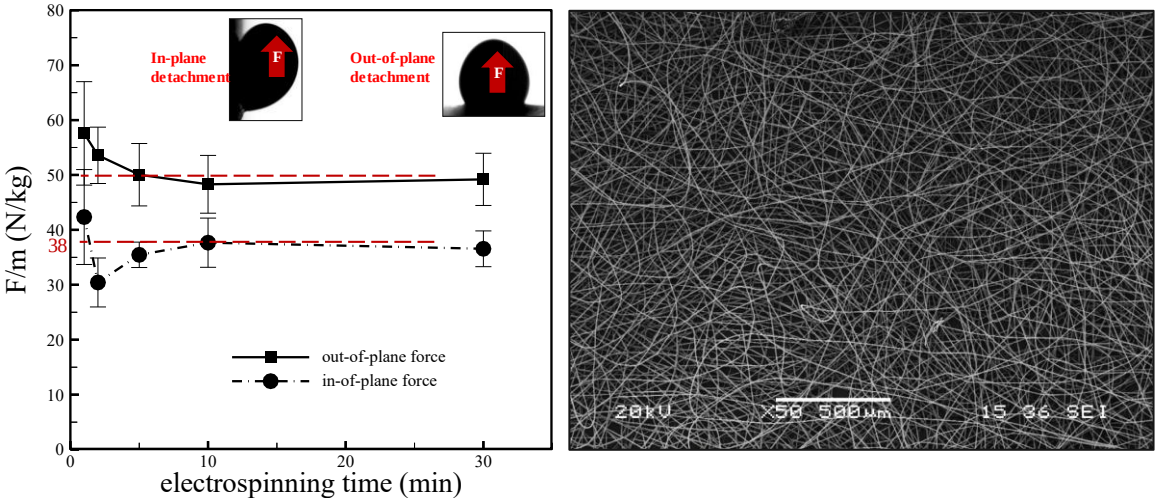

Figure 3.9: Droplet in-plane and out-of-plane detachment forces as a function of electrospinning time for a PS mat with randomly deposited fibers.

3.6. Conclusions

Droplet mobility on electrospun PS coatings is studied experimentally and computationally in this chapter. To simplify the otherwise very complicated problem, we limited the orientation of the fibers to the x and y directions. Depending on the spacing between the fibers (and of course fiber and droplet diameters), a droplet on an electrospun PS coating can be at the Cassie state, at the Wenzel state, or at a transition state in between these extremes states. It appeared from our experiments that the Cassie (or near-Cassie) droplets leave a much smaller residue on the surface after sliding compared to the Wenzel (or near-Wenzel) droplets. The Wenzel droplets have to break up into two or more volumes before they can roll on the surface. Our results also indicate that Cassie droplets seem to require a smaller body force to roll on the surface. In the work presented here, we focused mostly on the Cassie droplets. The force needed to move a droplet on the surface of an electrospun PS coating is usually greater than the weight of the droplet (i.e., droplet does not roll off by tilting the surface). Our results indicate that droplet mobility is generally higher when the spacing between the fibers is larger. However, this depends on whether or not the droplet is in contact with the first layer of fibers. Excessive spacing between the fibers can lead to droplet penetration into the coating (even as small as one fiber diameter deep) to result in a significant reduction in droplet mobility. Our study quantified the effects of droplet volume (as well as fiber spacing or YLCA) on the force needed to roll the droplet on the surface. An in-depth analysis was presented for the effects of external body force on droplet contact line or fibers' wetted area. Calculating the force exerted on a droplet placed on a fibrous surface, it was found that the fibers on the receding and advancing sides of the droplet play the most important roles in determining the force needed to roll the droplet on the surface.

Chapter 4. Analysis of Droplet Penetration into a Nonwoven Fabric

4.1 Introduction

In this context, this work is the first to report the use of a magnetic field in quantifying the resistance of a non-wetting fibrous material to droplet spontaneous penetration. In our study however, no inertia is considered for the droplets so that a quasi-static approach could be considered to simplify the analysis. More specifically, we use a permanent magnet to measure the force needed to make a ferrofluid droplet penetrate into a thin non-wetting fibrous material. The measured forces are then used to relate the microstructural and wetting properties of the media to their ability to repel droplets of different properties. The measured body forces can, of course, be converted to their air (or liquid) drag force counterparts for comparison to a typical coalescence filtration experiment, if needed. The method for experiment and simulation is similar to chapter 1.

4.2. Simulation–Experiment Comparison

In this section, we present experimental and computational results obtained for 3-D printed (5th Gen Makerbot Replicator) mesh-like two-layer structures comprised of parallel fibers (with a fiber diameter of 345 μm and fiber spacing values of 905 and 1155 μm) layered orthogonally on top of one another (see Fig. 4.1). The printed fibers were coated with Ultra-Ever Dry solution from Ultratech to impart surface hydrophobicity (with an YLCA of about 120 on a microscope slide). Experiment with the ordered structures (equally-spaced large fibers of almost-identical diameters) allows us to produce a side-by-side simulation–experiment comparison (such a comparison cannot be made for a droplet on an electrospun fibrous coating, as excessive computational resources are needed to model a macroscopic droplet on submicron-sized PS fibers).

When a droplet sits on a hydrophobic porous surface, a meniscus forms inside the pores of the surface if the pressure inside the droplet is higher than the pressure of the fluid inside the pores (e.g., air). Generally speaking, a droplet does not penetrate too deep into a hydrophobic (oleophobic) surface when gravity is the only external force acting on the droplet. Applying an external body force increases the pressure inside the droplet and that leads to further penetration of the meniscus into the pores. The pressure at which a spontaneous droplet penetration starts is referred to as the critical pressure in this work.

Figures 4.1a and 4.1b show the equilibrium shape of a droplet with a volume of 7 µL on the mesh-like structures (see Fig. 4.1c) with fiber–fiber spacing of 905 and 1155 µm, respectively. Droplet shapes from simulation and experimental are compared with each other in these figures (gravity is the only body force acting on the droplets). While the predicted droplet apparent contact angles (ACAs) tend to be smaller than those predicted, good overall agreement between the simulation and experiment is noticeable. We believe that surface roughness (from 3-D printing or from spray coating) is the reason for the discrepancy between predicted and measured ACAs; the simulated droplets (in the absence of roughness or pinning effect) show slightly deeper meniscus penetration into the structure. Also note in Fig. 4.1 that, the 3-D printed fibers do not have a perfectly circular cross section.

Figures 4.1d and 4.1e present the droplet equilibrium shapes in the presence of an increasing magnetic body force. Good general agreement can again be seen between the simulation and experiment. The smallest body force needed for the droplet to spontaneously penetrate in each mesh was obtained from the simulations and experiments, and is given in the figure (2.7g and 7.6g for meshes with a fiber spacing of 1155 µm and 905 µm, respectively). Note that, as SE equations are time-independent, our simulations are limited to conditions where an equilibrium shape can be

expected for the droplet, i.e., spontaneous droplet flow through the structure cannot be simulated. Also note in the experimental images of Fig. 4.1e that, due to 3-D printing imperfections, the droplet often tends to flow only through one of the openings between the fibers (where the resistance to the flow is minimum).

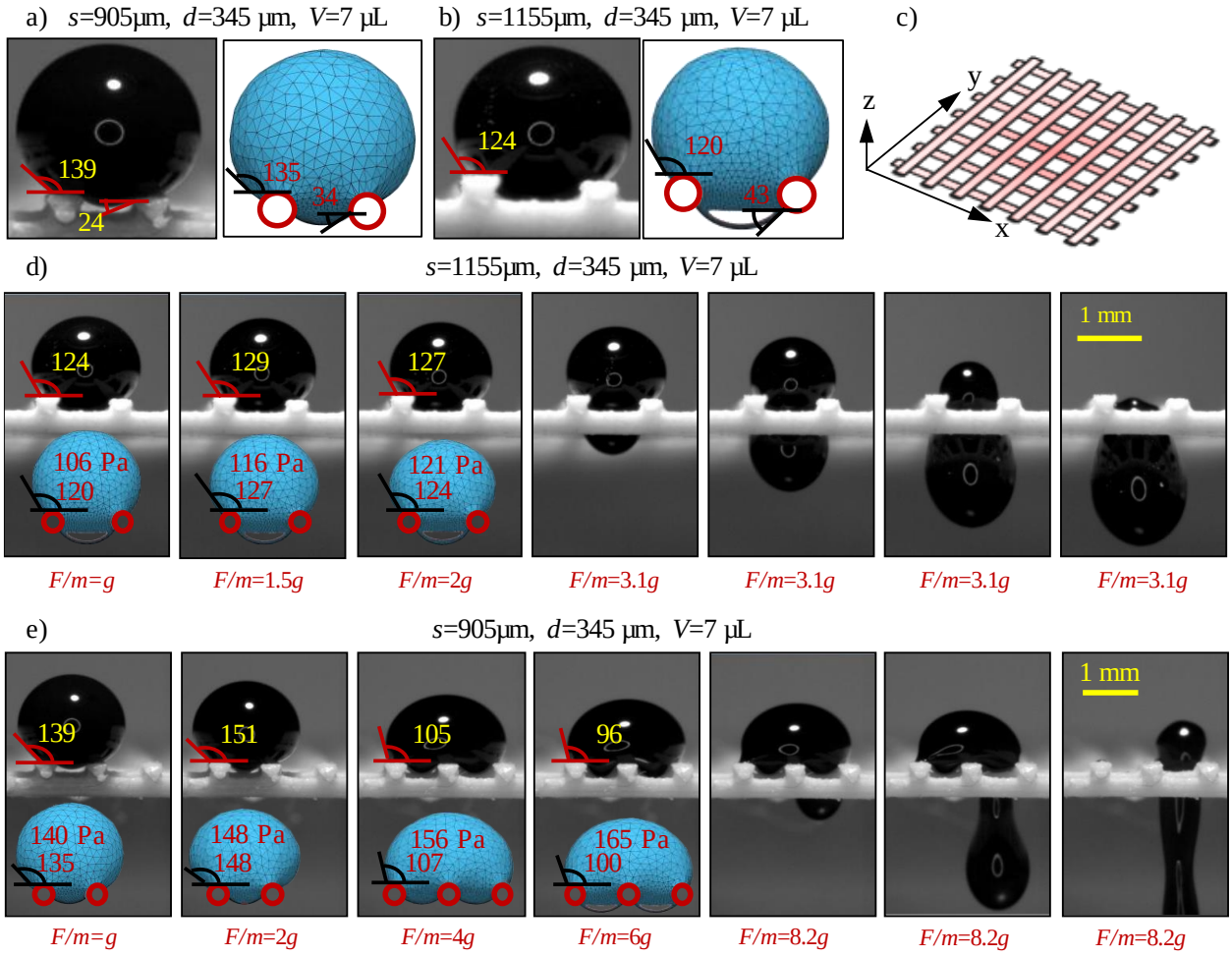

Figure 4.1: Images in (a) and (b) show the under-gravity equilibrium shape of a droplet with a volume of 7 µL on the mesh-like structures, shown in (c), with a spacing of 905 and 1155 µm, respectively. Comparison is made between droplet shapes from experiment and simulation. Images in (d) show examples of the droplet equilibrium shapes under the influence of an increasing magnetic body force. The force per unit mass needed to initiate spontaneous penetration was found to be 2.7g and 3.1g computationally and experimentally, respectively (note that simulation results are only given for forces smaller than the penetration force. Images shown in (e) are for a similar experiment but with a mesh with a smaller spacing leading to computational and experimental penetration forces of 7.6g and 8.2, respectively.

Pressure inside the droplet and the droplet ACA are also given in Fig. 4.1 for the simulated droplets as they provide valuable information about how a droplet interacts with the fibers, as will be discussed later. As expected, droplet pressure increases with increasing the body force on the droplet.

4.3. Experiential Results

In this section, effects of fiber–fiber spacing, droplet volume, coating thickness (number of layers), and fiber orientation on the force needed to initiate droplet spontaneous penetration are experimentally studied.

Figure 4.2a shows the penetration of a 4 μL ferrofluid droplet into a single layer of PS parallel fibers spun for 3 minutes (see the inset figures in Fig. 4.2b). The first image from the left shows the equilibrium shape of the droplet under gravity. With increasing the magnetic force, the droplet first flattens slightly, and then starts penetrating into the space between the fibers. At a critical force of about 11.3g, the droplet spontaneously flows through the spacing between two neighboring fibers (perhaps the two with the largest spacing between them). Figure 3b shows the spontaneous penetration force for droplets of different volumes placed on single-layer coatings spun for 3 minutes (shown with red squares). This figure also shows (blue circles) how increasing the number of layers in a coating (each spun for a minute) increases the spontaneous penetration force measured for a droplet with a volume of 4 μL. It can be seen that, spontaneous penetration force increases with increasing droplet volume as the droplet will be in contact with more number of fibers. Note that the minimum force per mass needed to pull the droplet into the structure is much greater than the gravity. This force is also much bigger than the force needed to move the droplet on the surface of the coating or detach it in the vertical direction. It can also be seen in this

figure that, penetration force is much more sensitive to the number of layers of fibers in a coating than it is to the volume of the droplet (compare the red and blue symbols). It is worth mentioning that no noticeable residue was found on the fibers after droplets penetrated into the coatings (same as the case with the 3-D printed meshes).

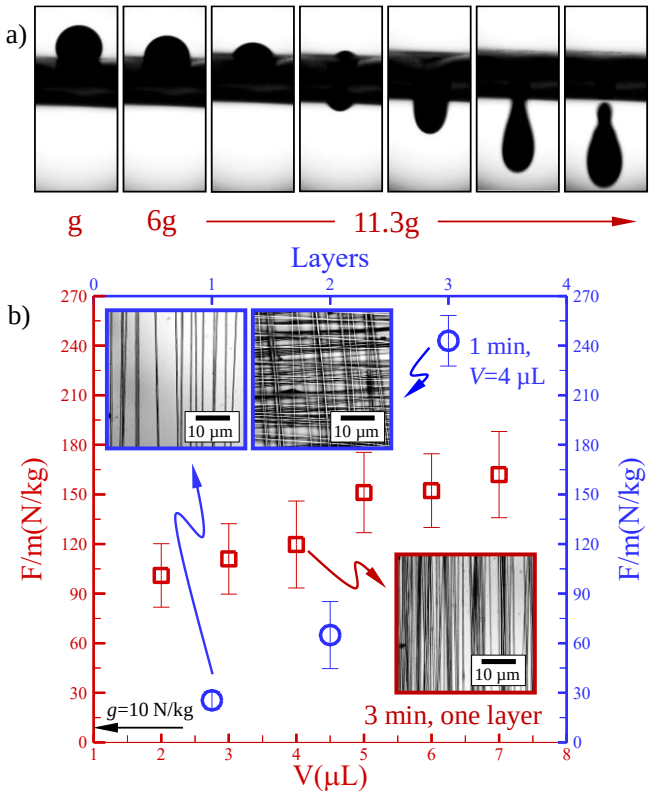

Figure 4.2: High-speed images of a ferrofluid droplet penetrating into a layer of parallel PS fibers electrospun for 3 min are shown in (a). Magnetic force increases from left to right. Droplet volume and fiber diameter are 4 μL and 0.5 μm, respectively. Effects of droplet volume and number of fiber layers on penetration force are shown in (b). The inset figures show examples of our electrospun PS coatings.

An important parameter that affects droplet penetration force in a significant way is the spacing between the fibers. As it was mentioned before, a penetrating droplet tends to find the largest opening between the fibers and flow through that "pore" as opposed to simultaneously flowing through a series of smaller pores. Spacing between the fibers in our work is varied by varying the

electrospinning time per layer (for a drum lateral velocity of 15 mm/s). Figure 4.3a shows droplet spontaneous penetration force through single- and two-layer coatings.

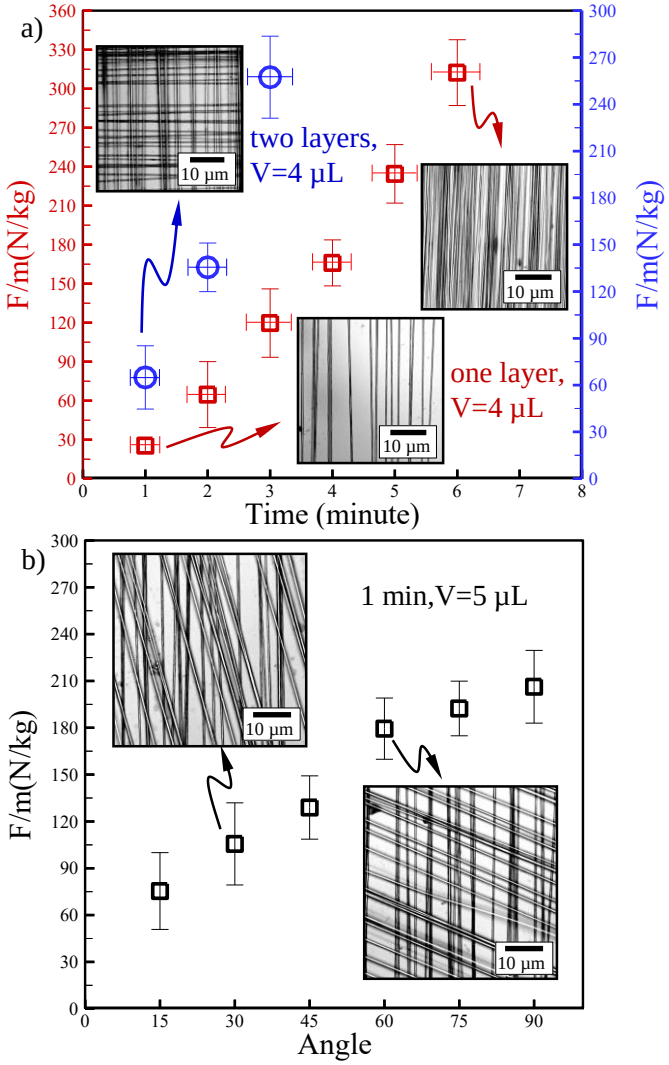

Figure 4.3: Effects of fiber spacing on the force needed to initiate droplet spontaneous penetration into one- and two-layer coatings are shown in (a). Effects of fiber orientation on the same are given in (b).

As expected, penetration force is less for coatings with larger fiber–fiber spacing (shorter spinning time). In addition to fiber spacing, spontaneous penetration force is also dependent on the orientation of the fibers with respect to each other. The error bars for spinning time in Figure 4.3a shows the statistical uncertainty of the fiber–fiber spacing, and they were calculated by counting

the fibers in each SEM image (this is quite easy as the fibers are parallel to one another) to obtain an average value and a fiber–fiber spacing standard deviation for each spinning time. To produce standard deviations in the unit of time, the standard deviations for the fiber–fiber spacing were divided by the average number of fibers per minute for each spinning time. Figure 4.3b shows the penetration force for two-layer coatings comprised of fibers with different relative angles. It can be seen that penetration force is the highest when the layers are orthogonal with respect to each other. Also note that, since the fibers are soft and flexible, it not unreasonable to assume that they may have moved in the lateral directions or deform in reaction to the forces exerted on them by the penetrating droplet.

4.4. Simulation Results

As mentioned earlier, simulating penetration of a droplet with a volume of about a few microliters into an electrospun PS coating comprised of submicron-sized fibers is computationally prohibitive. This is because such droplets are 3–4 orders of magnitude larger in diameter than the fibers, and conducting numerical simulations on such diverse length scales requires an excessive computational power. We have therefore considered a fiber diameter of 50 μm for our simulations to alleviate this problem. Figure 4.4a shows a droplet placed on a one-layer coating of fibers with a fiber spacing of 500 μm and an YLCA of 85 under gravity (shown with a blue color). The droplet is sliced from the middle to better show the penetration of the AWI between the fibers (penetration under gravity is relatively small as the YLCA is somewhat high). The AWI penetration between the fibers increases when a large body force is applied to the droplet as shown in Fig. 4.4a (shown with an orange color). Further increase in the body force for the case shown in this figure will lead to AWI burst or self-coalescence resulting in droplet spontaneous penetration into the structure. The burst and self-coalescence AWI failure mechanisms are explained graphically in Fig. 4.4b.

Consider the AWI between two parallel fibers as shown in Fig. 4.4b. Increasing the pressure over the AWI, results in the AWI penetrating deeper into the space between the fibers, as described by the so-called immersion angle.

If the pressure acting on the meniscus between two fibers is too high for the fibers' capillary forces to balance it, the meniscus continuously grows without reaching an equilibrium shape or position, and will eventually burst. This usually results in droplet spontaneous penetration into the structure unless the underlying fiber-layers are packed more densely (or if they are made of more hydrophobic materials). The highest pressure that an AWI between two parallel fibers can withstand before a burst failure takes place (also referred to as critical pressure) can be calculated using the following equation,

$$p = -\sigma \frac{2\sin(\alpha + \theta^{YL})}{s - d_f \sin\alpha} \tag{4.1}$$

where α, d_f, and s are immersion angle, fiber diameter, and fiber spacing, respectively. For such calculations, one has to first calculate $\partial p / \partial \alpha = 0$ to find the immersion angle at which the pressure is the highest (i.e., α^{burst}), and then evaluate the burst pressure for that immersion angle.

The self-coalescence mechanism is the case where two neighboring meniscus come into contact with one another underneath a fibers (or group of fibers). In this case, the fiber in contact with both meniscus will become submerged in the droplet (or "wetted" by the droplet). When a fiber is wetted, its resistance to droplet penetration becomes significantly weaker, and this can lead to droplet spontaneous penetration.

Figure 4.4c shows how droplet pressure (non-dimensionalized using droplet's Laplace pressure $p_0 = 4\sigma d_d^{-1}$, where d_d is droplet diameter) and immersion angle varying with increasing the body force on the droplet for the case of a droplet with a volume of 4 µL on a coating comprised of

parallel fibers with d_f =50 µm, s =400 µm, and θ^{YL} = 85^0. The insets in Fig. 4.4c show the AWI between the two middle fibers from when droplet is only under gravity to when it is about to spontaneously penetrate into the structure.

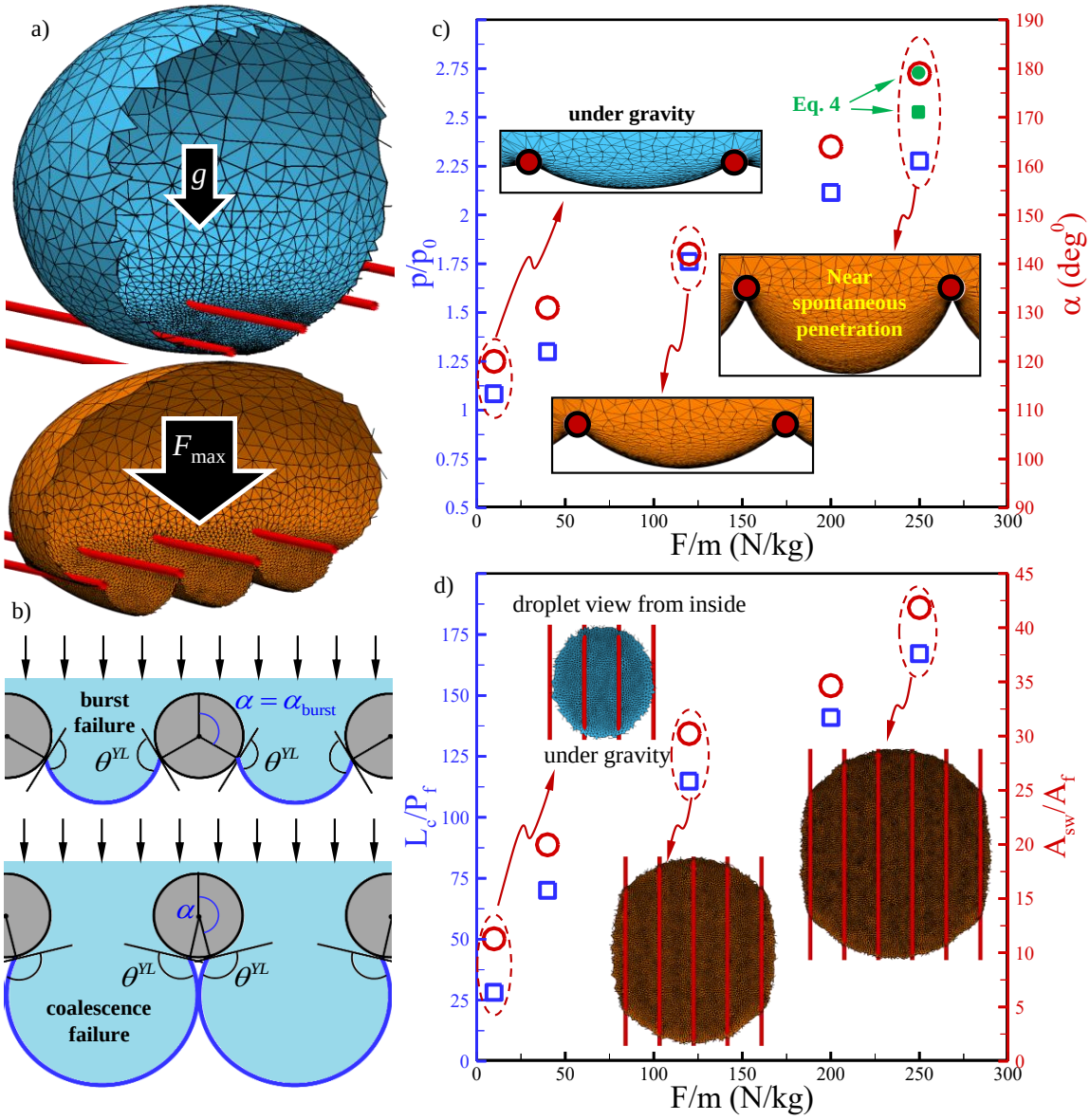

Figure 4.4: Droplet shape under gravity and at the moment of penetration are shown in (a) on a coating with a fiber dimeter of 50 µm, YLCA of 85, and a spacing of 400 µm. The burst and coalescence failures are shown schematically in (b). Simulated droplet pressure and immersion angle are presented in (c) versus external body force. Fibers WA and CL are given in (d).

Note that, droplet pressure at the moment of spontaneous penetration is more than twice higher than its equilibrium value under gravity for the droplet–coating combination considered. The burst pressure predicted using Eq. 4.1 is also shown in Fig. 4.4c with green symbols. It can be seen that the immersion angle α^{burst} and burst pressure from Eq. 4.1 are in good agreement with the results from simulations obtained for the moment of spontaneous penetration.

Increasing the body force on the droplet deforms the droplet shape and so increases the length of the droplet contact line (CL) L_c (non-dimensionalized with fiber perimeter $P_f = \pi d_f$) and the solid wetted area (WA) A_{sw} (non-dimensionalized using fiber cross-sectional area $A_f = \pi d_f^2 / 4$), as can be seen in Fig. 4.4d. The insets in Fig. 4.4d are droplet footprints viewed from inside.

To study the effects of fiber–fiber spacing on droplet penetration, we report the force needed to initiate droplet spontaneous penetration versus fiber spacing for a droplet with a volume of 4 μL placed on a one-layer coating comprised of parallel fibers with a diameter of 50 μm but different YLCAs in Fig. 4.5a. It can be seen that penetration force depends strongly on both the fiber–fiber spacing and the YLCA (the inset figures in Fig. 4.5a show the droplet profile right before spontaneous penetration). More specifically, it can be seen that penetration force and its corresponding droplet pressure monotonically increase with decreasing the spacing between the fibers or with increasing the YLCA of the fibers (more force is needed to pull a droplet into a coating comprised of hydrophobic fibers or a coating with fibers packed more closely).

Figure 4.5b shows the dimensionless CL length and solid WA for the same droplet–coating combinations reported in Fig. 4.5a. While CL length and WA clearly decrease with increasing fiber–fiber spacing, no clear trends were found in how they vary with varying fibers' YLCA. This is because when the YLCA is lower, droplet's initial (under gravity) footprint on the coating is relatively larger leading to a greater initial CL length and a larger WA.

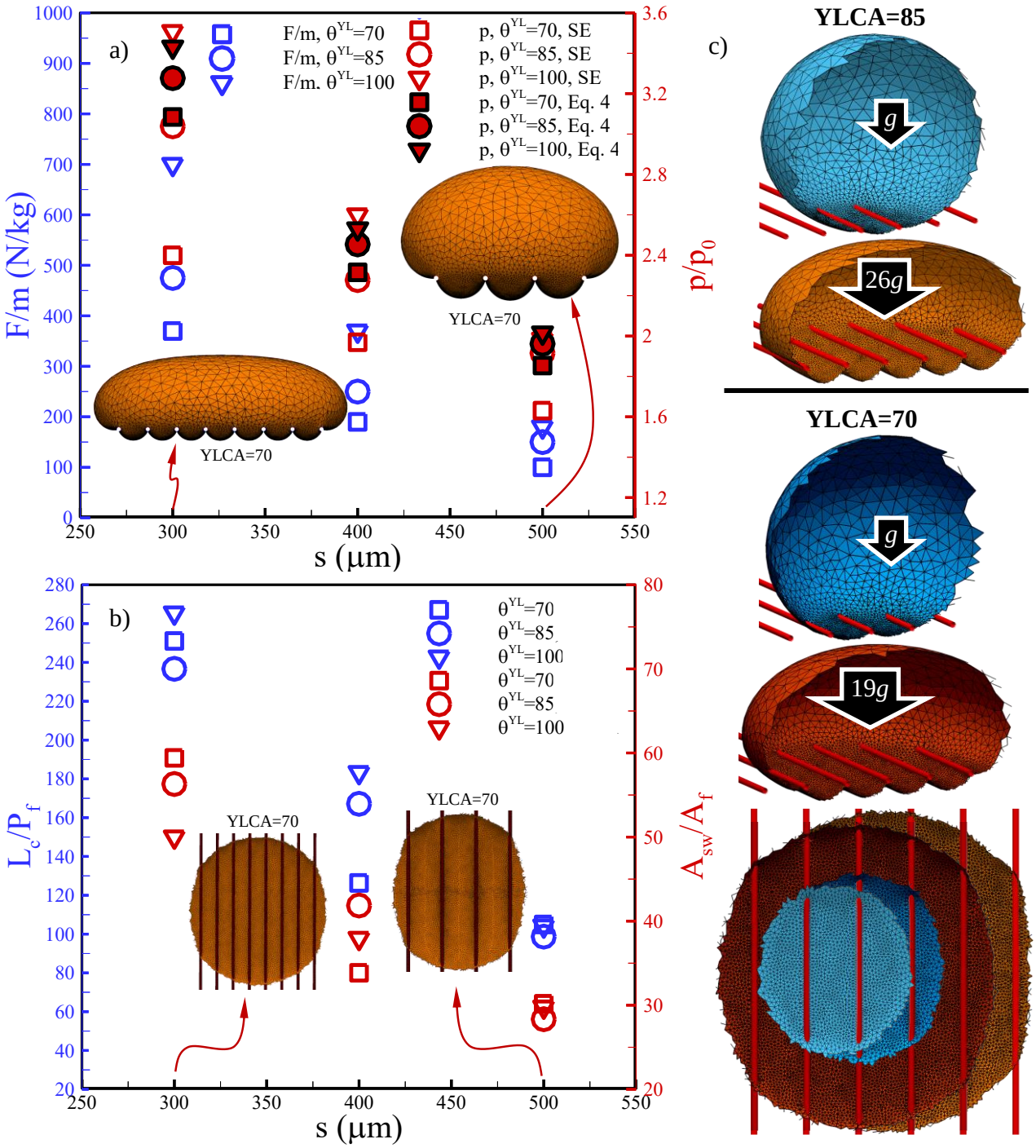

Figure 4.5: Effects of fiber spacing and YLCA on penetration force, droplet pressure, droplet CL length, and fibers WA are shown in (a) and (b). Figure (c) compares droplet profiles under gravity and at the moment of penetration on a layer of parallel fibers with identical spacing but different YLCAs or 85 and 70 degrees. Figure (c) also compared droplet footprints of these coatings under the gravity and at the penetration moment. The figures are color-coded for better illustration.

When the YLCA is higher, the droplet's initial footprint is smaller, but it grows to a larger size (the droplet severely deforms and spreads over the surface) before the external body force becomes strong enough to pull the droplet in (a higher internal pressure is needed for the meniscus between two neighboring fibers to fail when the YLCA is higher). This leads to larger CL lengths and WAs for droplets on coatings with higher YLCAs. This is also shown in Fig. 4.5c using simulated droplet footprints overlaid on top of each other for comparison.

To quantify how the spontaneous penetration force increases with increasing the number of fiber layers, we considered a water droplet with a volume of 4 μL on two-layer (orthogonally-layered) coatings of different fiber–fiber spacing but only one YLCA of 85 degrees in Fig. 4.6 (effects of YLCA is similar to those discussed in Fig. 4.5). As expected, penetration force and its corresponding droplet pressure decrease with increasing the spacing between the fibers. The results obtained previously for a one-layer coating with s=500μm are added to this figure for comparison. It can be seen that adding the second layer of fibers increased the penetration force by a factor of about 2.5. Obviously, applying such a strong body force to a droplet results in a significant droplet flattening over the surface (see the initial and final footprints of the droplet on an orthogonal coating with a fiber–fiber spacing of 500 μm in Fig. 4.6b). Such a significant droplet spreading brings about significant increase in the CL of the droplet and the fibers WA (Fig. 4.6c) relative to those obtained for the penetration of the same droplet through one-layer coatings.

Neglecting the variation of the immersion angle along the length of the fibers, an approximate equation for the burst pressure for an AWI over the unit cell of a two-layer structure was produced in a previous work using the balance of forces (see Fig. 4.6d). Describing the vertical component of the pressure force on the AWI as $p(s-d_f \sin\alpha_1)(s-d_f \sin\alpha_2)$, the capillary forces along the CL

on the top fibers as $2\sigma\sin(\theta^{YL}+\alpha_1)(s-d_f\sin\alpha_2)$, and capillary forces along the CL on the bottom fibers as $2\sigma\sin(\theta^{YL}+\alpha_2)(s-d_f\sin\alpha_1-d_f)$, one can obtain,

$$p=-2\sigma\frac{\sin(\alpha_1+\theta^{YL})(s-d_f\sin\alpha_2)+\sin(\alpha_2+\theta^{YL})(s-d_f\sin\alpha_1-d_f)}{(s-d_f\sin\alpha_1)(s-d_f\sin\alpha_2)} \tag{4.2}$$

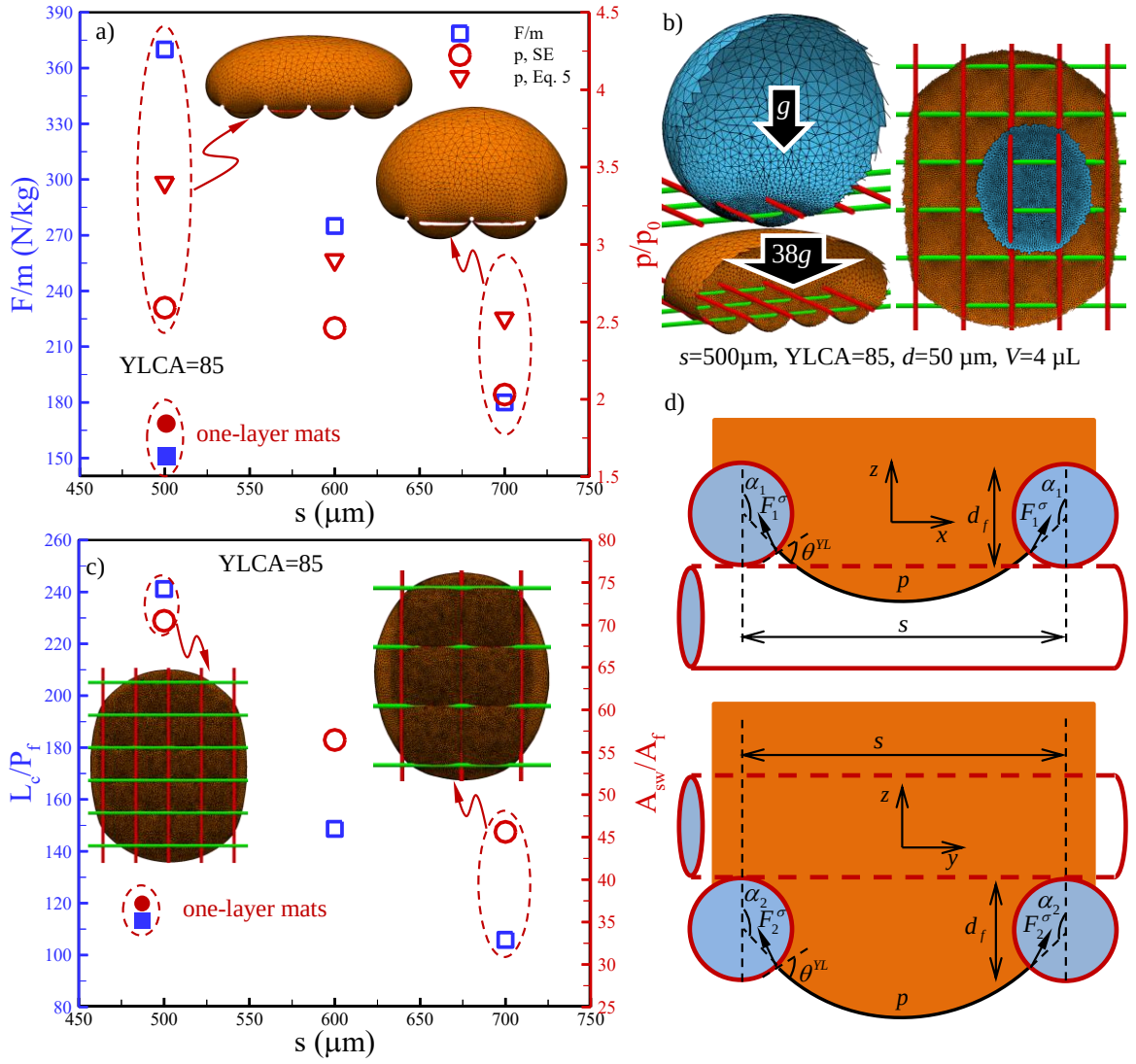

Figure 4.6: Effects of fiber spacing and YLCA on spontaneous penetration force, droplet pressure, droplet CL length, and fibers WA are shown in (a) and (c) for two-layer coatings comprised of orthogonal fibers. Examples of droplet profiles and footprints under the influence of gravity and at the moment of spontaneous penetration are given in (b). A schematic diagram for the AWI over a square unit cell of a two-layer structure consisting of four fibers is given in (d).

Obviously, the length of the CL on the fibers in the lower layer is shorter than that of the fibers in the upper layer. To incorporate this into our pressure equation, we subtracted a length equal to a fiber diameter from the length of the lower fibers' CL in each unit cell (the $-d_f$ term in the last parenthetical term in the numerator of the RHS of Eq. 4.2). The burst pressure can again be obtained by finding the immersion angles at which the pressure is the highest (i.e., solving $\partial p / \partial \alpha_1 = 0$ and $\partial p / \partial \alpha_2 = 0$ simultaneous for α_1^{burst} and α_2^{burst}). Figure 4.6a compares the predictions of Eq. 4.2 with those obtained from SE simulations at the moment of spontaneous penetration for different fiber–fiber spacing. The agreement between SE predictions and those of Eq. 4.2 is quite good given the number of simplifying assumptions considered to make such a purely analytical calculation possible.

4.5. Force Balance Analysis

Consider a droplet placed on a layer of parallel fibers aligned in the *y*-direction at the moment of spontaneous penetration. The forces acting on the fibers in the *z*-direction can be broken down into the capillary forces (acting along the CL) and the pressure forces (acting on the WA), i.e.,

$$F_z = F^{\sigma} + F^{p} = \int_{CL} \sigma \sin\beta dl + \int_{WA} p dA \tag{4.3}$$

where β is the angle between the tangent to the AWI and a horizontal plane along the CL on the fiber (see Fig. 4.7a). In this equation, dl and dA are the CL and the WA, respectively. Using Eq. 4.3 to obtain the force needed to initiate droplet spontaneous penetration into a fibrous coating requires the local slope of the AWI along the CL on each fiber as well as the WA of each fiber. Unfortunately, such fiber-level detailed information can only be obtained from a numerical simulation. In this concern, we have considered a series of simplifying approximations to make it possible to use Eq. 4.3 when such detailed information is not available, as described below. As

WA and CL are different on the fibers in the first and second layer, we describe each case separately.

One of the most important parameters needed for predicting the local slope of the AWI along the fibers is the immersion angle (characterizing the local depth of the AWI). Consider the droplet shown in Fig. 4.7a, a droplet with a volume of 4 µL on a coating comprised of parallel fibers with a diameter of 50 µm with a fiber–fiber spacing of 500 µm, and an YLCA of 85 degrees. Figure 4.7b reports the immersion angles along the length of the four fibers in contact with the droplet (the contact angle on the left and right sides of the fibers are shown with different symbols). It can be seen that immersion angle on a wetted fiber only changes near the edges of the fiber WA. For instance, immersion angle is greater than about 160 degrees for most of the wetted length of the fibers, except for the left side of the left fiber and right side of the right fiber (i.e., fibers near the left and right edges of the droplet, numbered fibers 1 and 4, respectively, in Fig. 4.7a). Therefore, an average immersion angle $\alpha_{avg} = \int_{CL} \alpha dl$, could be defined and used in this analysis to simplify the problem at hand. Denoting the droplet maximum body and footprint lengths in the direction of the fibers (in the y-direction here) with $L_y^{\max}$ and L_y^{fp}, respectively, we noticed from the simulations that the ratio of the length of the CL on a fiber having an immersion angle of $\alpha \cong \alpha^{\max}$ to the total length of the CL on that fiber (i.e., $L_y^{\alpha\max} / L_y^{fp}$) is somewhat proportional to $L_y^{\mathrm{fp}} / L_y^{\max} \approx 0.8$ for fibers far from the edge of droplet footprint. This proportionality $L_y^{\alpha\max} / L_y^{fp} \propto L_y^{fp} / L_y^{\max}$ depends of course on the shape of the droplet on the surface and so it may vary depending on fibers' YLCA and spacing (see Fig. 4.7a). We use this ratio here to scale down the maximum immersion angle and use it as an approximation for the average immersion angle of the fibers, i.e., $\alpha_{avg}^{aprx} = \alpha^{\max}(L_y^{\alpha\max} / L_y^{\mathrm{fp}})$. To estimate the maximum immersion angle, we assumed the AWI failure

to be the burst mechanism and so assumed $\alpha^{\max} \cong \alpha^{\text{burst}}$ by calculating $\partial p / \partial \alpha = 0$ from Eq. 4.1 (i.e., we assumed the droplet pressure at the moment of penetration to be the burst pressure). This allowed us to calculate an average (approximate) angle for the capillary force on the fiber with the horizon to be later used in Eq. 4.3, i.e.,

$$\beta_{avg}^{aprx} = \theta^{YL} + \alpha_{avg}^{aprx} - \pi \tag{4.4}$$

The next geometrical parameters to approximate are the length of the CL and the WA of each fiber. Considering an elliptical cross-section for the droplet footprint on the surface (Fig. 4.7a), one can write,

$$(\frac{2x}{L_x^{fp}})^2 + (\frac{2y}{L_y^{fp}})^2 = 1 \tag{4.5}$$

To obtain an overall WA A^{aprx} and CL length C^{aprx} for all the fibers in contact with the droplet, we can now consider

$$A^{aprx} = 2d_f \sum_{i=1}^{N_x^f} y_i \tag{4.6}$$

$$C^{aprx} = 4\sum_{i=1}^{N_x^f} y_i \tag{4.7}$$

With the number of fibers in contact with the droplet in the fibers given as,

$$N_x^f = L_x^{fp} / s + 1 \tag{4.8}$$

and

$$y_i = \frac{L_y^{fp}}{2}\sqrt{1-(\frac{2x_i}{L_x^{fp}})^2} \tag{4.9}$$

and

$$x_i = (i-1)s + (L_x^{fp} - (N_x^f - 1)s)/2 \tag{4.10}$$

An approximate form of Eq. 4.3 can now be written as,

$$F_z = C^{aprx}\sigma \sin\beta_{avg}^{aprx} + p_{burst}^{2D} A^{aprx} \tag{4.11}$$

where A^{aprx}, C^{aprx}, β_{avg}^{aprx}, and p_{burst}^{2D} can be obtained from Eq. 4.6, Eq. 4.7, Eq. 4.4, and Eq. 4.1, respectively. Good agreement can be seen in Fig. 4.7d between the predictions of Eq. 4.11 and those from SE simulations for the force needed to initiate droplet spontaneous penetration in one-layer coatings and those using fiber-level information from Eq. 4.3.

For the case of two-layer coatings, the WA and CL for the top layer can be obtained using Eqs. 4.6 through 4.10, the same exact way as it was done for a droplet on a one-layer coating. The WA for the second layer can be added to that of the first layer, as the fibers in both layers are exposed to the same pressure, i.e.,

$$A^{aprx} = 2d_f(\sum_{i=1}^{N_x^f} y_i + \sum_{i=1}^{N_y^f} x_i) - 2N_x^f N_y^f d_f^2 \tag{4.12}$$

with the number of fibers in contact with the droplet in the second layer given as

$$N_y^f = L_y^{fp}/s + 1 \tag{4.13}$$

where

$$x_i = \frac{L_x^{fp}}{2}\sqrt{1-(\frac{2y_i}{L_y^{fp}})^2} \tag{4.14}$$

and

$$y_i = (i-1)s + (L_y^{fp} - (N_y^f - 1)s)/2 \tag{4.15}$$

Following the same logic discussed earlier in deriving Eq. 4.2, we have reduced the length of CL on the fibers in the second layer by a length equal to a fiber diameter in each unit cell. This will also reduce the WA of these fibers in each unit cell by a factor of $2d_f^2$ or $2N_x^f N_y^f d_f^2$ over the entire droplet footprint (see Eq. 4.12 and the black square in the magnified image in Fig. 4.7c).

In calculating the total capillary force for the two-layer coatings, the CL for the fibers in the first layer and that for the fibers in the second layer should be multiplied to their corresponding capillary force, i.e., $\sigma\sin(\theta^{YL}+\alpha_{avg}^{aprx,1})4\sum_{i=1}^{N_x^f} y_i$ for the first layer and $\sigma\sin(\theta^{YL}+\alpha_{avg}^{aprx,2})(4\sum_{i=1}^{N_y^f} x_i - 2N_x^f N_y^f d_f)$ for the second layer. Note that we have considered a similar approximation for the average immersion angle in the second layer, $\alpha_{avg}^{aprx,2}=\alpha^{\max}(L_x^{\alpha\max}/L_x^{\mathrm{fp}})$. Also note that with the assumption of $\alpha^{\max}\cong\alpha^{\mathrm{burst}}$, one should obtain α^{burst} from Eq. 4.2 as explained earlier in Section IIIB.

Equation 14 can now be rewritten as,

$$F_z = -4\sum_{i=1}^{N_x^f} y_i\,\sigma\sin(\theta^{YL}+\alpha_{avg}^{aprx,1}) - (4\sum_{i=1}^{N_y^f} x_i - 2N_x^f N_y^f d_f)\sigma\sin(\theta^{YL}+\alpha_{avg}^{aprx,2}) + p_{burst}^{2D}(2d_f(\sum_{i=1}^{N_x^f} y_i + \sum_{i=1}^{N_y^f} x_i) - 2N_x^f N_y^f d_f^2) \quad (4.16)$$

where p_{burst}^{2D} should be obtained from Eq. 4.2.

Good agreement can be seen in Fig. 4.7d between the predictions of Eq. 4.16 and those from SE simulations for the force needed to initiate droplet spontaneous penetration in two-layer coatings and those using fiber-level information from Eq. 4.3. See our published paper for more details on this chapter [92].

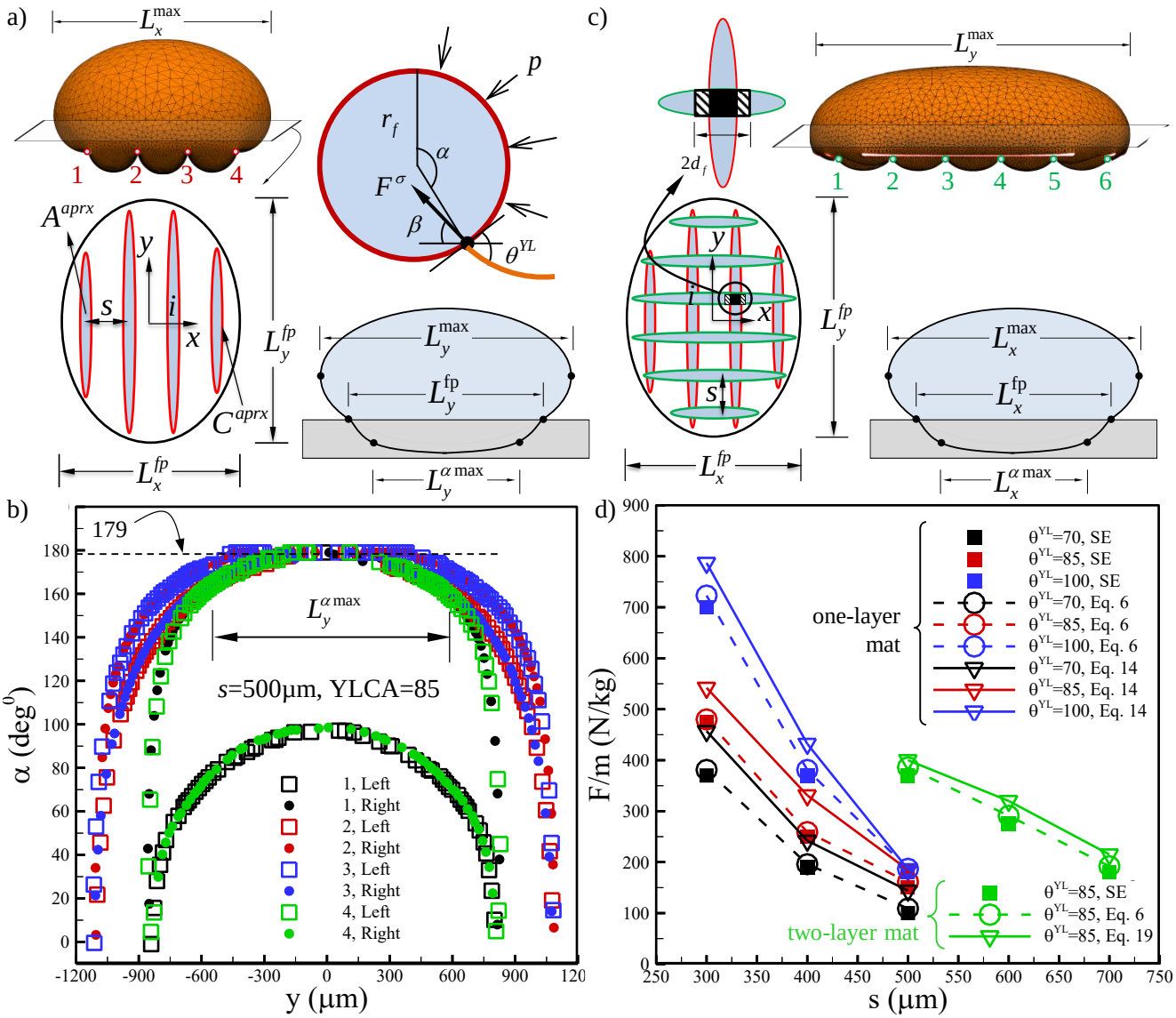

Figure 4.7: Droplet shape from the transverse (schematic) and longitudinal (simulations) views are given in (a) on a one-layer coating with a fiber dimeter of 50 μm, a spacing of 500 μm, and a YLCA of 85 deg. A free body diagram for the forces acting on one side of a fiber as well as a schematic drawing for droplet footprint are also given in (a). Figure (b) reports the immersion angles along the length of each of the four fibers in contact with the droplet shown in (a). Figure (c) presents the same information as was given in (a) but for when the droplet is placed on a two-layer coating. Figure (d) compares prediction of our approximate equations (Eqs. 4.11 and 4.16) with those of SE simulations. Predictions of Eq. 4.3 (requiring fiber-level information from simulations) are also added for completeness of the study.

4.6. Conclusions

Droplet penetration into idealized non-wetting fibrous coatings was studied computationally and experimentally in this chapter. As the earth gravity was not enough to initiate water droplet penetration into our hydrophobic fibrous coatings (electrospun polystyrene), we used aqueous ferrofluid droplets for our experiment so that the body force on the droplets could be enhanced using a magnet, and droplet penetration could be induced. It was found that the force needed to initiate droplet penetration varies with varying droplet volume or the geometrical properties of the fibrous coatings. Our experiments also revealed that increasing the relative angle between the fibers, in the range of angles from zero (parallel fibers) to ninety degrees (orthogonal fibers), increases the resistance of the material to droplet penetration. We also conducted a series of numerical simulations to provide additional insight into the physics of the problem and to develop an in-depth analysis of the forces acting on a droplet penetrating into a fibrous material. The accuracy of our simulations were verified through one-on-one comparison with experimental data obtained for droplet penetration into 3-D printed mesh-like structures. The simulations allowed us to isolate individual factors affecting droplet penetration (e.g., capillary forces acting on droplet¬–fiber CL or pressure forces acting on fibers WA) and quantify their contribution. Novel easy-to-use analytical expressions are derived for droplet penetration force to circumvent the need for running CPU-intensive simulations for each and every droplet–coating combinations of interest, and thereby expand the application of the reported experimental/computational results.

Chapter 5. Universal Equation for Droplet Adhesion and Mobility

5.1 Introduction

One way to design the desired surface for a specific application is using available and reliable experimental or computer simulation data that have been obtained by others. However, all empirical correlations are limited to a specific applications and limited range of data. A better alternative way is developed a universal correlation that one can use for a wide range of data and a variety of other applications. In a simple word, the goal is to developed an equation that one can simply plug in geometrical parameters of a fibrous surface such as fiber spacing, fiber diameter or Young Laplace Contact Angle (YLCA) and obtained the droplet detachment force without performing any experiment or computer simulations.

5.2. Method

A droplet deposited on a surface may not necessarily roll off by only tilting the surface, even when the surface is hydrophobic (when the droplet maintains a large apparent contact angle on the surface). In such a condition, a force greater than droplet's weight is needed to detach the droplet from the surface (or to make it move on the surface). Equation 2.11 to estimate the vertical force needed to detach a droplet from a hydrophobic surface comprised of a layer of parallel fibers was developed in the first task which needs two parameters of droplet diameter near the surface d_{Cir}^{Cr} and droplet's apparent contact angle at the moment of detachment θ_{App}^{Cr}. While this equation is easy to use and provides reasonable estimation for droplet detachment force, it unfortunately requires quantitative information about droplet shape at the moment of detachment. Similarly, for droplet motion on a surface, Equation 1.3 can be used. This equation requires a characteristic

length to describe the size of the droplet. While no universal dimension has yet been determined for this equation, one can logically expect droplet width (i.e., largest dimension perpendicular to droplet's direction of motion) at the critical moment (i.e., when the in-plane body force exerted on the droplet is large enough to initiate droplet motion) to be the proper dimension for this equation, based on the balance of forces on the droplet. Given the difficulties involved in knowing droplet width at the critical moment without conducting an experiment or a numerical simulation (which otherwise would negate the whole point of using an equation for force prediction), different arbitrary dimensions have been used in the literature. It has also become customary to include an empirical correction factor (also known as "shape factor") k to make up for the mismatch predictions of Eq. 1.3 and experimental or computational data.

As was earlier, the main purpose of the current chapter is to develop an easy-to-use equation for predicting the force needed to vertically detach (or horizontally move) a droplet from (or on) an idealized fibrous surface without needing to conduct an experiment or a numerical simulation. To do so, our approach is to relate the droplet shape at the moment of detachment to its shape when it is only under gravity (no other external forces involved), and thereby estimated the required parameters in Eqs. 1.3 and 2.11 (i.e., $d_{Cir}^{Cr}, \theta_{App}^{Cr}, \theta_{Rec}, \theta_{Adv}, w^{Cr}$). In fact, one can calculate d_{Cir}^{Gr} and θ_{App}^{Gr} when a droplet is under gravity using the Cassie–Baxter (CB) equation modified for surfaces comprised of parallel fibers (Eq. 1.1).

5.3. Results and Discussion

In this section, we present our numerical simulation results obtained for the effects of geometrical and wetting properties of a coating comprised of a layer of parallel fibers (fiber dimeter, fiber–fiber spacing, and YLCA) on droplet mobility. Figures 5.1a–5.1b show the out-of-plane and in-

plane forces needed to detach or move a droplet on the aforementioned surface as a function of fiber–fiber spacing and YLCA, when the fiber diameter and the droplet volume are kept constant.

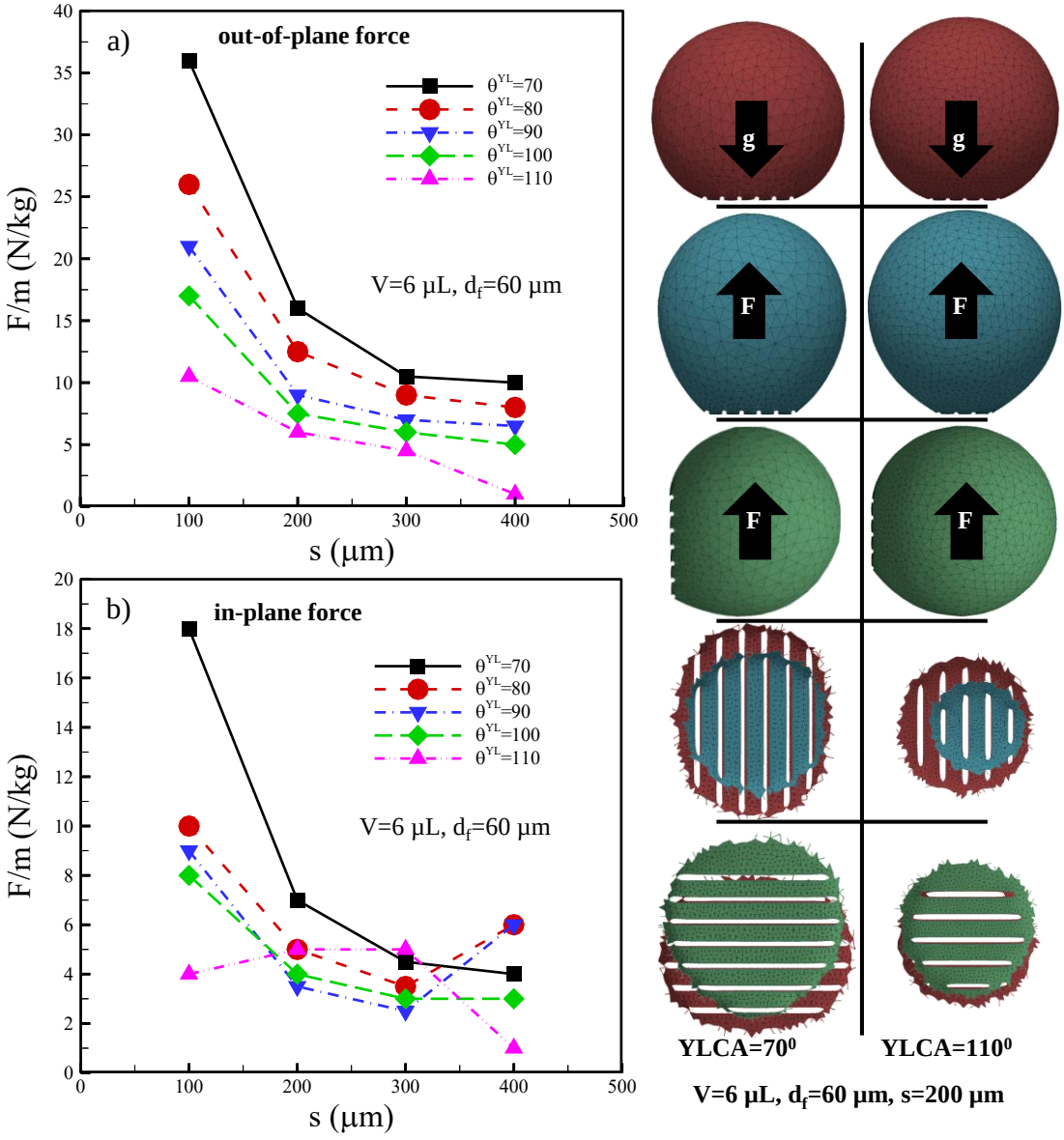

Figure 5.1: Effects of fiber spacing and YLCA on droplet detachment force per mass (F/m) in the out-of-plane and in-plane directions are given in (a) and (b), respectively. Fiber diameter and droplet volume were kept constant at 60 µm and 6 µL, respectively. Examples of simulated droplet profiles and footprints on the coatings are also given to provide additional insight into droplet shape change under gravitational (downward), external out-of-plane (upward), and external in-plane forces (upward) forces. Droplet footprints are color-coded to match their corresponding droplet profiles.

The force values reported are obtained from SE simulations. The variables *F*, *m* and *s* denote force, droplet mass and fiber-fiber spacing. Examples of droplet shape simulations are given in this figure with colors red, blueish green, and green for droplet under the gravity, influenced by an out-of-plane body force, and when pulled by an in-plane force, respectively. As expected, it is generally easier to move (or detach) a droplet placed on a coating with a higher YLCA (droplet is in contact with a smaller number of fibers). The same also explains why detachment force is smaller when the fiber–fiber spacing is larger.

Figures 5.2a–5.2b show the effects of fiber diameter on out-of-plane and in-plane detachment forces when droplet volume and YLCA are constant. These results indicate that detachment force in both the out-of-plane and in-plane directions are higher on coatings with larger fiber diameters. This is because droplet contact length and fibers' wetted area are larger for coatings made up of larger fibers (capillary force holding the droplet is higher), as shown with droplet footprint examples in Figure 5.2. Figures 5.3a–5.3b show droplet out-of-plane and in-plane detachment force vs. fiber–fiber spacing for droplets of different volumes (note that force is presented per unit of droplet mass). It can be seen that droplets with a smaller volume require a larger force per mass to become detached or mobilized. It should be noted that a droplet may retain more than one equilibrium shape on a rough surface, depending on how it was deposited on the surface and the local morphology of the surface underneath the droplet (see e.g., [38, 45, 93]). To investigate whether or not the detachment forces obtained from our simulations were dependent on the starting shape or position of the droplets, we considered four different arbitrary initial shape-position combinations (denoted as case A through case D) for one of the systems discussed in Figure 5.2 (a droplet with a volume of 6 µL on a coating with d_f=20 µm, spacing=300 µm, and a YLCA=85^0).

We monitored how the shapes of these droplets evolved to an equilibrium shape under gravity and also under an external body force until they detached from the surface.

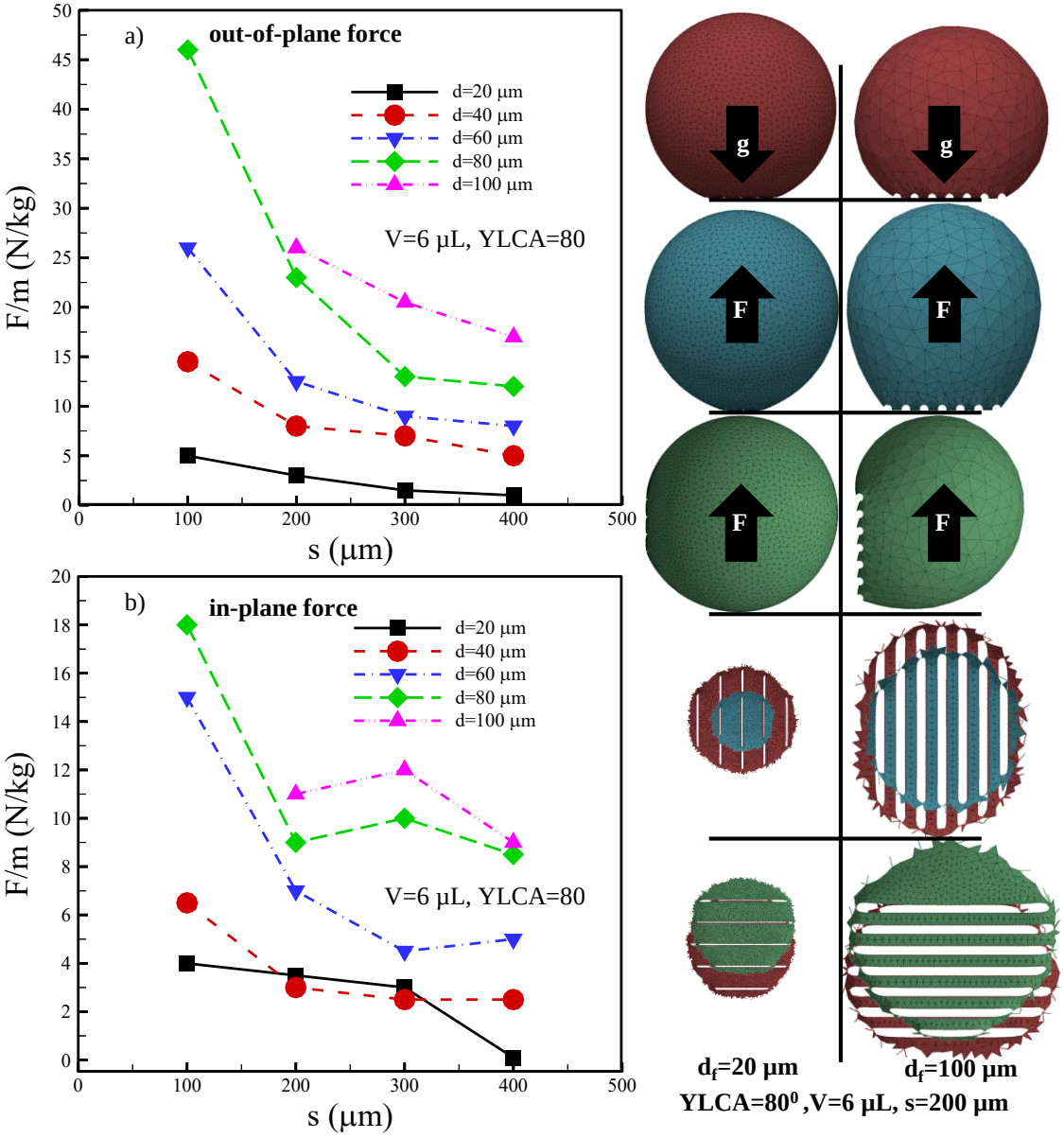

Figure 5.2: Effects of fiber spacing and fiber diameter on droplet detachment force per mass (F/m) in the out-of-plane and in-plane directions are given in (a) and (b), respectively. YLCA and droplet volume were kept constant at 80 degrees and 6 µL, respectively. Examples of simulated droplet profiles and footprints on the coatings are also given to provide additional insight into droplet shape change under gravitational (downward), external out-of-plane (upward), and external in-plane forces (upward) forces. Droplet footprints are color-coded to match their corresponding droplet profiles.

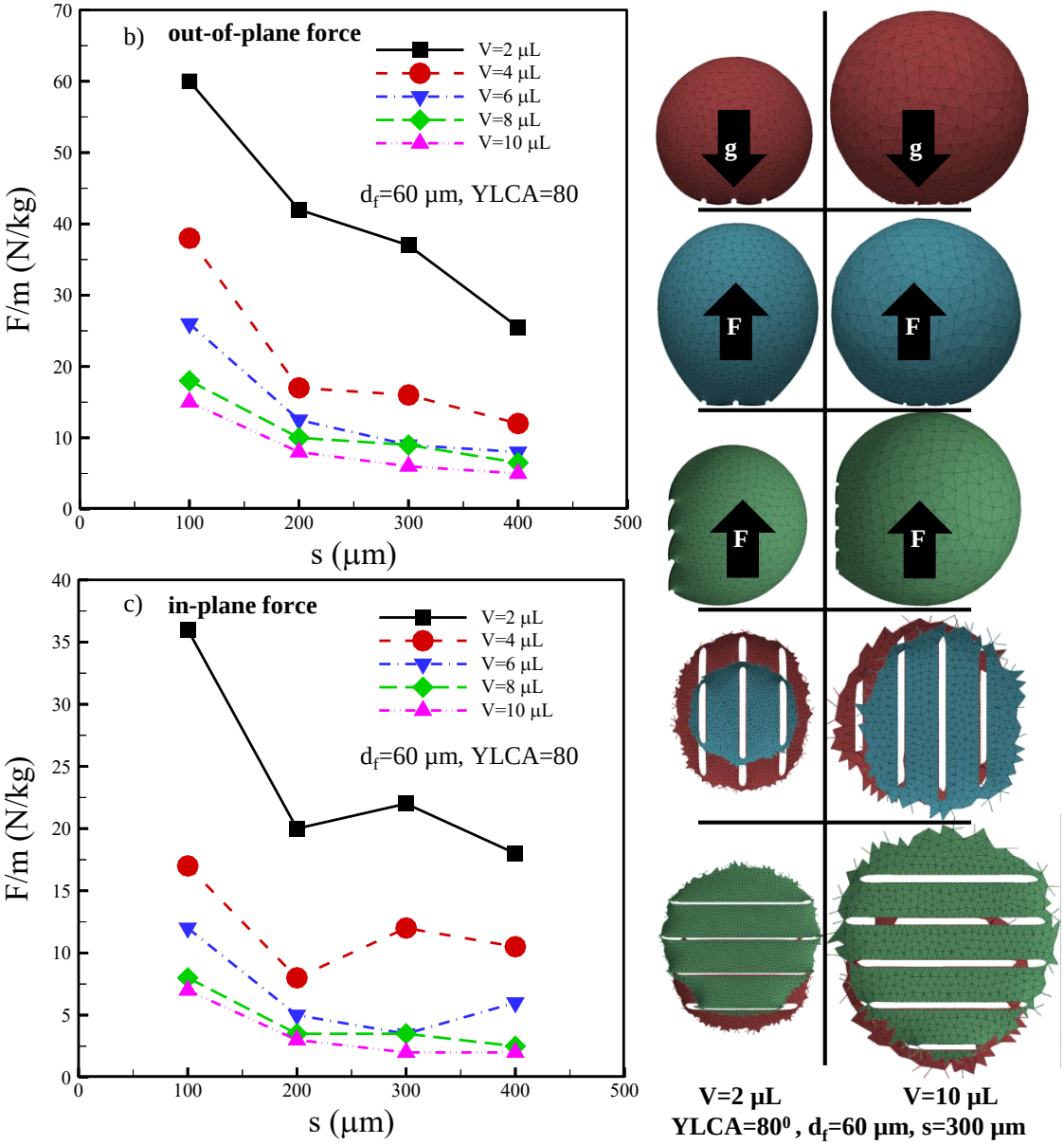

Figure 5.3: Effects of fiber spacing and droplet volume on droplet detachment force per mass (F/m) in the out-of-plane and in-plane directions are given in (a) and (b), respectively. YLCA and fiber diameter were kept constant at 80 degrees and 60 µm, respectively. Examples of simulated droplet profiles and footprints on the coatings are also given to provide additional insight into droplet shape change under gravitational (downward), external out-of-plane (upward), and external in-plane forces (upward) forces. Droplet footprints are color-coded to match their corresponding droplet profiles.

As can be seen in Figure 5.4, different equilibrium shapes could be observed for some cases under the gravity (e.g., case D vs. case C), but the droplet profiles prior to detachment (droplets' final equilibrium state) as well as the in-plane or out-of-plane forces obtained from the simulations were

all identical and unaffected by the choice of initial droplet shape-position combination (consistent with our previous study on droplet detachment from rough fibers by Amrei et al. [45]).

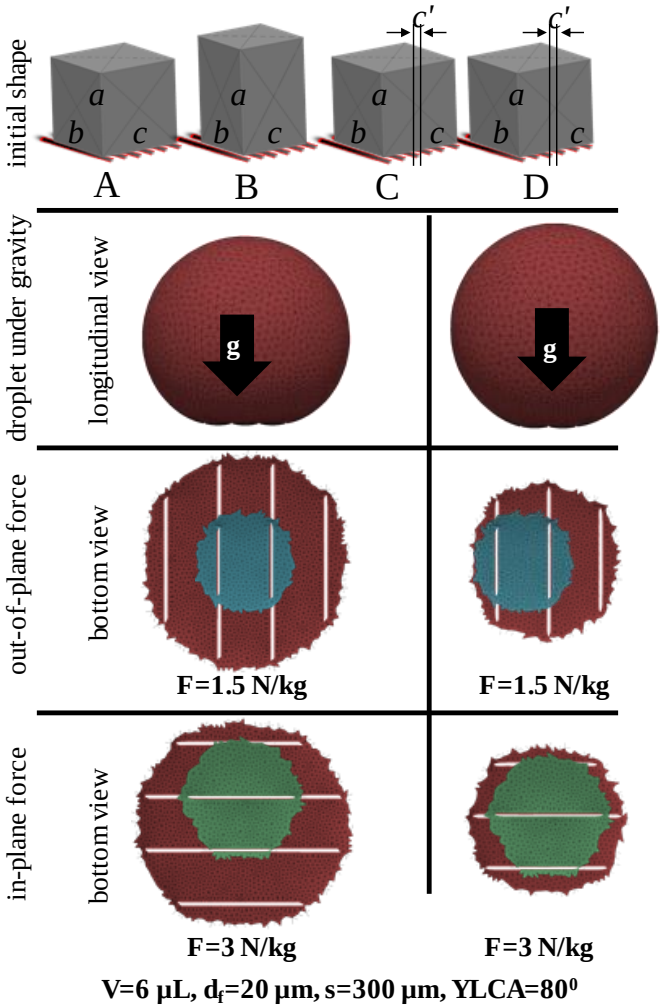

Figure 5.4: Different arbitrary starting shapes (grey cubes denoted by A, B, C, and D) with a volume of 6 µL are considered in our SE simulations to study their possible impact on droplet detachment force prediction. For case A, the dimensions a, b, and c are equal to 1817 µm and the cube is centered with one of the underlying fibers. For case B, the dimensions a, b, and c are changed to 2263, 1592 and 1592 µm, respectively. For cases C and D, dimensions are the same as case A but the cubes are off-centered by c'=100 and c'=150 µm, respectively. Colors red, blue and green represent droplet under the gravity, droplet under a vertical detachment force and droplet under a horizontal detachment force, respectively.

Figures 5.5a–5.5b compare θ_{App}^{Gr} and d_{Cir}^{Gr} (droplet apparent contact angle and diameter near the surface when droplet is only under gravity) from simulation with those obtained from the CB

equation for three examples of droplet–coating combinations. For the clarity of illustrations, the data are divided into three categories of $70 < \theta^{YL} < 110, 20 < d_f < 100\ \mu m$ and $2 < V_a < 10\ \mu L$. The differences between the predictions of SE simulations and those of CB equation (presented in the form of absolute error percentage $e_d = |\frac{d^{Gr}_{Cir,SE} - d^{Gr}_{Cir,CB}}{d^{Gr}_{Cir,SE}}|$ and $e_\theta = |\frac{\theta^{Gr}_{Cir,SE} - \theta^{Gr}_{Cir,CB}}{\theta^{Gr}_{Cir,SE}}|$ for the eighty-five simulations reported in Figures 5.1–5.3). Despite some differences between the predictions of SE simulations and those of the CB equation, the CB equation is still used in the current study for its simplicity as we move on to further analyze the results reported in Figures 5.1–5.3. Our objective here is to develop useful relationships between a droplet's geometric properties under the gravity (i.e., $\theta^{Gr}_{App}$and d^{Gr}_{Cir}) and those at the moment of out-of-plane (i.e., $\theta^{Cr}_{App}$and d^{Cr}_{Cir}) or in-plane (i.e., θ^{Gr}_{App}, $w^{Gr}$and θ_{Adv}, θ_{Rec} , w^{Cr}) detachment. Such relationships can then be used in Eqs. 1.3 and 2.11 for force prediction.

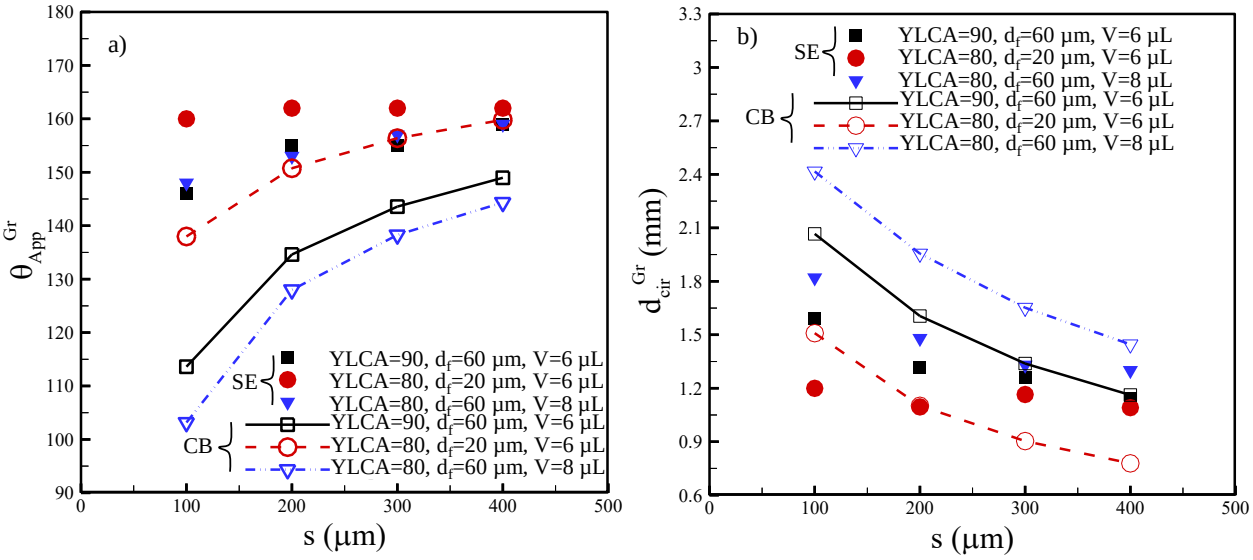

Figure 5.5: Examples of droplet diameter and apparent contact angle obtained from our numerical simulations and from the Cassie–Baxter equation are given in (a) and (b), respectively. θ^{Gr}_{App} and d^{Gr}_{Cir} are apparent contact angle and droplet diameter near the surface when the droplet is only under the gravity, respectively.

Figure 5.6a shows the ratio of a droplet's circular diameter under gravity to that at the moment of out-of-plane detachment $d_{cir}^{Cr}/d_{Cir}^{Gr}$ (ratio of droplet diameter near the surface at the moment of detachment to that when the droplet is only under the gravity) versus fiber–fiber spacing for eighty-five droplet–surface combinations. In the absence of an expected trend for how $d_{cir}^{Cr}/d_{Cir}^{Gr}$ should vary with fiber–fiber spacing, we considered here a linear relationship for its simplicity, i.e.,

$$\frac{d_{Cir}^{Cr}}{d_{Cir}^{Gr}} = \vartheta_1 s + \vartheta_2 \tag{5.1}$$

where ϑ_1 and ϑ_2 are 462 m^{-1} and 0.9163, respectively. A similar linear trend is also considered for the difference between droplet apparent contact angle under the gravity and that at the moment of out-of-plane detachment in Figure 5.6b, i.e.,

$$\theta_{App}^{Gr} - \theta_{App}^{Cr} = \beta_1 s + \beta_2 \tag{5.2}$$

where β_1 and β_2 are -39167 m^{-1} and 24, respectively. For the case of droplet in-plane detachment, the ratio of droplet's width under the gravity to that at the moment of in-plane motion on the surface $\frac{w^{Cr}}{w^{Gr}}$ (ratio of droplet width at the moment of detachment to that when the droplet is only under the gravity) is considered versus fiber–fiber spacing for the all eighty-five cases (see Figure 5.6c) to produce a linear fit as,

$$\frac{w^{Cr}}{w^{Gr}} = \gamma_1 s + \gamma_2 \tag{5.3}$$

where γ_1 and γ_2 are 584.27 m^{-1} and 0.7824, respectively. Likewise, we considered the difference between the advancing (and receding) contact angle and that under gravity (see Figure 5.6d) to obtain the following equations.

$$\theta_{Adv} - \theta_{App}^{Gr} = \delta_1 s + \delta_2 \tag{5.4}$$

$$\theta_{App}^{Gr} - \theta_{Rec} = \varepsilon_1 s + \varepsilon_2 \tag{5.5}$$

where δ_1, δ_2, ε_1 and ε_2 are -20943 m^{-1}, 7.781, -52105 m^{-1}, and 37.22, respectively.

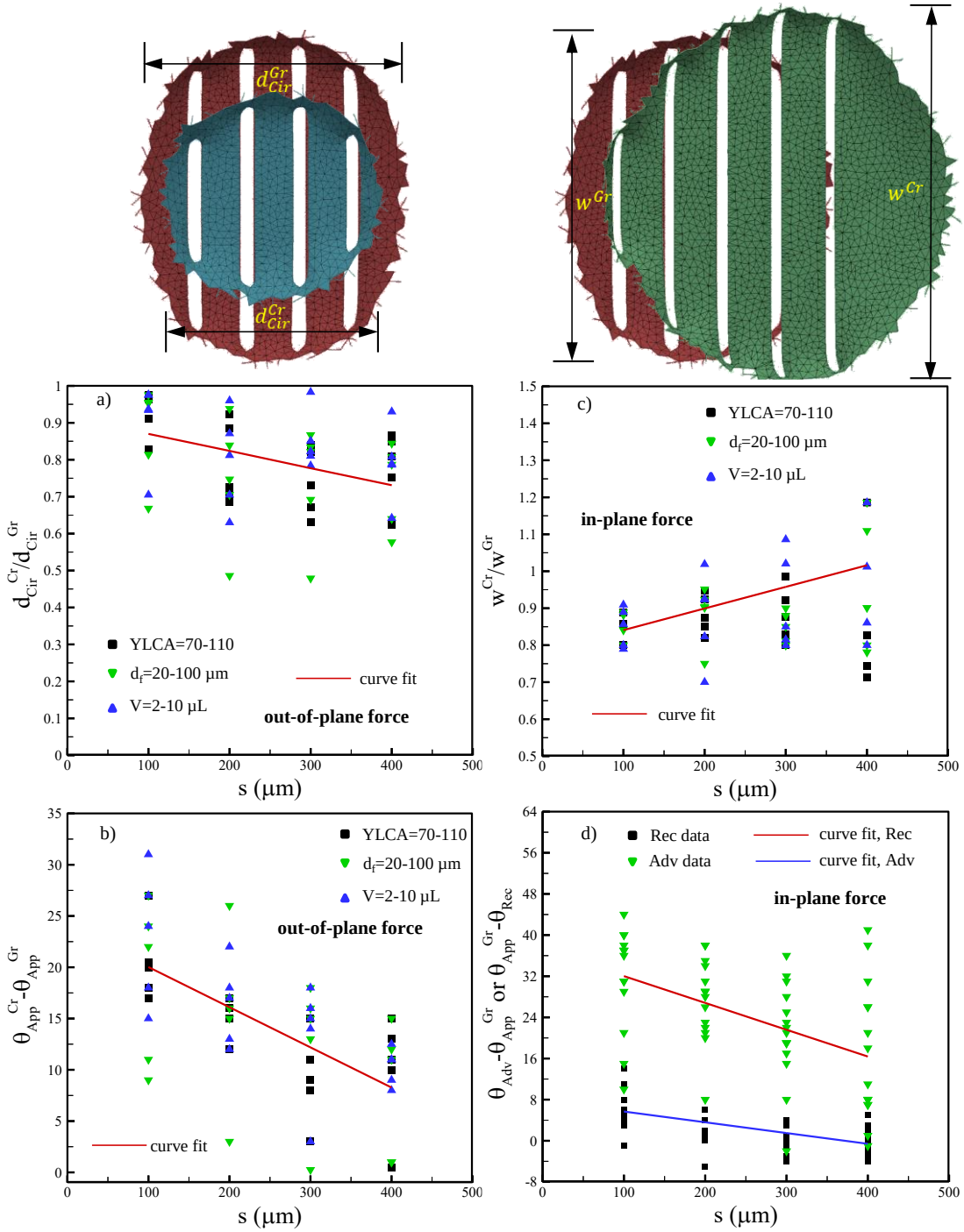

Figure 5.6: Droplet dimensions at the moment of detachment relative to those at rest under gravity are given in (a) and (b) for out-of-plane detachment, and in (c) and (d) for in-plane detachment. d_{Cir}^{Gr} , d_{Cir}^{Cr}, $d_{cir}^{Cr}/d_{Cir}^{Gr}$, w^{Cr}, w^{Gr} and $\frac{w^{Cr}}{w^{Gr}}$ are droplet diameter near the surface when the droplet is only under the gravity, droplet diameter near the surface at the moment of detachment, ratio of droplet diameter near the surface at the moment of detachment to that when the droplet is only under the gravity, droplet width at the moment of detachment, droplet width when droplet is only under the gravity, and the ratio of droplet width at the moment of detachment to that when the droplet is only under the gravity, respectively.

The above equations (Eqs. 5.1–5.5) can now be substituted in Eqs. 1.3 and 2.11 to produce easy-to-use correlations to estimate the force F_z required for the out-of-plane detachment of a droplet (or to move it on the surface F_x) knowing only the geometrical or wetting properties of the surface, i.e.,

$$F_z = \sigma\pi(\vartheta_1 s + \vartheta_2) d_{Cir}^{Gr}\, sin(\,\theta_{App}^{Gr} - \beta_1 s - \beta_2) - p\pi((\alpha_1 s + \alpha_2) d_{Cir}^{Gr})^2/4 \tag{5.6}$$

$$F_x = kw^{Gr}(\gamma_1 s + \gamma_2)\sigma\big(\cos(\delta_1 s + \delta_2 + \theta_{App}^{Gr}) - \cos(\theta_{App}^{Gr} - \varepsilon_1 s - \varepsilon_2)\big) \tag{5.7}$$

Following the work of [35], we have used a shape factor of k=48/π^3 in Eq. 5.7 to improve its prediction (a shape factor of $1<k<\pi$ has been reported in many previous studies [35, 40]). As mentioned earlier, a shape factor of k=48/π^3 was derived from first principle calculations accounting for the shape of the contact line and variation of the contact angle around the contact line [35]. Predictions obtained from Eqs. 5.6 and 5.7 are compared with our raw simulation data. While the absolute error $e_F = |\frac{F_{eq}-F_{SE}}{F_{SE}}|$ may reach as high as 150% for a few cases, they are generally about 70–80% on average. Note that these predictions (despite the errors) are obtained using only the properties of the fibers and droplets with no experimental or computation data as input. Using these equations, one can estimate the magnitude of the force needed to move or detach a droplet from a fibrous coating before the coating is made.

Figures 5.7a and 5.7b show our experimental detachment force data obtained for aqueous ferrofluid droplets with a volume of 4 µL on single-layer electrospun PS coatings comprised of parallel fibers with a diameter of about 0.5 µm but different fiber–fiber spacing. As mentioned earlier, Eqs. 1.3 and 2.11 can predict the force of detachment in the out-of-plane and in-plane directions, but these equations require droplet geometrical dimensions right before detachment from the surface, i.e., θ_{App}^{Cr} (the critical apparent contact angle) and d_{Cir}^{Cr} (droplet diameter near the surface at the moment of detachment, as shown in Figure 5.7c), and θ_{Adv}, θ_{Rec} (advancing and

receding contact angles) and w^{Cr} (droplet width at the moment of detachment, as shown in Figure 5.7d). This means that Eqs. 1.3 and 2.11 cannot be used for designing a surface prior to its manufacturing. This is in contrast to Eqs. 5.6 and 5.7 where detachment force can be predicted based solely on the dimensions of fibrous surface with no need for conducting an experiment or simulation with a droplet on the surface. It is important to mention that Eqs. 5.6 and 5.7 were obtained from simulations conducted for coatings with a fiber diameter of $20 < d_f < 100\ \mu m$ (and a fiber–fiber spacing of $100 < s < 400\ \mu m$) but they are used in this figure to predict the force of detachment from coatings with a fiber diameter of $d_f \cong 0.5\ \mu m$ (and $1 < s < 4\ \mu m$). This is because conducting a numerical simulation for a droplet as large as a few microliters on fibers as small as 0.5 μm in diameter (or producing fibers as large as 20–100 μm via electrospinning) are very challenging. One can obviously expect the predictions of Eqs. 5.6 and 5.7 to become more accurate when compared to experimental data obtained for coatings with larger fibers. One should also keep in mind that the fibers is the simulations are assumed to be spaced equally with respect to one another, which obviously is not the case in the experiments.

Note in Figure 5.7a that the out-of-plane detachment force is lower for larger fiber–fiber spacing due to droplet's smaller contact area with solid fibers, which is consistent with the decrease of d_{Cir}^{Cr} in Figure 5.7c (as θ_{App}^{Cr} remained nearly constant), leading to a smaller capillary force acting on the droplet. Figure 5.7b also shows smaller detachment force in the in-plane direction when the fiber–fiber spacing is larger. This trend is also consistent with how $\theta_{Adv} - \theta_{Rec}$ and w^{Cr} decrease with increasing spacing between the fibers. See our published paper for more details on this chapter [94].

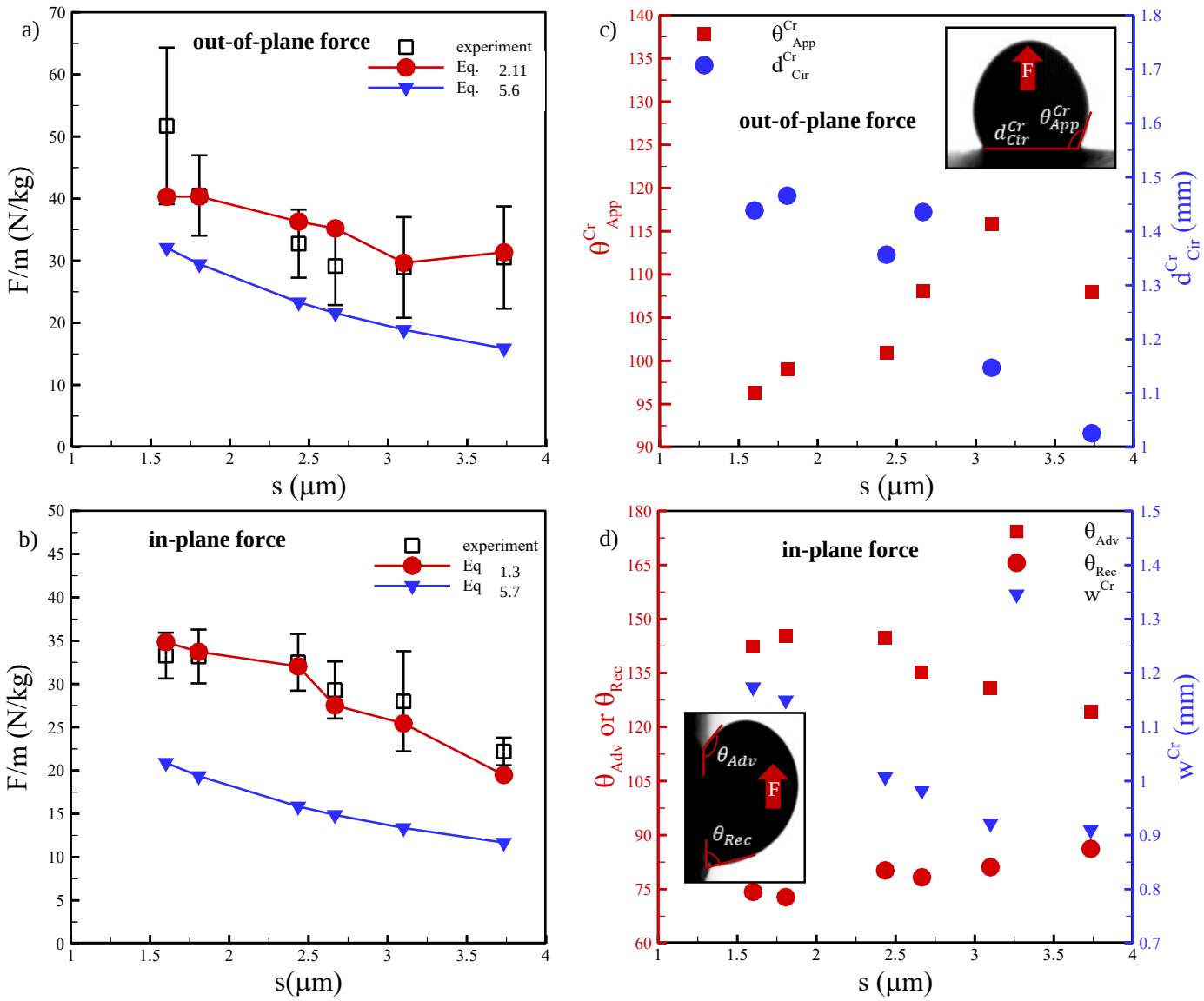

Figure 5.7: Droplet detachment force from experiment is compared to those from Eqs. 2.11 and 5.6 in (a) for out-of-plane detachment, and with those from Eqs. 1.3 and 5.7 in (b) for in-plane detachment. Droplet dimensions at the moment of detachment (needed as input for Eqs. 1.3 and 2.11) are given in (c) and (d) for out-of-plane and in-plane detachments, respectively.

While the energy minimization method of Surface Evolver was used to provide detail and useful information regarding the impact of NW microstructure on detachment force (i.e. Eq. 5.6 and 5.7). We therefore considered developing an in-house code to provide such prediction at a higher rate but with somewhat less accuracy if needed.

In order to predict droplet shape and droplet detachment force, the Young-Laplace equation can be considered. Therefore, we started by solving the Young-Laplace equation for a surface with a roughness represented with a cosine wave. The Young-Laplace equation (2-D for now) can be expressed as

$$\frac{\ddot{z}}{(1+\dot{z}^2)^{2/3}} = \rho g z + \Delta p_0 \tag{5.8}$$

where g is gravity in the z-direction and Δp_0 is a constant number. This is a non-linear second order differential equation that can be solved numerically using a MATLAB code. Figure 5.8a shows an example of a 2-D droplet profile under gravity for a cosine wave. It can be seen that droplet spreads more when the surface was made rougher (roughness makes a hydrophilic surface more hydrophilic). Figure 5.8b shows how a droplet profiles changes with vertical external force. It can be seen that a strong force is needed to detach the droplet from the surface. It should be noted that the tangent of surface to droplet profile is always remained as YLCA. Also, A is the area below profile and w is frequency of the cosine wave.

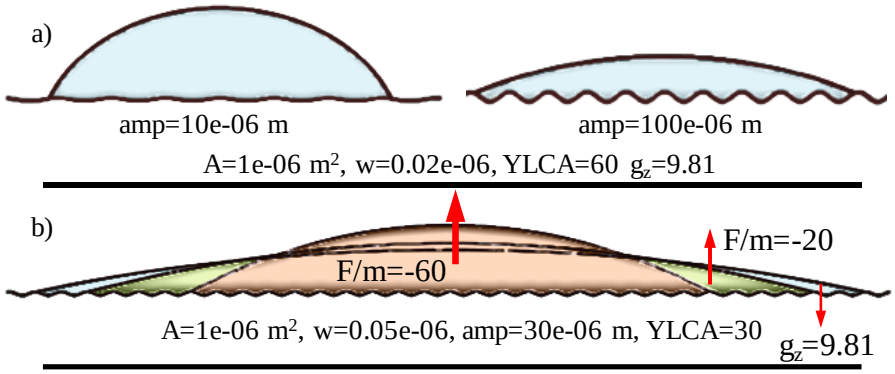

Figure 5.8. Examples of 2D droplet profile for 2 different amplitude of cosine wave in (a) and different external force in (b).

Effects of droplet volume (i.e. area in 2-D) on contact angle and detachment force is shown in Figure 5.9. It can be seen that a smaller force is needed for a droplet to be detached from the surface. This was also observed in our previous modeling results.

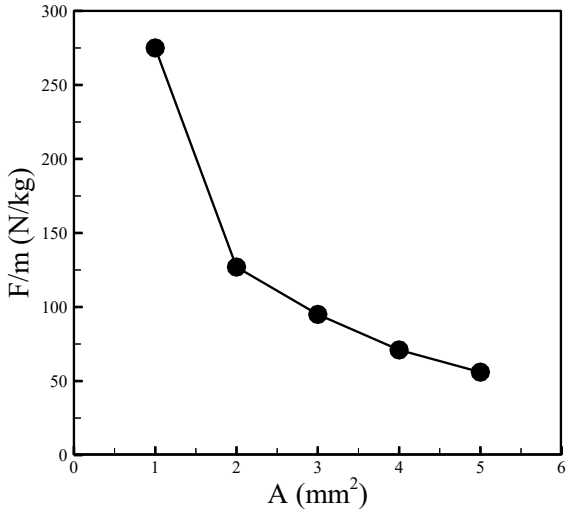

Figure 5.9. An example of our 2-D droplet detachment force modeling. Detachment force vs. droplet volume (area).

The MATLAB code that is developed to obtain droplet profile under gravity is also compared to the Surface Evolver simulation results. Figure 5.10 shows that there is a good agreement between the code and SE. The red line shows droplet profile using MATLAB code and blue profiles are obtained from SE.

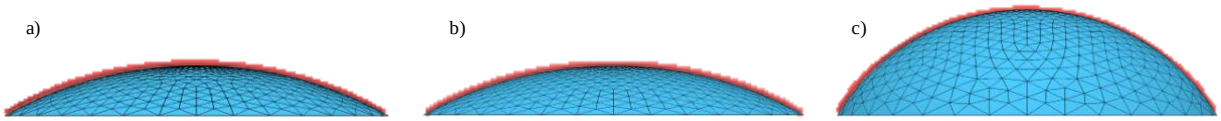

Figure 5.10. Comparison of droplet profiles under gravity obtained from the MATLAB code to SE. a) YLCA=30 V=2 µL b) YLCA=30 V=4 µL c) YLCA=60 V=4 µL.

Because there are many possible equilibrium shapes of droplet, the total energy of the system should be calculated. Generally, there are two main points in the energy plots which are local and global minimums. When a droplet is deposited on a surface, the droplet adjusts its location to go the local minimum energy. By shaking the surface, it is possible that droplet goes to its global minimum energy. We calculated the total energy to obtain droplet profile for all different possibilities. Figure 5.11 shows an example of a water droplet profiles on a flat surface with YLCA of 30 degrees and droplet volume of 4 µL as well as the total energy of the system for each profile. Both local and global minimum energies can be seen which the global one is close to 150 µm. This is also another advantage of this code compared to SE because SE results depend on the initial location of droplet that is deposited on the surface. Total energy calculated in the code has three main components similar to SE which are wetted surface energy, liquid energy and gravitational energy. In our code, since we use gravity as external force, therefore, this term of energy has a big impact on the total energy while it is small compared to the two other terms when there is no external force. It is also interesting that wetted surface and liquid energies work against each other. In another word, both of them become bigger as droplet spreads more on the surface but minimum energy of the system depends on how much the growth of each one is compared to the other one.

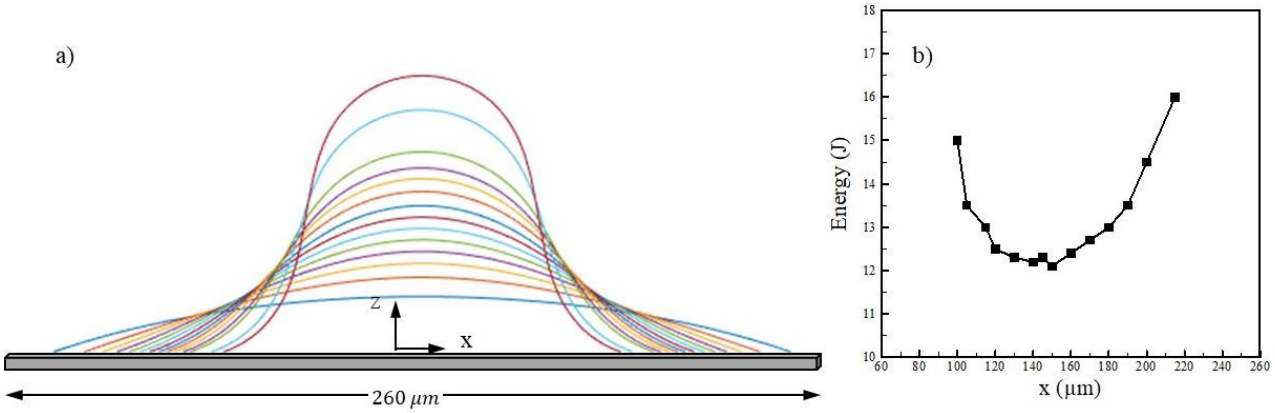

Figure 5.11. Different possible droplet profiles with volume of 4 µL on a flat surface with YLCA of 30 degrees in (a) and total energy of the system corresponding to the profiles in (b).

5.4. Conclusions

Conducting a series of digital experiments for a Cassie droplet detaching from a fibrous coating comprised of parallel fibers, it was observed that detachment force in both the out-of-plane and in-plane directions is lower when the fibers are smaller, when the spacing between them is larger, or when they are more hydrophobic. These simulation results (obtained for $70 < \theta^{YL} < 110,\ 20 < d_f < 100\ \mu m$, $100 < s < 400\ \mu m$ and $2 < V_a < 10\ \mu L$) were then used to produce semi-empirical correlations for the force required to detach a droplet from a hydrophobic fibrous surface in the in-plane and out-of-plane directions. These easy-to-use correlations only require the physical properties of the fibers (e.g., fiber diameter, fiber spacing, and fiber contact angle) and the droplet (e.g., volume and surface tension) as inputs. The work presented here advances the field by providing a means to optimize the surface geometry prior to manufacturing. The accuracy of our easy-to-use correlations was examined using experimental data obtained for droplet detachment from electrospun polystyrene mats with fibers having a diameter of about two orders of magnitude smaller than those considered in developing the correlations. The predictions in the in-plane and out-of-plane directions were found to be off by about 45% and 30%, respectively, on average. Despite the lack of perfect agreement, we believe that these correlations have practical values for product design and development as they do not require any experimental or computational data as input (they can be used prior to manufacturing). One can also expect the predictions of our correlations to be more accurate when compared with experimental data obtained for fibrous mats with larger fibers. The simulation method and/or the mathematical approach considered in this work can also be used in future studies to investigate droplet mobility on microfabricated (e.g., pillar-structured) surfaces.

Chapter 6. Force Measurement for Nonmagnetic Droplet Detachment from Fibrous Surfaces

6.1 Introduction

It was shown in the previous chapters that a ferrofluid droplet, magnet and a scale can be used to measure droplet detachment force. In this chapter, a nonmagnetic droplet detachment on a nonwoven surface will be measured in our setup. To do so, a small amount of a ferrofluid which is the secondary fluid here will be added to a nonmagnetic droplet which is the primary fluid. This way, a compound droplet will be formed. As the magnet gets closer to the compound droplet, the droplet deforms and eventually detaches. The scale will be used to measure the detachment force.

6.2. Method

A pendent compound droplet can be produced by nesting a small amount of water-based ferrofluid inside an oil droplet (a non-polar liquid) or by cloaking (engulfing) a water droplet (a polar liquid) with an oil-based ferrofluid. In the latter case (subject of interest in this paper), the oil can engulf the droplet completely or partially as shown in Figure 6.1a. In the absence of gravity, this can be determined using the so-called spreading coefficients $S_i = \sigma_{jk} - \sigma_{ij} - \sigma_{ik}$, (i ≠ j ≠ k = 1,2, 3). Considering phase 1, 2, and 3 denoting water, air, and ferrofluid, respectively, a compound water droplet will be completely engulfed if $S_1 < 0,\ S_2 < 0,\ S_3 > 0$, partially engulfed if $S_1 < 0, S_2 < 0, S_3 < 0$, and not engulfed if $S_1 < 0, S_2 > 0, S_3 < 0$ [95-98]. Partial cloaking is promoted here by using a high-surface-tension oil-based ferrofluid for the experiments (see Table 1). To estimate the interfacial tension between this ferrofluid and DI water we used the expression given in [99] where subscripts *w*, *of*, and *w-of* donate water, oil ferrofluid and water-oil ferrofluid, respectively,

$$\sigma_{w-of} = \frac{\cosh\left(\frac{\sigma_w}{k}\right)\sigma_w^{1-m} - \cosh\left(\frac{\sigma_{of}}{k}\right)\sigma_{of}^{1-m}}{\cosh\left(\frac{\sigma_w+\sigma_{of}-c\sigma_w^n\sigma_{of}^{1-n}}{k}\right)(\sigma_w+\sigma_{of}-c\sigma_w^n\sigma_{of}^{1-n})^{-m}} \quad (6.1)$$

where $m = 0.938$, $n = 0.949$, $c = 0.837$ and $k = 42.121$ mN/m. Using the above equation and Table 1, one obtains $\sigma_{w-of} = 46$ mN/m.

Table 1: Fluid properties at 25 C^0

Fluid	Density (kg/m^3)	Surface tension (mN/m)
Water	$\rho_w = 998$	$\sigma_w = 72$
Oil-based ferrofluid (APG2133)	$\rho_{of} = 1060$	$\sigma_{of} = 32$

Figure 6.1b shows a schematic of our experimental setup. The experiment starts by producing a DI water droplet using a New Era NE-300 syringe pump and placing it on a PS coating. The assembly was then turned upside-down and placed on a 3-D printed holder mounted on a sensitive scale (Mettler Toledo XSE105DU with an accuracy of 0.01 mg) connected to a computer. The scale was then zeroed and a small amount of an oil-based ferrofluid droplet (APG2133 purchased from Ferrotech, USA) was gently added to the water droplet (the weight shown on the scale was used to calculate the volume of the ferrofluid). The scale was again set to zero and a permanent magnet mounted on a Mitutoyo electronic height gauge was used to detach the resulting compound droplet. A digital high-speed camera (Phantom Miro Lab 340 with) with a Tokina 100 mm F 2.8 D lens was used to record the detachment process. Nikon D3100 camera with an AF-S micro Nikkor 105 mm lens was also used to take additional pictures when needed.

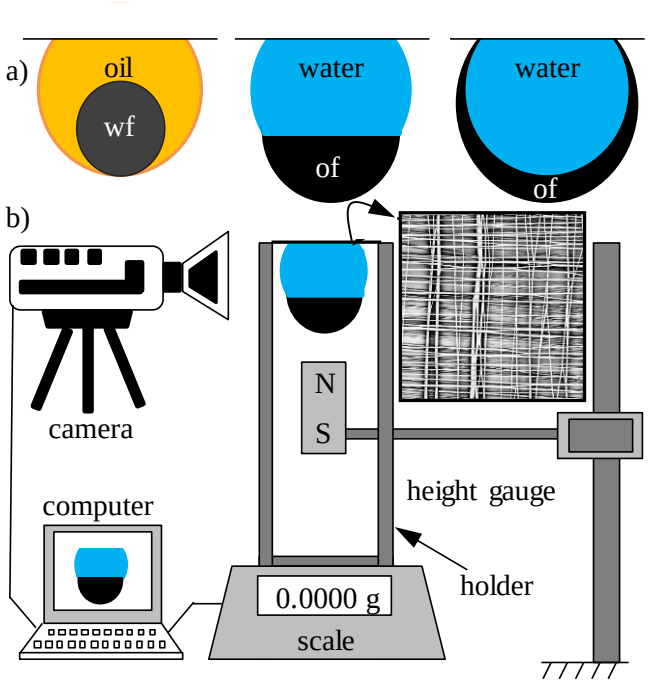

Figure 6.1. Schematic illustrations of a pendent compound droplet in the nested, partially-cloaked, and fully-cloaked configurations are given in (a). Our experimental setup is shown schematically in (b).

With the above choice of ferrofluid, one can prevent the ferrofluid from climbing up the water droplet to reach and spread into the PS coatings. Additionally, partial cloaking has a much smaller impact on the contact angle, contact line, and surface tension of the water droplet than its complete cloaking counterpart, for obvious reasons. Figure 6.2a shows the process of producing a pendent partially cloaked water droplet and detaching it using a permanent magnet. The water and ferrofluid volumes are 3 µL and 0.6 µL, respectively. Frame 1 shows the compound droplet under gravity. Frame 2 shows the compound droplet under an increased body force. Frames 3–5 show the spontaneous detachment of the compound droplet (irreversible) at the critical (detachment) force, followed by frame 6 where droplet residue left on the surface after detachment is shown. The evolution of the body force acting on the droplet is shown in Figure 6.2b. The volume of the residue is calculated using the last reading from the scale (frame 6).

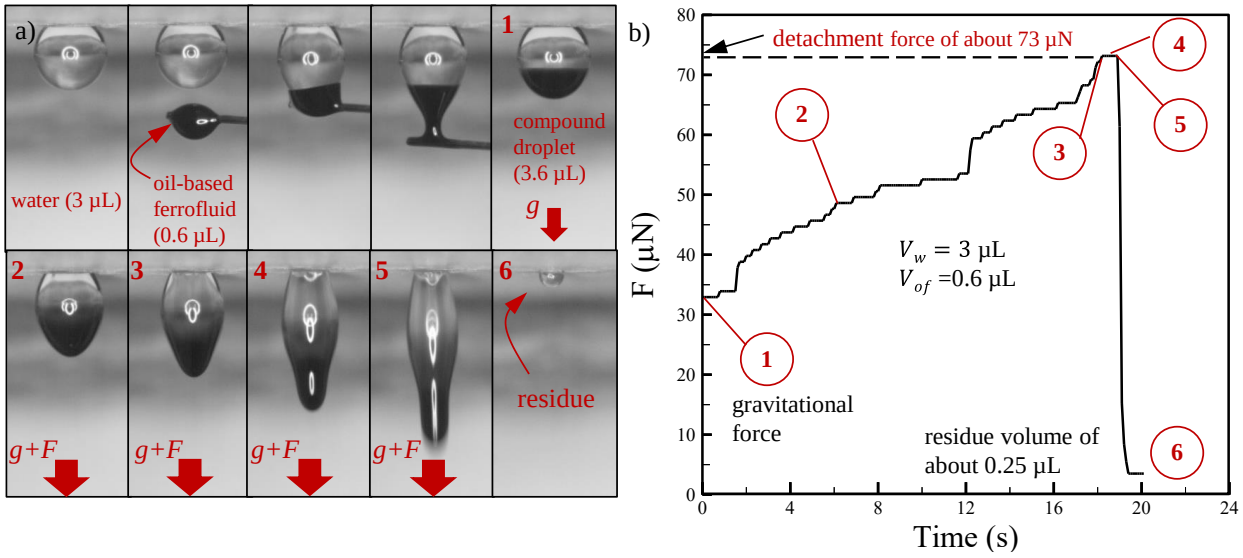

Figure 6.2. The process of adding an oil-based ferrofluid (0.6 µL in volume) to a pendent water droplet (3 µL in volume) and detaching the resulting compound droplet from an electrospun PS surface is shown in (a). An example of the force recorded by the scale during a detachment experiment is shown in (b).

Note that, under the influence of the magnetic field, the ferrofluid (and more so the suspended Fe_3O_4 nano-paticles in it) tends to move downward toward the magnet. Therefore, the magnetic force is applied mostly to the lower part of the droplet. This however has a negligible impact on the measured detachment force as the force transferred to the solid surface depends (mostly) on the magnitude of the net force acting on the water droplet, but does not depend on the location to which the force is applied. It should be mentioned that when the droplet deforms due to this effect (when the droplet shape becomes pointy), the pressure force applied to the solid surface changes, but this does not make a significant impact on the force of detachment.

The compound droplet shape is simulated using Surface Evolver (SE) in this work [89]. SE has shown to provide accurate predictions for single [45, 100-102] or multiphase [103-106] droplets interacting with a solid surface. The shape of a droplet under an external body force can be obtained by minimizing the total energy of the air–liquid-liquid–solid system using the following equation,

$$E = \sigma_{al}A_{al} + \sigma_{ll}A_{ll} - \sigma_{al}\cos\theta_{YL}\iint_{A_{sl}} dA + \iiint \rho_w gz dV + \iiint \rho_{of} gz dV \quad (6.2)$$

where ρ_w, ρ_{of}, θ_{YL}, A_{al}, A_{ll}, A_{sl} and V are water density, ferrofluid density, Young–Laplace Contact Angle (YLCA), air–liquid interfacial area, liquid–liquid interfacial area, solid–liquid interfacial area, and droplet volume, respectively. The simulations start by considering two cubic droplets on top of one another, and evolves through iterations to reach an equilibrium condition. The cube on the top represents the water droplet and the one on the bottom is the ferrofluid. The YLCA for a smooth sheet of PS is about 85 degrees, but to incorporate the effects of the roughness of the electrospun surface in our simulations with a smooth solid surface, we used the ACA of the droplets (measured experimentally) in place of the YLCA (SE ensures that the air–water interface along the contact line with solid smooth surface maintains a slope corresponding to the ACA of the water droplet with the PS coatings). This simplifies the otherwise very challenging task of simulating a droplet on a surface with micrometer-sized random roughness.

Our approach to simulate the effects of a magnetic force on a ferrofluid droplet, without actually simulating the magnetic field, has been to include an additional body force in our SE simulations of the droplet. This approach however does not work for a two-phase (cloaked) droplet since only a fraction of the droplet volume responds to a magnetic force. To circumvent this problem, we applied a fixed gravitational force per unit mass ($g = 9.81$ N/kg) to each phase, but artificially increased the density of the ferrofluid. In other words, we presented the gravitational energy in Eq. 6.2 with two terms ($\iiint \rho_w gzdV + \iiint \rho_{of} gzdV$) to also include the effects of magnetic force. With the help of this artificial density, we were able to emulate the condition where the water droplet was subjected to the earth gravity but the ferrofluid was under the influence of the magnetic force (obviously greater than the gravity). To obtain the force of detachment for the compound droplet, ferrofluid density was continuously increased until no equilibrium shape was achievable

for the pendent compound droplet. The detachment force was then calculated by knowing the detachment density of the ferrofluid and the mass of each phase, i.e.,

$$F_d = (\rho_{of,d} V_{of} + \rho_w V_w) g \tag{6.3}$$

Figure 6.3 compares compound droplet profiles (blue, red, and green represent air–water, air–ferrofluid, and ferrofluid–water interfaces, respectively) obtained from simulations with those from experiment for a water droplet with a volume of 3 µL partially-cloaked with different amounts of ferrofluids (figures in the second row show droplet cross-section (sliced from the middle) with the water–ferrofluid interface shown in green). Good general agreement between the simulation and experimental results is evident. For the simulations, we considered $\sigma_{w-of} = 42$ mN/m which is slightly lower than $\sigma_{w-of} = 46$ mN/m from the empirical correlation (curve fit) given in Eq. 6.1 (note that the root mean squared error for some of the experimental data used in producing Eq. 6.1 was as high as 4.14 mN/m) [99]. A detachment force of 73 µN was obtained from the numerical simulations reported in Figure 6.3 in good agreement with its experimental counterpart of 76 µN.

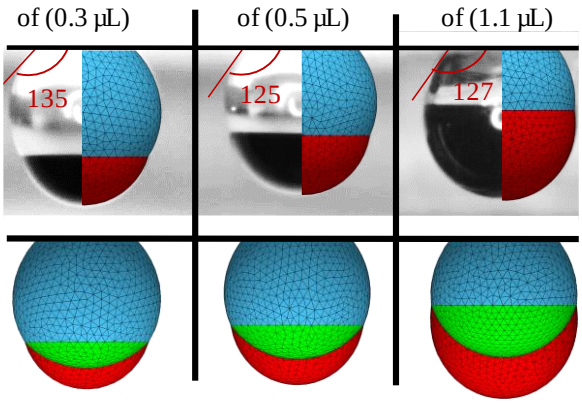

Figure 6.3. Side-by-side comparison between the experimental and computational compound droplets produced by adding different amount of ferrofluid to a water droplet with a volume of 3 µL. Blue, red, and green represent water–air, ferrofluid–air, and water–ferrofluid interfaces, respectively.

6.3. Results and Discussion

The surface considered in our experiments is a fibrous coating comprised of 3 layers of orthogonally stacked electrospun PS fibers. As mentioned earlier in the Introduction, the fully-cloaking method is not suitable for droplet detachment from a porous surface as the cloaking fluid can spread into the pores of the surface and further pin the droplet. The partial cloaking method on the other hand is a minimally-intrusive method that can be used to estimate the force of droplet detachment from a hydrophobic surface. In this section, we present a detailed analysis of the interplay between the interfacial forces acting on partially-cloaked multiphase droplets. We then used this information to create in a general-purpose phase-plot to be used in deciding on the volume and surface tension of the ferrofluid that is most suitable for detaching a water droplet from a given surface.

To use the partial-cloaking method, one needs to know the volume of the ferrofluid required for the experiment. This is important as the volume of the ferrofluid should be large enough to impart sufficient body force to the water droplet, but small enough so that it does not reach up and spread into the PS surface. Figure 6.4a shows an example where the volume of the ferrofluid (0.2 µL) was insufficient for a successful detachment of a 3 µL water droplet. The frames in this figure show the steps in making the compound droplet and in applying a magnetic force on it. As can be seen in frames 1 through 6, applying a magnetic force to such a droplet results only in the separation of the ferrofluid cloak from the water droplet. Comparing the forces recorded for frame 1 and frame 6 in Figure 6.4b, it can be seen that the volume of the water droplet after ferrofluid separation is about the same as that measured before the ferrofluid was added (within the expected margin of error). Also note in this figure that the maximum achievable force was about 53 µN which is much less than 76 µN needed to detach the water droplet from the surface.

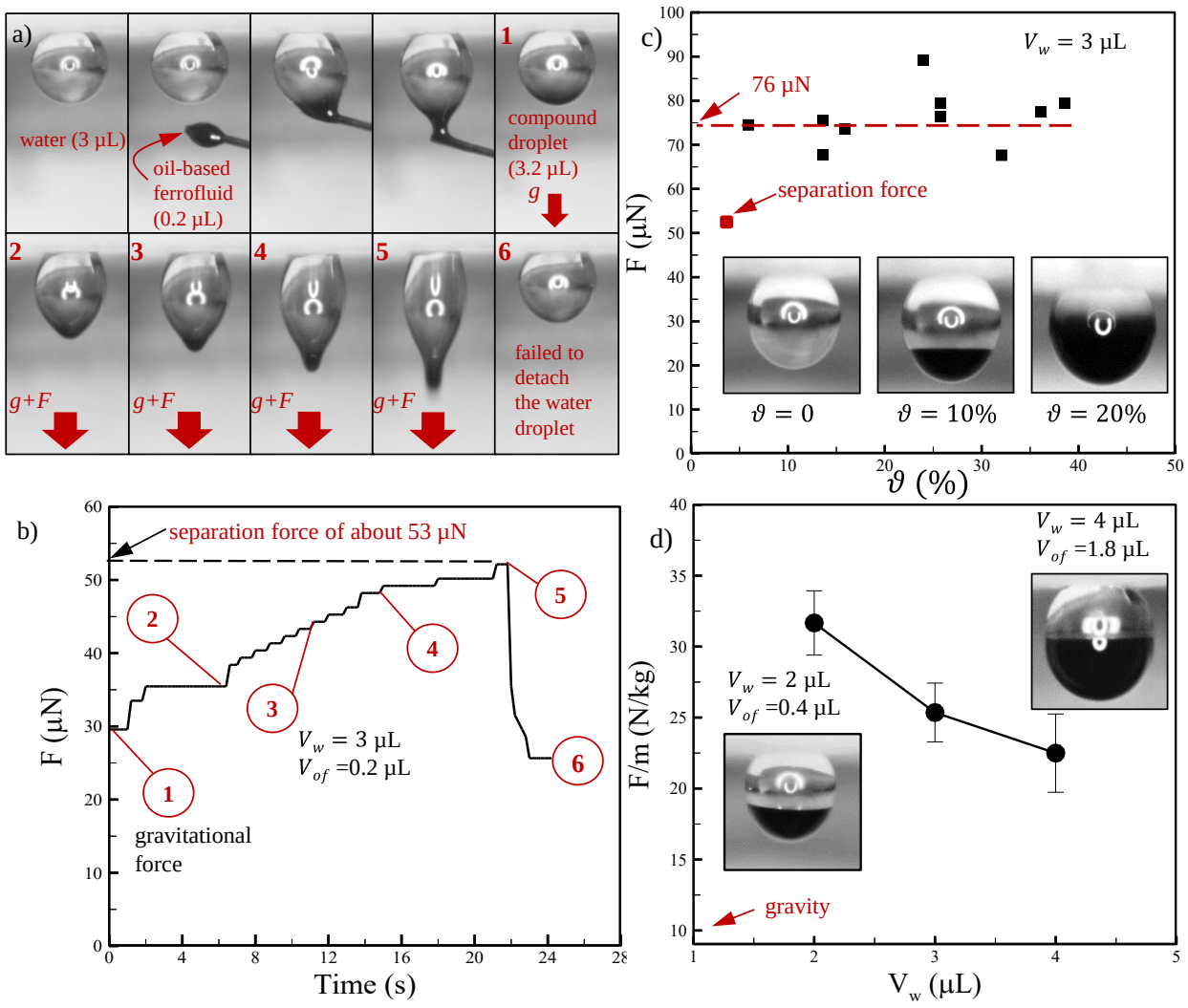

Figure 6.4. A failed experiment in which the ferrofluid volume was insufficient for droplet detachment is shown in (a) along with its force recordings in (b). Compound droplet detachment force versus ferrofluid volume ratio ϑ is shown in (c). Force of detachment per unit mass of droplet (N/kg) is measured via partial cloaking for water droplets of different volumes in (d).

Figure 6.4c shows the force of detachment measured for a water droplet with a volume of 3 µL from the above PS coatings cloaked partially with different amounts of ferrofluid (presented as ferrofluid volume ratio $\vartheta = V_{of}/V_w$). As shown in Figure 6.4c, a minimum ferrofluid volume ratio of $\vartheta = 10\%$ is needed to detach a 3 µL water droplet from our PS surface. In addition, it can be seen that the force required to detach such a compound droplet is independent of the volume of

the ferrofluid used for cloaking. This is a unique attribute of the proposed partial cloaking approach, and it is in contrast to the fully cloaking method. Figure 6.4d shows the detachment force (per unit mass) measured for water droplets of different volumes. It can be seen that detachment force per unit mass decreases with increasing droplet volume in agreement with those reported previously in [90] for water-based ferrofluids on similar (but not identical) PS coatings.

To compare the results of our partial cloaking droplet detachment method with an alternative but intrusive detachment method, we conducted a set of experiments in which we detached a water droplet from our PS coatings using a nylon fishing line having a diameter of 210 μm. This was done by first bringing the fishing line into contact with the droplet to create an asymmetric liquid bridge and then by moving it back to stretch the droplet until droplet detached from the PS surface (see [107]). This experiment was conducted on the setup shown in Figure 6.1 with the forces applied to the PS surface recorded by the scale. Recordings from the scale showed a detachment force of 94 ± 8.9 μN for a 3 μL water droplet (averaged over 5 repetitions) and a small residue with an average volume of about 0.3 μL on the PS surface. This force is close, but is not identical, to the force obtained using the partial cloaking method, 76 ± 6.2 μN for the same droplet volume. The observed 20% mismatch between the two methods can be attributed to many factors including the inherent geometrical differences between a pendent droplet and an asymmetric liquid bridge (between a flat surface and a fiber). A second reason for the mismatch could be the errors associated with in our partial-cloaking method: we chose our oil-based ferrofluid based on a water–oil surface tension estimate obtained from the approximate correlation given in Eq. 6.1. It is not impossible to assume that an invisible (nanometer thick) film of oil has formed over the water droplet all the way to the contact line, and has affected our original assumption (that the only fluid in contact with the PS is water). Given the complexity of the four-phase interfacial problem at

hand, it is hard to prove or disprove such a possibility. In addition (a third reason), it is possible that some surfactant in the oil-based ferrofluid has interacted with water and lowered its surface tension by 10–20%. Nevertheless, the extent to which these issues might have affected our results seems to be quite small. For instance, one can compare the apparent contact angle of the water droplet before and after adding the oil-based ferrofluid in Figure 6.2a or Figure 6.4a. Whether or not a nanometer thick film of oil has fully cloaked the water droplet (or if the water surface tension is slightly lowered), its impact on droplet shape or droplet's apparent contact angle seems to be small.

Figures 6.5a–6.5d show a water droplet with a volume of 3 μL cloaked with different amounts of ferrofluid. For each case, the magnetic body force acting on the droplet was increased from zero (leaving gravity as the only body force) to a maximum force at which no equilibrium shape was predicted for the compound droplet. This critical force is different for droplets made with different ferrofluid volume ratios (the values with red underlines). As stated earlier in discussing Figures 6.2 and 6.4, increasing the magnetic force on a compound droplet results either in the detachment of the water droplet from the surface or in the separation of the ferrofluid from the water droplet. Figure 6.5e shows the critical forces (acting on the solid surface) obtained for compound droplets of different ferrofluid volume ratios. It can be seen that the critical force increases with increasing the ferrofluid volume but reaches a plateau at about $\vartheta = 9.5\%$. Comparing this behavior with the behavior observed experimentally (where the measured force of droplet detachment was independent of the volume of the ferrofluid used for partial cloaking), it can be concluded that the simulated critical force is in fact the force needed to detach the water droplet when $\vartheta > 9.5\%$. On the other hand, applying a magnetic force to a compound droplet with $\vartheta < 9.5\%$, results only in

the separation of the ferrofluid, and the simulated critical force is the force needed for this fluid–fluid separation.

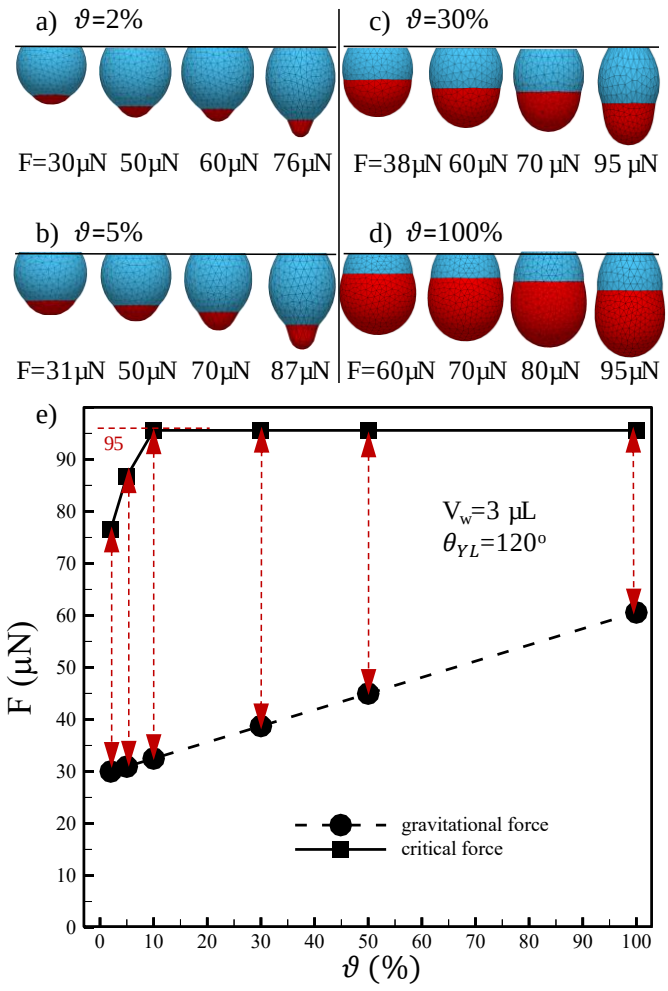

Figure 6.5. Simulation results for the shape of a partially cloaked water droplet under the influence of gravitational and magnetic forces are given in (a) through (d) for different ferrofluid volume ratios ϑ. The water droplet is 3 µL in volume and maintains a YLCA of 120° with the solid surface. Simulation results for the critical and gravitational forces are given in (e) for compound droplets having different ferrofluid volume ratios.

The weight of the above compound droplets is added to Figure 6.5e for comparison, and it can be seen that the difference between the force of detachment and droplet's weight decreases with increasing ϑ. This means that increasing the ferrofluid volume, the resulting compound droplet will eventually detach from the surface under its own weight.

A force analysis is presented here to better our understanding of how a partially-cloaked (two-phase) droplet can be detached from a surface using a magnetic force. Consider a free body diagram for the compound droplet as shown in Figure 6.6a. The balance of forces in the *y*-direction can be written as,

$$F_{d,y} = F^{\sigma}_{w,y} - F^{p}_{w,y} \tag{6.4}$$

where $F^{\sigma}_{w,y} = \pi\sigma_w d_w sin\theta^{app}_w$ and $F^{p}_{w,y} = \pi p_w d^2_w/4$ are the capillary force and pressure force acting on the water droplet at the solid surface, respectively, and $F_{d,y}$ is the total body force acting on the compound droplet. In this equation d_w, θ^{app}_w, and p_w are the base diameter, apparent contact angle, and droplet pressure, respectively. Likewise, considering a free body diagram for the ferrofluid droplet as shown in Figure 6.6b, one can write the balance of forces in the *y*-direction as,

$$F_{s,y} = F^{\sigma}_{of,y} - F^{p}_{of,y} \tag{6.5}$$

where $F^{\sigma}_{of,y} = \pi\sigma_{of} d_{of} \sin\theta^{app}_{of}$ and $F^{p}_{of,y} = \pi p_{of} d^2_{of}/4$ denote the capillary and pressure forces for the ferrofluid droplet, respectively, and $F_{s,y}$ is the force acting to separate the ferrofluid from the water droplet. The parameters d_{of} and θ^{app}_{of} denote the ferrofluid base diameter and ferrofluid apparent contact angle (angle with a horizontal plane going through the line of contact with water), respectively, and p_{of} represents the ferrofluid pressure. The separation force $F_{s,y}$ can also be calculated using the water droplet information (see the second free body diagram shown in Figure 6.6b), as

$$F_{s,y} = F^{\sigma}_{of,y} + F^{\sigma}_{w-of,y} - F^{p}_{w-of,y} \tag{6.6}$$

where $F^{\sigma}_{w-of,y} = \pi\sigma_{w-of} d_{of} sin\theta^{app}_{w-of}$ and $F^{p}_{w-of,y} = \pi p_{w-of} d^2_{of}/4$ denote the surface tension force for the water–ferrofluid interface and the water pressure force on that interface, respectively.

In this equation, p_{w-of} represents the pressure on the water–ferrofluid interface (water droplet pressure p_w plus the hydrostatic pressure). The geometric parameters and droplet pressures shown in Eqs. 6.4–6.6 are obtained from our SE simulations and are shown in Figures 6.6c and 6.6d versus body force magnitude. It can be seen that pressure inside the water droplet slowly decreases with increasing the magnetic force or with increasing the volume ratio of the ferrofluid. This means that the shape of the water droplet deviates only slightly from a spherical shape under the influence of an increasing magnetic force (until it detaches from the surface). On the other hand, the pressure inside the ferrofluid droplet decreases significantly with increasing the magnetic force when the ferrofluid volume ratio is small (ferrofluid droplet significantly elongates with increasing the magnetic force). It is interesting to compare the elongated shapes of the ferrofluid droplets of different volumes at their specific critical forces in Figures 6.5a–6.5d.

Figure 6.6d shows the base diameter for the water droplet at the solid surface d_w and that for the ferrofluid droplet at a horizonal plane going through the line of contact with water d_{of}. It can be seen that d_w decrease with increasing the magnetic force on the droplet as the area of contact between water and solid surface decreases as the droplet becomes closer to the moment of detachment. For the ferrofluid, d_{of} decreases with force mostly because it moves downward on the surface of the water droplet (see Figures 6.5a–6.5d). Obviously, d_{of} is more sensitive to ϑ as it is more strongly dependent on the volume of the ferrofluid droplet.

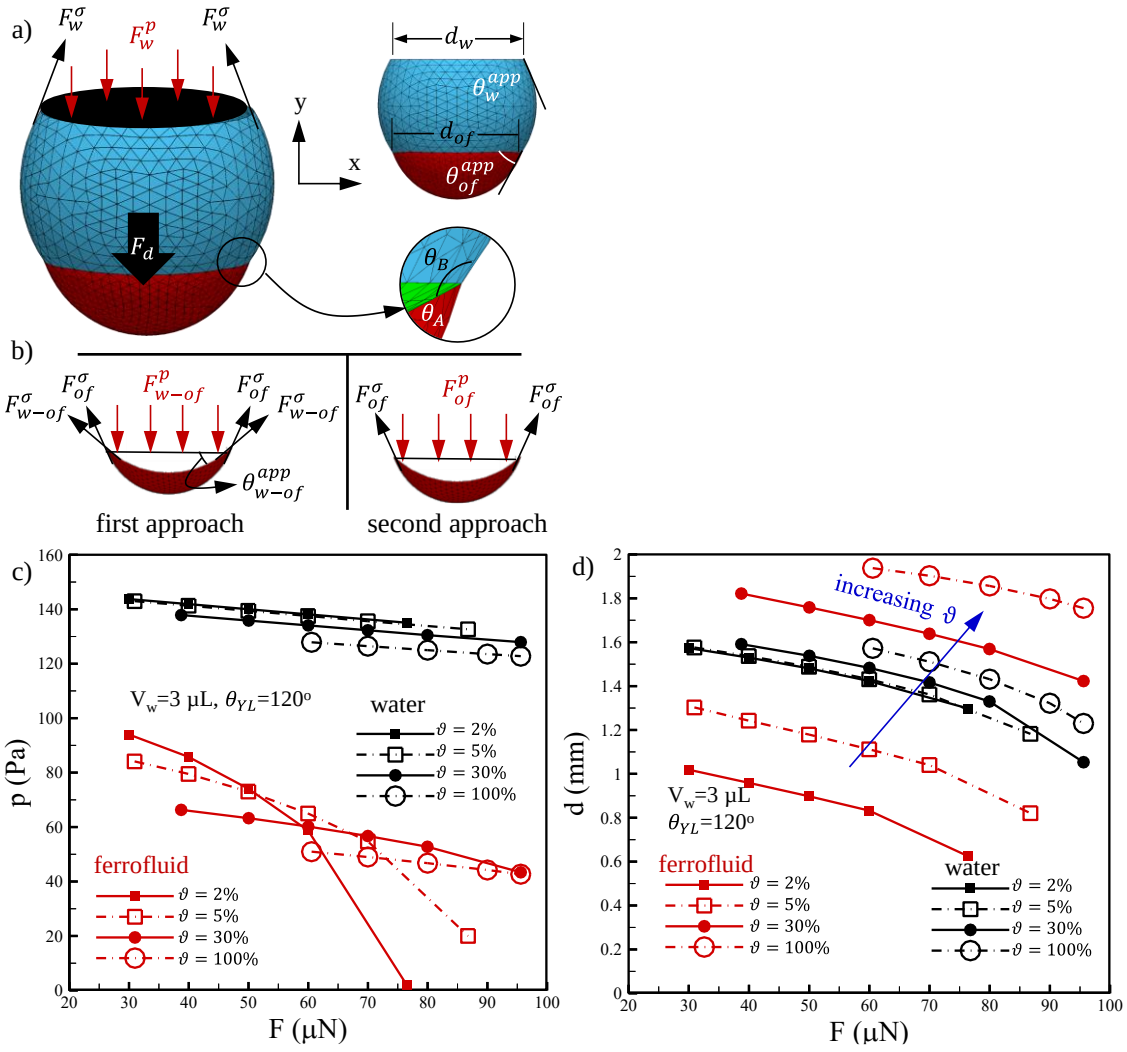

Figure 6.6. A free body diagram showing the forces acting on a partially cloaked water at its contact with the solid surface is given in (a). Two different ways of depicting the forces acting on the ferrofluid cloak are shown in (b). Pressure at water–solid (for water droplet) and water–ferrofluid (for ferrofluid droplet) interfaces and base diameter under the influence of an enhanced body force are shown in (c) and (d), respectively, for compound droplets with different ferrofluid volume ratios (starting points represent the weight of the compound droplets).

As was shown earlier using the spreading factor, the oil-based ferrofluid used in our experiments cloaks the water droplet only partially. Considering the balance of forces acting on the three-phase contact line in the absence of an external body force such as gravity, one can obtain the contact angles between the three phases involved, θ_A and θ_B, using the following equations (i.e., the Neumann triangle) [108-110]:

$$\sigma_{w-of} cos\theta_B + \sigma_w + \sigma_{of} \cos(\theta_A + \theta_B) = 0, \quad (6.7)$$

$$\sigma_{w-of} cos\theta_A + \sigma_{of} + \sigma_w \cos(\theta_A + \theta_B) = 0. \quad (6.8)$$

With the surface tension values known, one can solve these equations to obtain $\theta_A = 27^o$ and $\theta_B = 168^o$ in perfect agreement with the predictions of our two-phase numerical simulations conducted in the absence of a body force (see Figure 6.6a). In the presence of an external body force however, the contact angles obtained from the simulations show higher values for θ_B but smaller values for θ_A, confirming that Neumann triangle is only accurate in the absence of a body force (see Figure 6.7). Figure 6.7 also shows the ACA (defined with respect to the horizon) for the water droplet θ_w^{app} at two different ferrofluid volume ratios of $\vartheta = 5\%$ and ϑ =100%. It can be seen that, θ_w^{app} does not change with increasing the magnetic force on the droplet. On the other hand, the ACA for the ferrofluid droplet θ_{of}^{app} increases significantly when $\vartheta = 5\%$ (where ferrofluid separates from the water droplet), but decreases mildly when $\vartheta = 100\%$. It is also interesting to notice that θ_{of}^{app} converges to 90 degrees regardless of the volume of the ferrofluid droplet.

To isolate and study the effects of ferrofluid volume on the droplet capillary and pressure forces, we have plotted these forces individually for both the water and ferrofluid droplets in Figures 6.8a–6.8c in the absence of a magnetic force (when gravity is the only body force acting on the droplet) and at the moment of detachment. It can be seen in Figure 6.8a that $F_{w,y}^p$ decreases slowly with increasing ϑ but $F_{w,y}^\sigma$ remains almost a constant (because d_w and θ_w^{app} do not depend on ϑ strongly, as discussed earlier in Figure 6.6). $F_{of,y}^\sigma$ and $F_{of,y}^p$ on the other hand, increase with ϑ to reach a plateau (as d_{of} reaches a constant diameter about the spherical diameter of the water droplet). The difference between $F_{w,y}^\sigma$ and $F_{w,y}^p$ represents the weight of the compound droplet and it obviously increases with increasing ϑ.

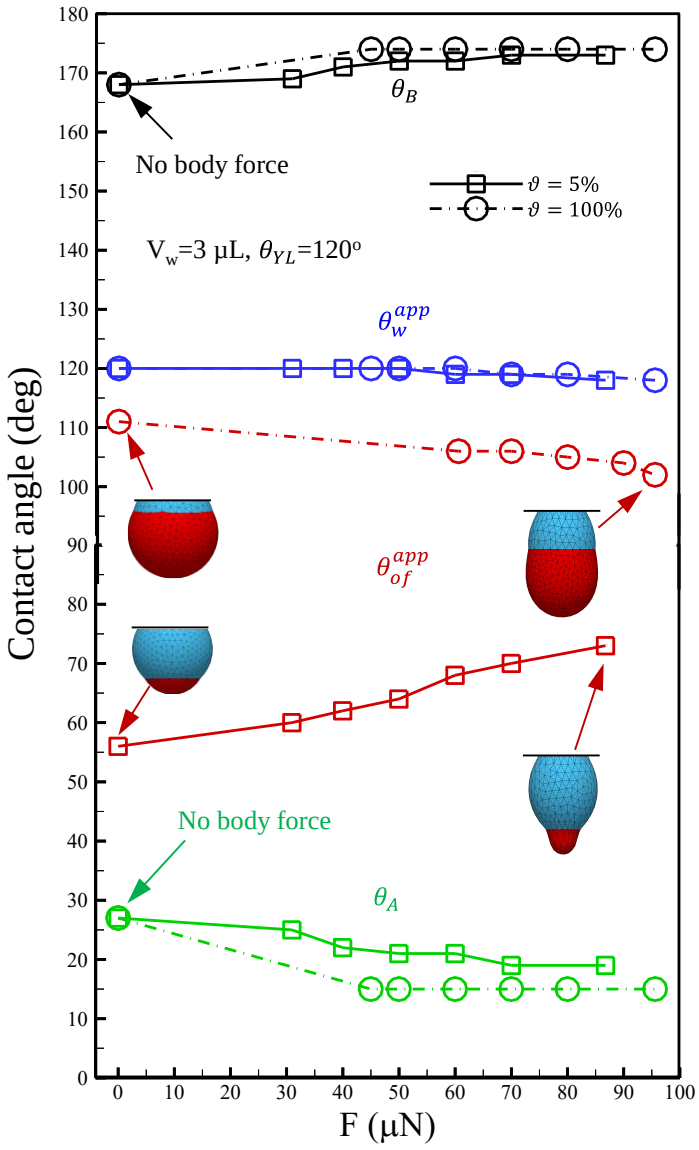

Figure 6.7. Contact angles between water and ferrofluid θ_A and θ_B are shown under the influence of an enhanced body force for compound droplets with two different ferrofluid volume ratios. Apparent contact angles for water and ferrofluid droplets θ_w^{app} and θ_{of}^{app} (measured with respect to horizon) are also given for comparison. Water droplet volume and YLCA are 3 μL and 120°, respectively.

Effects of increasing the volume ratio of the ferrofluid on capillary and pressure forces are different when the total body force acting on the droplet (magnetic plus gravitational) is at the critical value (Figures 6.8b and 6.8c).

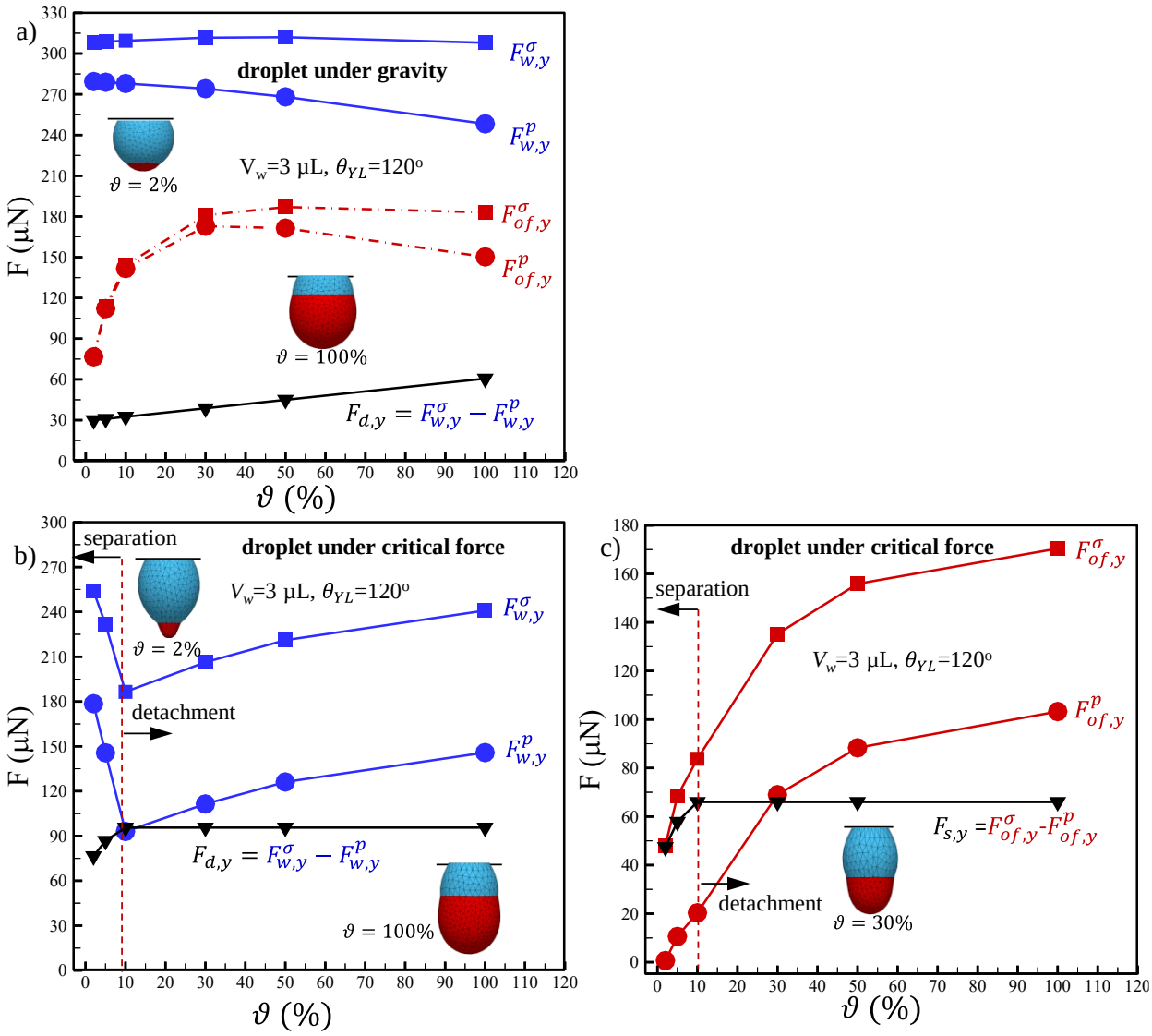

Figure 6.8. Force components acting on water and ferrofluids are calculated for compound droplets with different ferrofluid volume ratios. Figure (a) is for when the compound droplet is under the influence of gravity, whereas (b), for water droplet, and (c), for ferrofluid droplet, are at the critical moment. The water droplet has a volume of 3 µL and it is on a surface with a YLCA of 120°.

For the water droplet (Figure 6.8b), these forces first decrease with ϑ but then increase, and the ferrofluid volume ratio at which $F^{\sigma}_{w,y}$ and $F^{p}_{w,y}$ reach a minimum ϑ^* denote where a transition from the ferrofluid-separation regime (failed experiments) to the water-droplet-detachment regime takes place. It is also interesting to note that $F_{d,y}$ (the difference between $F^{\sigma}_{w,y}$ and $F^{p}_{w,y}$) increases with

increasing ϑ at first but then it reaches a constant value after $\vartheta = \vartheta^*$. For the ferrofluid droplet (Figure 6.8c), F_{of}^{σ} and F_{of}^{p} increase for all ϑ values as d_{of} increases with ϑ.

To further expand the use of the proposed partial cloaking method to detach water droplets of different volumes from a sticky hydrophobic surface, we calculated the minimum required ferrofluid volume ratio $\vartheta^*$for a reasonable range of ferrofluid surface tensions $24 < \sigma_{of} <$32 mN/m, as can be seen in Figure 6.9. We considered surfaces with three different YLCAs (or three different ACAs in the case of working with rough surfaces) of 100, 110, and 120 degrees. For the sake of presentation clarity, we have plotted these data in the form of shaded bands, with the ferrofluid surface tension deceasing in each band from $\sigma_{of} = 32$ mN/m on the left (shown with a red line) to $\sigma_{of} = 24$ mN/m on the right (shown with a blue line). Water droplets with a volume on the right side of the constant-surface tension lines will be detached successfully from the surface for each YLCA. Consider for instance a water droplet with a volume of $V_w = 10.5\ \mu L$ on a surface with an YLCA of $\theta_{YL} = 110^o$. This droplet can be detached using a ferrofluid with a surface tension of $\sigma_{of} = 32$ mN/m with a volume greater than about 0.75 µL ($\vartheta^* = 7.5\%$), a ferrofluid with a surface tension of $\sigma_{of} = 24$ mN/m with a volume greater than 3.1 µL ($\vartheta^* = 30\%$), or any other ferrofluid with a surface and volume in between the above values (see green dotted lines in Figure 6.9) as long as they all have the same magnetization strength (Iron nanoparticle concentration).

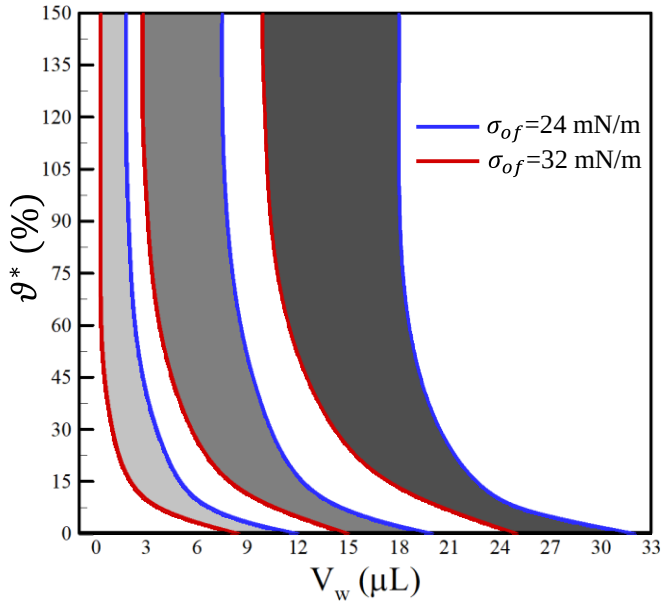

Figure 6.9. Minimum ferrofluid volume ratio ϑ^* required for successful detachment of a water droplet is plotted versus water droplet volume for different ferrofluid surface tensions and surface YLCAs. The surface tension for the lower and upper bounds of the shaded areas are 24 and 32 mN/m, respectively.

We used our numerical simulations to further examine the accuracy of partial cloaking method in emulate detachment of a pure water droplet from a surface. To this end, we compared detachment force values obtain for water droplets of different volume in the presence and absence of a ferrofluid cloak in Figure 6.10a for two different YLCAs. We also added our experimental data to this figure for comparison. It can be seen that detachment force for a pure water droplet is about 20–30% higher than that of its partially cloaked counterpart. To further explore the reasons behind obtaining different forces, we plotted the pressure inside these droplets in Figure 6.10b for the case of a water droplet with a volume of 7 µL and a YLCA of 110 degrees. It can be seen that the average pressure inside the partially cloaked droplet is less than that of the pure water droplet. This is due to the flattening that occurs at the bottom of the water droplet resulting in a lower Laplace pressure inside the water droplet (note that the area of contact between water and ferrofluid is exposed to an interfacial tension lower than water surface tension, i.e., $\sigma_{w-of} < \sigma_w$). Figure 6.10b

compares the pressure inside the water droplet p_w in presence and absence of ferrofluid cloaks. A higher p_w results in a higher $F_{w,y}^{p}$which causes the difference between $F_{w,y}^{\sigma}$ and $F_{w,y}^{p}$ (i.e. the detachment force) to become smaller ($F_{w,y}^{\sigma}$ is always bigger than $F_{w,y}^{p}$). Note that the area of contact between water and solid surface does not change significantly with adding the ferrofluid.

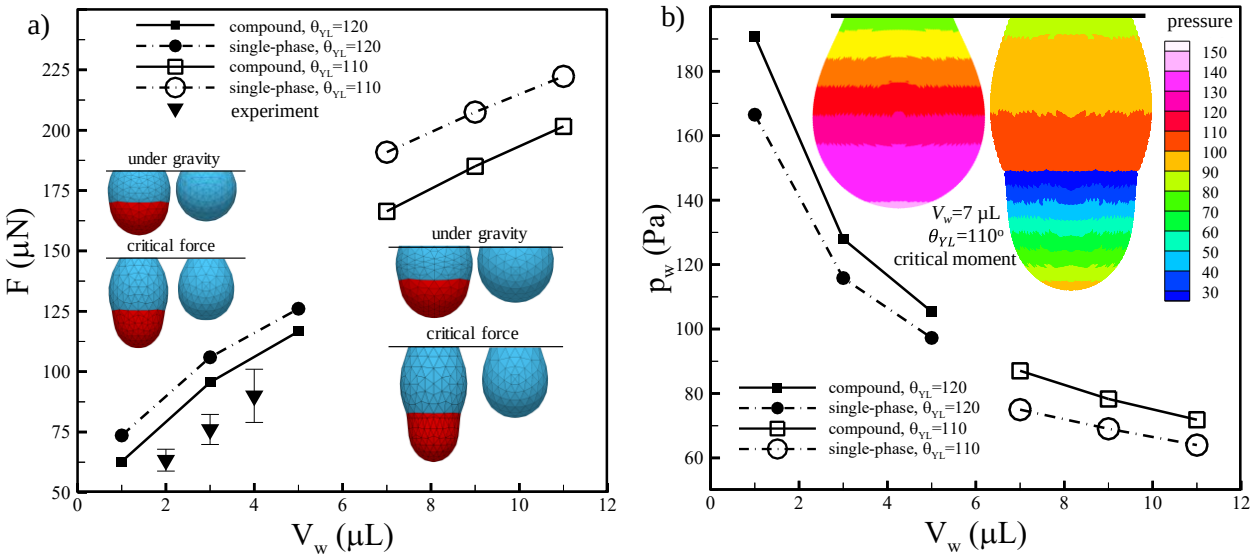

Figure 6.10. Comparison between simulated detachment forces for pure and partially-cloaked water droplets is given in (a) for different water droplet volumes and YLCAs. $\theta_{YL} = 120$ and $V_w = 5\ \mu L$, for the droplets shown in the left inset, and $\theta_{YL} = 110$ and $V_w = 7\ \mu L$, for the droplets shown in the right inset. Water droplet pressure at the water–solid interface versus water droplet volume for YLCAs of 110° and 120° are given in (b). The inset figure shows pressure contours inside a water droplet with the volume of 7 μL and a YLCA of 110° with and without of a ferrofluid cloak.

With regards to the comparison between the experimental and computational results, it should be note that the YLCA for the PS coatings generally varies in the range of $125^o < \theta_{YL} < 135^o$ as was shown earlier in Figure 6.3, and a perfect agreement can only be achieved by inputting the exact ACA from experiment (see the text describing Figure 6.3). See our published paper for more details on this chapter [111].

6.4. Conclusions

The concept of partial cloaking is used in this study to develop a new technique to measure the force needed to detach nonmagnetic (e.g., water) droplets of different volumes from hydrophobic surfaces (e.g., electrospun polystyrene coatings) using a magnet in a simple test setup. Partial cloaking is achieved through the use of high-surface tension oil-based ferrofluids that are unable to completely cloak a pendent water droplet (does not contaminate the solid surface), but can be used to impart enough body force to detach the droplet from the surface. Our experimental and computational results revealed that the detachment force obtained via partial cloaking is independent of the volume of the ferrofluid used in the experiment as long as the ferrofluid volume is greater than a minimum value (applying a magnetic force to a droplet with insufficient ferrofluid results only in the separation of the ferrofluid from water). The above minimum ferrofluid volume depends on the volume of the water droplet and increases with decreasing the surface tension of the ferrofluid or the YLCA of the surface. Our results indicate that the detachment force obtained via partial cloaking of a water droplet is within about 20–25% of the detachment force expected for the droplet. In this chapter, we also developed a new approach to simulate the effects of magnetic force on a partially cloaked water droplet, without actually simulating the magnetic field. To do this, we considered gravity as the only body force acting on the entire compound droplet, but artificially increased the density of the ferrofluid to emulate the effect of magnetic field, for the first time.In short, we presented a novel method to measure the force of detachment for a water droplet from a hydrophobic surface. We also provided an insightful analysis into the complex nature of this multiphase problem, and thereby developed a general-purpose plot (Figure 6.9) that extends the application of our work to other oil–water–solid combinations.

Chapter 7. Overall Conclusion

Droplet adhesion, mobility and penetration into an electrospun PS coatings are studied experimentally and computationally in this work. To initiate water droplet detachment or penetration into our hydrophobic fibrous coatings (electrospun polystyrene), we used aqueous ferrofluid droplets for our experiment so that the body force on the droplets could be enhanced using a magnet (as the earth gravity was not enough), and droplet detachment or penetration could be induced. Depending on the spacing between the fibers (and of course fiber and droplet diameters), a droplet on an electrospun PS coating can be at the Cassie state, at the Wenzel state, or at a transition state in between these extremes' states. It appeared from our experiments that the Cassie (or near-Cassie) droplets leave a much smaller residue on the surface after sliding compared to the Wenzel (or near-Wenzel) droplets. The combined experimental-computational study for the droplet adhesion showed that the droplet detachment force decreases with increasing fibers' YLCA. It was also observed that droplet detachment force decreases or remains relatively constant with increasing fiber-to-fiber spacing depending on the number of layers of fibers in contact with the droplet. Our results from the droplet mobility study indicate it is generally higher when the spacing between the fibers is larger. Droplet penetration study showed that increasing the relative angle between the fibers, in the range of angles from zero (parallel fibers) to ninety degrees (orthogonal fibers), increases the resistance of the material to droplet penetration. A series of simulation results were then used to produce semi-empirical correlations for the force required to detach a droplet from a hydrophobic fibrous surface in the in-plane and out-of-plane directions. At the end, a high-surface tension oil-based ferrofluids was used to partially cloak a nonmagnetic droplet (e.g., water) which resulted in a compound droplet to measure the nonmagnetic droplet adhesion on hydrophobic surfaces.

Chapter 8. References

1-B. Bhushan, M. Nosonovsky, The rose petal effect and the modes of superhydrophobicity, Philosophical Transaction of Royal Society A, 368 (2010), 4713–4728.

2-B.J. Carroll, The accurate measurement of contact angle, phase contact areas, drop volume, and Laplace excess pressure in drop-on-fiber systems, Journal of Colloid Interface Science, 57 (1976) 488–495.

3-B.J. Carroll, The equilibrium of liquid drops on smooth and rough circular cylinders, Journal of Colloid and Interface Science, 97 (1984) 195–200.

4-S. Rebouillat, B. Letellier, B. Steffenino, Wettability of single fibers – beyond the contact angle approach, International Journal of Adhesion and Adhesives, 19 (1999) 303.

5-G. McHale, M.I. Newton, Global geometry and the equilibrium shapes of liquid drops on fibers, Colloids and Surfaces A, 206 (2002) 79–86.

6-G. McHale, M.I. Newton, B.J. Carroll, The shape and stability of small liquid drops on fibers, Oil and Gas Science and Technology, 56 (2001) 47-54.

7- N.M. Farhan, H. Aziz, and H.V. Tafreshi, Simple Method To Measuring Intrinsic Contact Angle of a Fiber with Liquids, Experiments in Fluids60 (2019), 87.

8-C. Bauer, S. Dietrich, Shapes, contact angles, and line tensions of droplets on cylinders, Physical Review E, 62 (2000) 2428.

9-A. L. Dubov, A. Mourran, M. M¨oller, O. I. Vinogradova, Contact Angle Hysteresis on Superhydrophobic Stripes, The Journal of Chemical Physics 141 (2014), 074710.

10-M. Mei, J. Fan, D. Shou, The gravitational effect on the geometric profiles of droplets on horizontal fibers, Soft Matter, 9 (2013) 10324-10334.

11- H. Aziz, N. Farhan, and H.V. Tafreshi, Effects of fiber wettability and size on droplet detachment residue, Experiment in Fluids 59 (2018), 122.

12-D. Quéré, Wetting and roughness, Annual Review of Material Research, 38 (2008) 71-99.

13-P. Olin, S.B. Lindström, T. Pettersson, L. Wagberg, Water drop friction on superhydrophobic surfaces Langmuir, 29 (2013) 9079−9089.

14- H. Aziz, H.V. Tafreshi, Role of particles spatial distribution in drag reduction performance of superhydrophobic granular coatings, International Journal of Multiphase Flow, 98 (2018), 128.

15-D. Ebert, B. Bhushan, Wear-resistant rose petal-effect surfaces with superhydrophobicity and high droplet adhesion using hydrophobic and hydrophilic nanoparticles, Journal of Colloid and Interface Science 384 (2012) 182–188.

16-X. Dai, B.B. Stogin, S. Yang, T. Wong, Slippery wenzel state, ACSNano, 9 (2015) 9260–9267.

17-E. Bormashenko, Progress in understanding wetting transitions on rough surfaces, Advances in Colloid and Interface Science, 222 (2015) 92–103.

18-H. Aziz, M.M. Amrei, A. Dotivala, C. Tang, H.V.Tafreshi, Modeling Cassie droplets on superhydrophobic coatings with orthogonal fibrous structures, Colloids and Surfaces A 512 (2017) 61-70.

19-E. Bormashenko, O. Gendelman, G. Whyman, Superhydrophobicity of lotus leaves versus birds wings:different physical mechanisms leading to similar phenomena, Langmuir 28 (2012) 14992–14997.

20-T.M. Bucher, H.V. Tafreshi, Modeling air–water interface in disordered fibrous media with heterogeneous wettabilities, Colloids and Surfaces A: Physicochemical and Engineering Aspects, 461 (2014) 323–335.

21-S. S. Chhatre, W. Choi, A. Tuteja, K.C. Park, J. M. Mabry, G. H. McKinley, Robert E. Cohen, Scale dependence of omniphobic mesh surfaces, Langmuir 26 (2010) 4027–4035.

22-S. Michielsen, H. J. Lee, Design of a superhydrophobic surface using woven structures, Langmuir 23 (2007) 6004-6010.

23-J. Drelich, J. D. Miller, A. Kumar, G. M. Whitesides, Wetting characteristics of liquid drops at heterogeneous surfaces, Colloids and Surfaces A: Physicochemical and Engineering Aspects, 93 (1994) 1-13.

24-L. Gao, T. J. McCarthy, How Wenzel and Cassie were wrong, Langmuir, 23 (2007) 3762-3765.

25- A. R. Esmaeili, B .Sajadi, M. Akbarzadeh, (2020). Numerical simulation of ellipsoidal particles deposition in the human nasal cavity under cyclic inspiratory flow. Journal of the Brazilian Society of Mechanical Sciences and Engineering 42 (2020), 243.

26- G. McHale, S. Aqil, N. J. Shirtcliffe, M. I. Newton, H. Y. Erbil, Analysis of droplet evaporation on a superhydrophobic surface. Langmuir 21 (2005) 11053–11060.

27- T. H. Chou, S. J. Hong, Y. J. Sheng, H. K. Tsao, Drops Sitting on a Tilted Plate: Receding and Advancing Pinning. Langmuir 28 (2012) 5158−5166.

28- C.W. Extrand, A.N. Gent, Retention of Liquid Drops by Solid Surfaces, Journal of Colloid and Interface Science 138 (1990) 431-442.

29- D. Quere, M. J. Azzopardi, L. Delattre, Drops at Rest on a Tilted Plane, Langmuir 14 (1998) 2213–2216.

30- B. Krasovitski, A. Marmur, Drops down the hill: theoretical study of limiting contact angles and the hysteresis range on a tilted plate, Langmuir 21 (2005) 3881-3885.

31- E. Bormashenko, Y. Bormashenko, G. Whyman, R. Pogreb, A. Musin, R. Jager, Z. Barkay, Contact angle hysteresis on polymer substrates established with various experimental techniques, its interpretation, and quantitative characterization, Langmuir 24 (2008) 4020–4025.

32- E. Bormashenko, A. Musin, M. Zinigrad, Evaporation of droplets on strongly and weakly pinning surfaces and dynamics of the triple line, Colloids and Surfaces A 385 (2011) 235–240.

33- A.R. Esmaeili, N. Mir, R. Mohammadi, R. A facile, fast, and low-cost method for fabrication of micro/nano-textured superhydrophobic surfaces. Journal of Colloid and Interface Science 573 (2020) 317–327.

34- A. Marmur, The Lotus Effect: Superhydrophobicity and Metastability, Langmuir 20 (2004) 3517-3519.

35- A.I. ElSherbini, A.M. Jacobi, Retention forces and CAs for critical liquid drops on non-horizontal surfaces. Journal of Colloid and Interface Science 299 (2006) 841–849.

36- G. McHale, Cassie and Wenzel: Were they really so wrong?, Langmuir 23 (2007) 8200-8205.

37- P.S. Yadav, P. Bahadur, R. Tadmor, K. Chaurasia, A. Leh, Drop Retention Force as a Function of Drop Size, Langmuir 24 (2008) 3181-3184.

38- A. Marmur, E. Bittoun, When Wenzel and Cassie are right: Reconciling and global considerations. Langmuir 25 (2009) 1277-1281.

39- B. Balu, A. D. Berry, D. W. Hess, V. Breedveld, Patterning of superhydrophobic paper to control the mobility of micro-liter drops for two-dimensional lab-on-paper applications. Lab Chip 9 (2009) 3066–3075.

40- C. W. Extrand, S. Moon, Repellency of the Lotus Leaf: CAs, Drop Retention, and Sliding Angles. Langmuir 30 (2014) 8791−8797.

41- S. J. Hong, C. C. Chang, T. H. Chou, Y. J. Sheng, H. K. Tsao, A Drop Pinned by a Designed Patch on a Tilted Superhydrophobic Surface: Mimicking Desert Beetle, The Journal of Physical Chemistry C, 116 (2012) 26487−26495.

42- S. Bommer, H.Scholl, R. Seemann, K. Kanhaiya, V. Sheraton, N. Verma, Depinning of drops on inclined smooth and topographic surfaces: experimental and lattice boltzmann model study, Langmuir 37 (2014) 11086–11095.

43- G. Karapetsas, N. T. Chamakos, A. G. Papathanasiou, Efficient modelling of droplet dynamics on complex surfaces, Journal of Physics: Condensed Matter, 28 (2016) 085101.

44- J. Park, S. Kumar, Droplet Sliding on an Inclined Substrate with a Topographical Defect, Langmuir 33 (2017) 7352–7363.

45- M.M. Amrei, M. Davoudi, G.G. Chase, H.V. Tafreshi, Effects of Roughness on Droplet Apparent Contact Angles on a Fiber, Separation and Purification Technology 180 (2017) 107–113.

46- Ed. Bormashenko, Wetting of real surfaces, 2nd ed. De Gruyter, Berlin, (2018).

47- P.G. De Gennes, F. Brochard-Wyart, and D. Quéré, Capillarity and gravity, In: Capillarity and Wetting Phenomena, Springer, New York, NY, (2004).

48- S.H. Yousefi, D. G. Venkateshan, C. Tang, H.V. Tafreshi, B. Pourdeyhimi. Effects of electrospinning conditions on microstructural properties of polystyrene fibrous materials. Journal of Applied Physics, 124 (2018), 235307.

49- Y. Liao, R. Wang, A.G. Fane, Fabrication of bioinspired composite nanofiber membranes with robust superhydrophobicity for direct contact membrane distillation, Environmental Science & Technology 48 (2014), 6335.

50- F. Guo, A. Servi, A. Liu, K.K. Gleason, G.C. Rutledge, Desalination by membrane distillation using electrospun polyamide fiber membranes with surface fluorination by chemical vapor deposition, ACS Applied Materials & Interfaces 7 (2015), 8225.

51- A.T. Servi, J. Kharraz, D. Klee, K. Notarangelo, B. Eyob, E. Guillen-Burrieza, A. Liu, H.A. Arafat, K.K. Gleason, A systematic study of the impact of hydrophobicity on the wetting of MD membranes, Journal of Membrane Science 520 (2016), 850.

52- S. H. Yousefi, H.V. Tafreshi, H. V. (2020). Modeling electrospun fibrous structures with embedded spacer particles: Application to aerosol filtration. Separation and Purification Technology, 235 (2020) 116184.

53- D. Liang, Z. Lu, H. Yang, J. Gao, and R. Chen, Novel asymmetric wettable AgNPs/chitosan wound dressing: in vitro and in vivo evaluation, ACS Applied Materials & Interfaces 8 (2016), 3958.

54- M. Li, L. P. Zhang, Y. J. An, W. J. Ma, S. H. Fu, Relationship between silk fabric pretreatment, droplet spreading, and ink-jet printing accuracy of reactive dye inks, Journal of Applied Polymer Science135 (2018), 46703.

55- S. Zhang, J. Huang, Z. Chen, S. Yang, and Y. Lai, Liquid mobility on superwettable surfaces for applications in energy and the environment, Journal of Materials Chemistry A 7 (2019), 38.

56- S. H. Yousefi, C. Tang, H.V. Tafreshi, B. & Pourdeyhimi, B. Empirical model to simulate morphology of electrospun polycaprolactone mats. Journal of Applied Polymer Science, 136 (2019), 48242.

57- W. Li, and A. Amirfazli, Microtextured superhydrophobic surfaces: A thermodynamic analysis, Advances in Colloid and Interface Science, 132 (2007), 51.

58- S. Sinha-Ray, A.L. Yarin, Drop impact cooling enhancement on nano-textured surfaces. Part I: Theory and results of the ground (1 g) experiments, International Journal of Heat and Mass Transfer 70 (2014), 1095.

59-S. Litster, D. Sinton, N. Djilali, Ex situ visualization of liquid water transport in PEM fuel cell gas diffusion layers, Journal of Power Sources 154 (2006), 95.

60- D. Seo, J. Lee, C. Lee, Y. Nam, The effects of surface wettability on the fog and dew moisture harvesting performance on tubular surfaces, Scientific reports 6 (2016), 24276.

61- F. Weyer, A. Duchesne, N. Vandewalle, Switching behavior of droplets crossing nodes on a fiber network, Scientific Reports 7 (2017), 13309.

62- W. Shi, M.J. Anderson, J.B. Tulkoff, B.S. Kennedy, J.B. Boreyko, Fog harvesting with harps, ACS Applied Materials & Interfaces 10, 11979 (2018).

63- R. Mead-Hunter, A. J. C. King, B. J. Mullins, Aerosol-mist coalescing filters–a review, Separation and Purification Technology, 133, 484 (2014).

64- S.U. Patel, G.G. Chase, Separation of water droplets from water-in-diesel dispersion using superhydrophobic polypropylene fibrous membranes, Separation and Purification Technology 126, 62 (2014).

65- S. H. Yousefi, H.V. Tafreshi. Novel approach to model microstructure of dust-deposits comprised of polydisperse particles of arbitrary shapes. Separation and Purification Technology, (2020)116844.

66- S. Wurster, D. Kampa, J. Meyer, T. Muller, B.J. Mullins, G. Kasper, Measurement of oil entrainment rates and drop size spectra from coalescence filter media, Chemical Engineering Science (2015)132, 72.

67- X. Wei, H. Zhou, F. Chen, H. Wang, Z. Ji, and T. Lin, High-Efficiency Low-Resistance Oil-Mist Coalescence Filtration Using Fibrous Filters with Thickness-Direction Asymmetric Wettability, Advanced Functional Materials 29 (2019), 1806302.

68- A. N. Lembach, H. B. Tan, I. V. Roisman, T. G. Roisman, Y. Zhang, C. Tropea, A. L. Yarin, Drop impact, spreading, splashing, and penetration into electrospun nanofiber mats, Langmuir 26 (2010), 9516.

69- A. Moghadam, S.H. Yousefi, H. V. Tafreshi, and B. Pourdeyhimi, Characterizing Nonwoven Materials via Realistic Microstructural Modeling, Separation and Purification Technology, 211 (2019), 602.

70- R. P. Sahu, S. Sett, A. L. Yarin, B. Pourdeyhimi, Impact of aqueous suspension drops onto non-wettable porous membranes: hydrodynamic focusing and penetration of nanoparticles, Colloids and Surfaces A 467 (2015), 31.

71- A. Moghadam and H.V. Tafreshi, On Liquid Bridge Adhesion to Fibrous Surfaces under Normal and Shear Forces, Colloids and Surfaces A, 589 (2020), 124473.

72- R. Tadmor, P. Bahadur, A. Leh, H.E. Nguessan, R. Jaini, L. Dang, Measurement of Lateral Adhesion Forces at the Interface between a Liquid Drop and a Substrate. Phys. Rev. Lett. 103 (2009), 266101.

73- R. Tadmor, R. Das, S. Gulec, J. Liu, H.E. Nguessan, M. Shah, P.S. Wasnik, S.B. Yadav, S.B. Solid-liquid work of adhesion. Langmuir 33 (2017) 3594.

74- S. Gulec, S. Yadav, R. Das, R. Tadmor, Reply to Comment on “Solid–Liquid Work of Adhesion”, Langmuir 33 (2017) 13899-13901.

75- B.J. Mullins, A. Pfrang, R.D. Braddock, T. Schimmel, G. Kasper, Detachment of liquid droplets from fibres—experimental and theoretical evaluation of detachment force due to interfacial tension effects, Journal of Colloid and Interface Science 312 (2007) 333–340.

76- R. Mead-Hunter, B.J. Mullins, T. Becker, R.D. Braddock, Evaluation of the force required to move a coalesced liquid droplet along a fiber. Langmuir 27 (2011) 227 – 232.

77- C.J. Hotz, R. Mead-Hunter, T. Becker, A.J.C. King, S. Wurster, G. Kasper, B.J. Mullins, Detachment of droplets from cylinders in flow using an experimental analogue. J. Fluid Mech. 771 (2015), 327−340.

78- R.P. Sahu, S. Sinha-Ray, A.L. Yarin, B. Pourdeyhimi, Blowing drops off a filament, Soft Matter 9 (2013) 6053–6071.

79- F. Fang, M. Davoudi, G.G. Chase, Drop movement along a fiber axis due to pressure driven air flow in a thin slit. Sep. Purif. Technol. 140 (2015) 77−83.

80- M. Davoudi, J. Fang, G.G. Chase, Barrel shaped droplet movement at junctions of perpendicular fibers with different orientations to the air flow direction. Sep. Purif. Technol. 162 (2016), 1−5.

81- M.M. Amrei, D.G. Venkateshan, N. D'Souza, J. Atulasimha, H.V. Tafreshi, Novel approach to measuring the droplet detachment force from fibers, Langmuir 32 (2016) 13333.

82- J.V.I. Timonen, M. Latikka, O. Ikkala, R.H.A. Ras, Free-decay and resonant methods for investigating the fundamental limit of superhydrophobicity, Nature Communications 4 (2013) 2398.

83- N. Farhan, H. V. Tafreshi, Using Magnetic Field to Measure Detachment Force between a Nonmagnetic Droplet and Fibers, Langmuir 35 (2019) 8490–8499.

84- U. Banerjee, A.K. Sen, Shape evolution and splitting of ferrofluid droplets on a hydrophobic surface in the presence of a magnetic field, Soft Matter 14 (2018), 2915-2922.

85- H. Wu, R. Zhang, Y. Sun, D. Lin, Z. Sun, W. Pan, P. Downs, Biomimetic nanofiber patterns with controlled wettability, Soft Matter 4 (2008) 2429–2433.

86- E. Bormashenko, Y. Bormashenko, T. Stein, G. Whyman, E. Bormashenko, Why do pigeon feathers repel water? Hydrophobicity of pennae, Cassie-Baxter wetting hypothesis and Cassie-Wenzel capillarity-induced wetting transition, J. Colloid Interface Sci. 311 (2007) 212–216.

87- N. Ghochaghi, A. Taiwo, M. Winkel, B. Dodd, K. Mossi, G. Tepper, Electrospun Polystyrene coatings with tunable wettability, Journal of Applied Polymer Science132 (2015) 41592.

88- T. Ho, N. Ghochaghi, G. Tepper, Development of magnetic fabrics with tunable hydrophobicity, Journal of Applied Polymer Science 130 (2013) 2352–2358.

89- K.A. Brakke, The Surface Evolver, Exp. Math. 1 (1992) 141–165.

90- M Jamali, A Moghadam, HV Tafreshi, B Pourdeyhimi, Droplet adhesion to hydrophobic fibrous surfaces, Applied Surface Science 456 (2018), 626-636.

91- M Jamali, HV Tafreshi, B Pourdeyhimi, Droplet Mobility on Hydrophobic Fibrous Coatings Comprising Orthogonal Fibers, Langmuir 34 (2018), 12488-12499.

92- M Jamali, H Vahedi Tafreshi, B Pourdeyhimi, Penetration of liquid droplets into hydrophobic fibrous materials under enhanced gravity, Journal of Applied Physics 125 (2019), 145304.

93- S. Brandon,N. Haimovich, E. Yeger, A. Marmur, Partial wetting of chemically patterned surfaces: The effect of drop size, J. Colloid Interface Sci. 263 (2003) 237–243.

94-M. Jamali, H. V. Tafreshi, B. Pourdeyhimi, Easy-to-use correlations to estimate droplet mobility on hydrophobic fibrous coatings, colloids and Surfaces A: Physicochemical and Engineering Aspects 582, 123867 (2019).

95-R.E. Johnson, S.S. Sadhal, Fluid mechanics of compound multiphase drops and bubbles, Ann. Rev. Fluid Meeh. 17 (1985), 289-320.

96-S. Bansal, P. Sen, Axisymmetric and Nonaxisymmetric Oscillations of SessileCompound Droplets in an Open Digital Microfluidic Platform. Langmuir 33 (2017) 11047-11058.

97-L. Mahadevan, M. Adda-Bedia, Y. Pomeau, Four-phase merging in sessile compound drops, J. Fluid Mech. 451 (2002) 411-420.

98-O. M. Lavrenteva, L. Rosenfeld, A. Nir, Shape change, engulfment, and breakup of partially engulfed compound drops undergoing thermocapillary migration, Physical Review E 84 (2011) 056323.

99-A. Marmur, D. Valal, Correlating interfacial tensions with surface tensions: a Gibbsian approach. Langmuir 26 (2010) 5568−5575.

100-M. Ataei, H. Chen, T. Tang, A. Amirfazli, Stability of a liquid bridge between nonparallel hydrophilic surfaces, J. Colloid Interface Sci. 207 (2017), 492.

101-N. Farhan, H.V. Tafreshi, Universal expression for droplet–fiber detachment force, J. Appl. Phys. 24 (2018), 075301.

102- A. Moghadam, M. Jamali, D.G. Venkateshan, H.V. Tafreshi, B. Pourdeyhimi, A new approach to modeling liquid intrusion in hydrophobic fibrous membranes with heterogeneous wettabilities, Colloids Surf A 558 (2018) 154-163.

103- X. Wu, M. Yu, Z. Zhou, A. Bedarkar, Y. Zhao, Droplets engulfing on a filament, Appl. Surf. Sci. 294 (2014) 49– 57.

104- R. Iqbal, S. Dhiman, A.K. Sen, A. Q. Shen, Dynamics of a water droplet over a sessile oil droplet: compound droplets satisfying a Neumann condition, Langmuir 33 (2017), 5713-5723.

105- Y. Zhang, D. Chatain, S.L. Anna, S. Garoff, Stability of a compound sessile drop at the axisymmetric configuration, J. Colloid Interface Sci. 462 (2016), 88–99.

106- J. Guzowski, P.M. Korczyk, S. Jakielaa, P. Garstecki, The structure and stability of multiple micro-droplets, Soft Matter 8 (2012), 7269.

107- H. Aziz, H.V. Tafreshi, Competing forces on a liquid bridge between parallel and orthogonal dissimilar fibers, Soft Matter 15 (2019), 6967-6977

108- M.J. Neeson, R.F. Tabor, F. Grieser, R.R. Dagastine, D.Y.C. Chan, Compound sessile drops, Soft Matter 8 (2012), 11042.

109- C. Semprebon, G. McHale, H. Kusumaatmaja, Apparent contact angle and contact angle hysteresis on liquid infused surfaces, Soft Matter 13 (2017), 101-110.

110- F. Schellenberger, J. Xie, N. Encinas, A. Hardy, M. Klapper, P. Papadopoulos, H.J. Butt, D. Vollmer, Direct observation of drops on slippery lubricant-infused surfaces, Soft Matter 11 (2015), 7617-7626.

111- M. Jamali, H.V. Tafreshi, Measuring Force of Droplet Detachment from Hydrophobic Surfaces via Partial Cloaking with Ferrofluids, Langmuir 36 (2020) 6116–6125.

Appendix A: Vita

Mohammad Jamali

3010 Hanes ave, Richmond, Virginia 23222
Cell: (804)869-0402; Email: m.jamali2007@gmail.com

SUMMARY

- Demonstrated problem-solving ability in fluid and solid mechanics.
- Experienced in multi-phase flow and heat transfer modeling, and designing experimental setup.
- Proficient in Computational Fluid Dynamics (CFD) and computer programming.

PROFESSIONAL EXPERIENCE

Graduate Research and Teaching Assistant, *Virginia Commonwealth University* *May 2016-July 2020*

- Developed an analytical solution for droplet mobility and adhesion on superhydrophobic surfaces based on numerical and experimental studies.
- Produced a surface made of nonwoven fibers using electrospinning method for low droplet mobility.
- Developed predictive models and experimental approach for numerous fluid–surface interactions, e.g., droplet motion and penetration into fibrous surfaces.
- Experienced with Matlab and Surface Evolver.
- Authored/co-authored 8 journal articles.
- Teaching Assistant for Numerical Methods.
- Reviewer of Journal of Engineered Fibers and Fabrics.

Graduate Research and Teaching Assistant, *Iran University of Science and Technology* *Sep 2013-Sep 2015*

- Investigated water entry of spheres experimentally along with an analytical study.
- Proposed a new method for analyzing heat transfer and entropy generation of nanofluid flows.
- Conducted research for several course projects including CFD simulation of the lid-driven cavity problem with SIMPLE method by Fortran code, numerical simulation of flow over a flat plate, design of Francis Turbine 3D by Catia.
- Experienced with Fluent, Gambit, Fortran, Solid Works and Catia.
- Authored/co-authored 3 journal articles.
- Teaching Assistant for Fluid Mechanic.

Research Assistant, *Shiraz University* *Feb 2013-Sep 2013*

- Simulated ventilation of a subway environment using a developed code.
- Conducted research for HVAC system of Mofateh Dormitory by Carrier.
- Experienced with C++ and C.

TECHNICAL AND EXPERIMENTAL SKILLS

- **Experimental:** Electrospinning, Imaging (optical and SEM).
- **Engineering Packages:** Fluent, Matlab, Surface Evolver, Mathematica, Gambit, Solid Works and Catia.
- **Programming Languages:** C++, C, Fortran.

HONORS AND AWARDS

- Received *first-place poster award* at The American Filtration and Separations Society Filteration Conference *April 2019*

- Received *Special Achievement Award* from The Nonwoven Institute at NC state University *May 2018*
- Ranked 1st among Energy Conversion students at Iran University of Science and Technology. Received straight admission PhD offer in Energy Conversion at Iran University of Science and Technology (exemption from competitive PhD national exam). *May 2016*
- Top 0.5% of B.Sc. nationwide entrance exam of Iranian University with nearly 400000 participants *Sep 2009*

EDUCATION

- **PhD in Mechanical & Nuclear Engineering**
  Virginia Commonwealth University *May 2016–July 2020*
- **MS in Mechanical Engineering**
  Iran University of Science and Technology, Tehran, Iran *Sep 2013–Sep 2015*
- **BS in Mechanical Engineering**
  Shiraz University, Shiraz, Iran *Sep 2009–Aug 2013*

PEER-REVIEWED JOURNAL PUBLICATIONS

1. **M Jamali**, HV Tafreshi, Water droplet detachment from a hydrophobic bead using partial and full cloaking methods, **Langmuir**, in preparation (2020).

2. KS Mehta, **M Jamali,** H Holgewer, MM Amrei, HV Tafreshi, Measuring work of droplet adhesion via magnetic repulsion force, **Physical Review Letters**, in preparation (2020).

3. **M Jamali**, HV Tafreshi, Measuring force of droplet detachment from hydrophobic surfaces via partial cloaking with ferrofluids, **Langmuir** 36 (2020) 6116–6125.

4. **M Jamali**, HV Tafreshi, B Pourdeyhimi, Penetration of liquid droplets into hydrophobic fibrous materials under enhanced gravity, **Journal of Applied Physics** 125 (2019) 145304.

5. **M Jamali**, HV Tafreshi, B Pourdeyhimi, Easy-to-use correlations to estimate droplet mobility on hydrophobic fibrous coatings, **Colloids and Surfaces A** 582 (2019) 123867.

6. **M Jamali**, NM Nouri, M Navidbakhsh, An experimental study of the Worthington jet and cavity formation during the impact of a solid body on an oil film on water, under review, **Applied Ocean Research** (2020).

7. **M Jamali**, HV Tafreshi, B Pourdeyhimi, Droplet mobility on hydrophobic fibrous coatings comprising orthogonal fiber, **Langmuir** 34 (2018) 12488-12499.

8. **M Jamali**, A Moghadam, HV Tafreshi, B Pourdeyhimi, Droplet Adhesion to Hydrophobic Fibrous Surfaces, **Applied Surface Science** 456 (2018) 626–636.

9. A Moghadam, **M Jamali**, HV Tafreshi, B Pourdeyhimi, A new approach to obtaining capillary pressure–saturation relationships for porous media with heterogeneous wettabilities, **Colloids and Surfaces A** 558 (2018) 154–163.

10. M Siavashi, **M Jamali**, Optimal selection of annulus radius ratio to enhance heat transfer with minimum entropy generation in developing laminar forced convection of water-Al_2O_3 nanofluid flow, **Journal of Central South University** 24 (2017), 1850-1865.

11. M Siavashi, **M Jamali**, Heat transfer and entropy generation analysis of turbulent flow of TiO_2-water nanofluid inside annuli with different radius ratios using two-phase mixture model, **Applied Thermal Engineering** 100 (2016), 1149-1160.